Bifurcation Analysis of Quasi-Periodic Solutions Observed in Coupled Bistable Oscillators

明治大学大学院理工学研究科
2013年度
博士学位請求論文

Bifurcation Analysis of Quasi-Periodic Solutions Observed in Coupled Bistable Oscillators

明治大学大学院理工学研究科電気工学専攻

学位請求者　電気工学専攻
神山 恭平

Contents

1 General Introduction

Coupled oscillatory systems have many applications for the model of biological systems, information transmission lines, and so on. It has been analyzed in weakly nonlinear systems since many years ago. As a result, existence of some kind of periodic and quasi-periodic solutions is already found. A periodic solution is an oscillation composed of single frequency component like a sine wave. On the other hand, a quasi-periodic solution is an oscillation composed of multiple non-resonant frequency components. Two non-resonant frequencies mean that the frequency ratio is an irrational number. In general, number of frequency components of a quasi-periodic solution is larger than two. In this study, we analyze mainly simplest case where two frequency components form a quasi-periodic solution. Altogether, we aim to analyze asynchronous double-mode oscillation. In Poincaré section, a periodic solution becomes a one point, but, a quasi-periodic solution becomes infinite number of points distributed on one closed curve called Invariant Closed Curve (ICC).

In weakly nonlinear systems, one can observe only limited number of oscillation modes. In contrast, one can observe more oscillation modes in non-weak nonlinear systems. For example, one can observe a non-decaying propagating wave only in non-weak nonlinear system. This is an interesting oscillation mode similar to SOLITON, and attracts great attention in the field of physics and engineering. In general, some oscillation modes in weakly nonlinear system still remain even if nonlinearity becomes stronger. However, many of quasi-periodic oscillation modes do not remain and bifurcate to one synchronized frequency mode, because of effects of phase-locking. For this reason, in the analysis by averaged method limited to weak nonlinear systems, one cannot observe overall behavior of coupled oscillator systems. Therefore, analysis for non-weak nonlinear systems is desired.

We try to analyze bifurcation of quasi-periodic solutions not only by using averaged method but also by using direct method. By using Runge-Kutta method, one can directly obtain stable solutions. However, to perform bifurcation analysis, it is indispensable to obtain saddle unstable quasi-periodic solutions which cannot be obtained by direct Runge-Kutta method. Saddle unstable solution is such a solution that diverges to some directions (namely, unstable), and converges to other directions (namely, stable). Therefore, if a solution is unstable in the p-directions it is called an index p saddle solution. Saddle unstable solution is intractable, because, it is not obtained by time reversal simulation. Fortunately, if a saddle unstable solution is periodic, it becomes a saddle fixed point on Poincaré section which can be obtained by Newton's method. Up to now, various bifurcation sets are already obtained by using this method [1]. In contrast, for quasi-periodic solutions, there is no algorithm to calculate saddle quasi-periodic solutions, so far. Recently, we developed the algorithm based on bisection method to calculate a saddle unstable quasi-periodic solution. By using this algorithm, one can perform bifurcation analysis for quasi-periodic solutions.

The purpose of this study is to perform bifurcation analysis for solving various quasi-

periodic oscillation modes appeared in coupled oscillator systems regardless of strength of nonlinearity. Bifurcation analysis is a study that classifies qualitative changes of a solution when a parameter is changed across the bifurcation point. It is hardly done to quasi-periodic solutions, although already carried out in detail to periodic solutions. We develop the algorithm for obtaining bifurcation of quasi-periodic solutions. In this algorithm, most important part is the calculation of saddle unstable periodic solution. We overcome this difficulty via bisection method.

The composition of this paper is as follows.

Chapter 2; Before explaining the bifurcation of quasi-periodic solution in detail, we demonstrate the propagating pulse wave solution which is one of the quasi-periodic solutions appearing in coupled bistable oscillator systems. The propagating pulse wave has an interesting propagation phenomena such as chaotic propagation. The velocity and statistical characteristics of this solution is presented.

Chapter 3; The bifurcation analysis of quasi-periodic solutions, propagating pulse wave solution and switching solution, are shown in this chapter. The bifurcation mechanism of propagating pulse wave solution is the combination of heteroclinic and pitchfork bifurcations. We also prove switching solutions present pitchfork bifurcation of quasi-periodic solution.

Chapter 4; In this chapter, we demonstrate the algorithm for obtaining saddle quasi-periodic soution in between two different attractors in the mutually coupled bistable oscillator system. We clarify the saddle-node and pithcfork bicurcations of double-mode (quasi-periodic) oscillations.

Chapter 5; Comparison between the bifurcation mechanisms of propagating wave solutions in six-coupled and three-coupled bistable oscillator systems, is shown. The bifurcation mechanism of the ring of three-coupled oscillators is almost the same as that of six-coupled oscillators. This chapter suggests that the bifurcation mechanism of propagating wave solution does not depend on number of oscillators.

Chapter 6; In this chapter, we improve the algorithm in Ch. 4 for obtaining a saddle quasi-periodic solution sandwiched between two attractors. Two improved approaches are shown. The first one is “overall template method” which can be applied to any attractors. The second one is “partial template method” which is faster than the first method but applied only to some restricted cases.

2 Chaos of the Propagating Pulse Wave in a Ring of Six-Coupled Bistable Oscillators

In this chapter, some properties of the chaotic propagating pulse wave in a ring of six-coupled bistable oscillators are investigated. When coupling factor α becomes large beyond a certain critical value, the standing pulse wave converts to a propagating pulse wave. Further, as α is increased, the propagating pulse wave behaves chaotically. We find some interesting properties of the chaotic propagating pulse wave such as random change of propagating direction and stepwise change of pulse position with respect to time. In particular, we notice that the shape of probability density of one-direction propagation time and distance is similar to that of Logistic map.

2.1 Introduction

Pulse wave propagation phenomena in coupled oscillator systems are of considerable interest among nonlinear scientists [2], [3], [4]. We investigate various behavior of pulse wave occurring in a ring of coupled bistable oscillators [5], [6]. Namely, there is a standing pulse wave staying in one place for small coupling factor. When the coupling factor becomes large beyond a certain critical value, the standing pulse wave converts to the propagating pulse wave. Further, for larger coupling factor, the propagating pulse wave becomes chaotic in some cases. It changes its propagation direction in random manner. In this chapter, we investigate properties of the chaotic propagating pulse wave such as probability density of one-direction propagation time and distance in the ring of six-coupled bistable oscillators. As a result, we notice that the shape of the probability density is close to that of Logistic map.

2.2 Circuit model and Equation

Figure 2.1a is our circuit model where N oscillators are coupled by inductor L_0. Each oscillator in Fig. 2.1b presents two states; oscillation or no oscillation depending on the initial condition. This type of oscillator has the following fifth-power nonlinear conductance (NC) whose V-I characteristic is given by: $i_{NC} = g_1 v - g_3 v^3 + g_5 v^5$ for $g_1, g_3, g_5 > 0$. After normalizing circuit equation of Fig. 2.1a, the system equation can be written as shown in Eq. (2.1) where the state variable with even number is proportional to voltage of each oscillator and where that with odd number is proportional to its derivative. Namely, $x_{2i} \propto v_{i+1}$ and $x_{2i+1} \propto \dot{v}_{i+1}$

for $i = 0, 1, 2, 3, \cdots, N-1$. The parameter ϵ (> 0) shows the degree of nonlinearity. The parameter α ($0 \leq \alpha < 1$) is a coupling factor; namely $\alpha = 1$ means maximum coupling, and $\alpha = 0$ means no coupling. The parameter β controls amplitude of oscillation. In this chapter, we investigate the case of $N = 6$ with parameters $\beta = 3.18$ and $\epsilon = 0.36$.

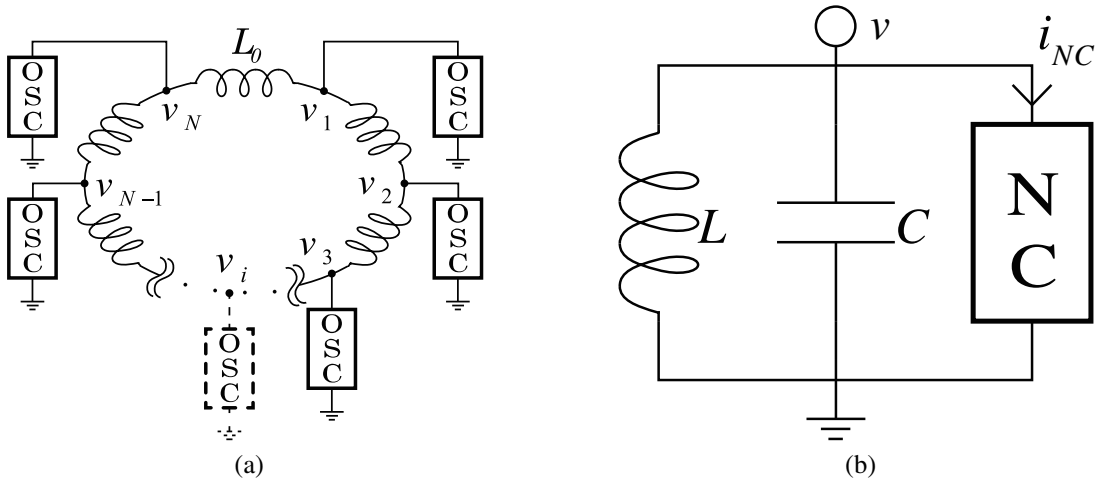

Figure 2.1: Circuit model. (a) A ring of N-coupled oscillators. (b) A model of bistable oscillator with hard type nonlinearity whoes V-I characteristic is given by $i_{NC} = g_1 v - g_3 v^3 + g_5 v^5$ for $g_1, g_3, g_5 > 0$.

$$\begin{aligned} \dot{x}_{2i} &= x_{2i+1} \\ \dot{x}_{2i+1} &= -\epsilon(1 - \beta x_{2i}^2 + x_{2i}^4)x_{2i+1} \\ &\quad - (1-\alpha)x_{2i} + \alpha(x_{2i-2} - 2x_{2i} + x_{2i+2}) \\ &\quad i = 0, 1, 2, 3, 4, \cdots, N-1 \pmod{2N} \end{aligned} \tag{2.1}$$

2.3 Chaotic propagating pulse wave in a ring of six-coupled bistable oscillators

We have already clarified that the transition from the standing pulse wave to the propagating pulse wave is a bifurcation from a periodic solution to a quasi-periodic solution, and that the bifurcation originates in a combination of pitchfork and heteroclinic bifurcations [6]. When coupling factor α is increased further, it is noted that propagation speed increases and beyond a certain critical value of α, the propagation wave becomes chaotic. The variation of Lyapunov exponents is presented in terms of α in Fig. 2.2. Namely, in region A($0.0800 \leq \alpha < 0.0905$), where the standing pulse wave exists, $LE1 = 0$ and $LE2 \cdots LE12 < 0$. Therefore, this is a periodic solution. In region B($0.0905 \leq \alpha < 0.1118$) where the non-chaotic propagating pulse wave exists, $LE1 = LE2 = 0$ and $LE3 \cdots LE12 < 0$. Therefore, this is a quasi-periodic solution. In region C($0.1118 \leq \alpha < 0.1162$) where the chaotically propagating pulse wave

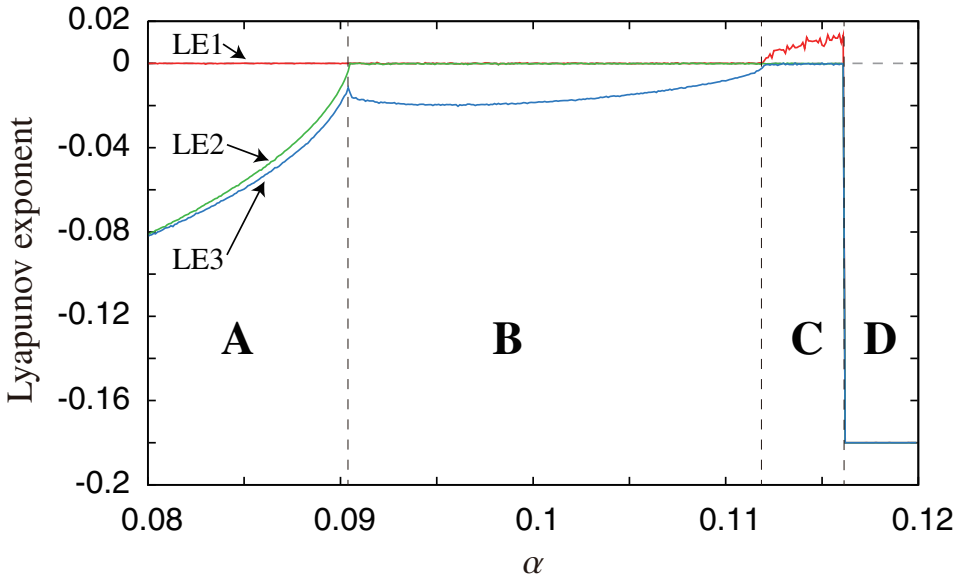

Figure 2.2: Transition of three dominant Lyapunov exponents $LE1 \geq LE2 \geq LE3$ in terms of α. Region A:Periodic; Region B:Quasi-periodic; Region C:Chaotic; Region D:no oscillation.

exists, $LE1 > 0$, $LE2 = 0$ and $LE3 \cdots LE12 < 0$. Therefore, this is a chaotic attractor. In region D($0.1162 \leq \alpha$) there is no oscillation.

Figure 2.3 demonstrates two-parameter bifurcation diagram in the α-β plane obtained by brute-force method where the symbol S denotes the standing pulse wave, PW1 denotes the non-chaotic propagating pulse wave of Type 1 [1], CPW1 denotes the chaotic propagating pulse wave of Type 1, and DEATH denotes the no oscillating solution. Extinction of PW1 or CPW1 to DEATH seems due to collision with a saddle object. The region of CPW1 is not large, but not too small. Figure 2.4 demonstrates 3D representation of typical (a) standing pulse wave, (b) non-chaotic propagating pulse wave, and (c) chaotic propagating pulse wave. Note that the standing pulse wave stays in one position, propagating pulse wave propagates in one direction; namely, propagating direction is unchanged once it is determined. In contrast, the chaotic propagating pulse wave changes its direction occasionally in random manner.

[1] The standing wave of Type 1 means the state in which one oscillator is alive and others are all death. It can bifurcate to the corresponding non-chaotic and chaotic propagating pulse wave [6].

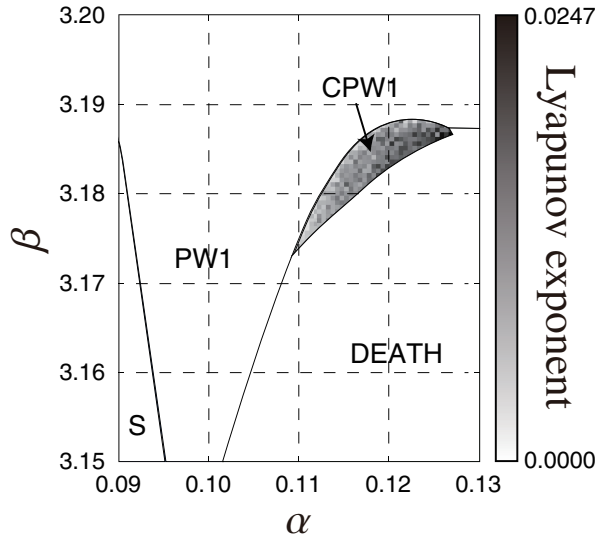

Figure 2.3: The region of positive Lyapunov exponent (black region) in two-parameter bifurcation diagram. The notations S,PW1,DEATH and CPW1 show the region of periodic oscillation, quasi-periodic oscillation, no oscillation and chaotic oscillation, respectively.

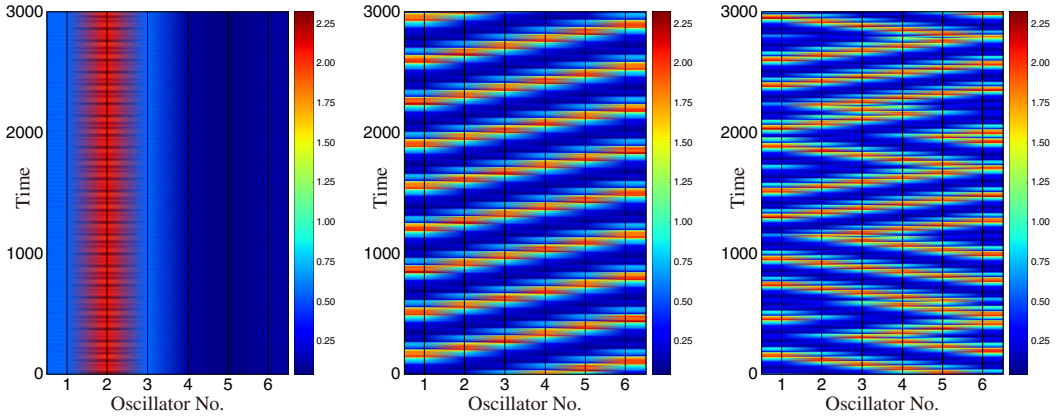

(a) (b) (c)

Figure 2.4: Three typical waves: (a) standing pulse wave for $\alpha = 0.08$, (b) non-chaotic propagating pulse wave for $\alpha = 0.10$ and (c) chaotic propagating pulse wave for $\alpha = 0.115$. The absolute magnitude $y_i = \sqrt{x_{2i}^2 + x_{2i+1}^2}, i = 0, 1, 2, 3, 4, 5$ ($i + 1$:number of oscillators) is shown in colors.

Figure 2.5 presents the propagating distance measured by oscillator number in terms of time for (a) α chosen in non-chaotic regime, and for (b) three values of α all chosen in chaotic regime (Appendix). We recognize that the propagating direction do not change in non-chaotic regime, but it suddenly changes in random manner in chaotic regime. It seems that the absolute value of propagating speed (= magnitude of the slope) in chaotic regime is constant for fixed values of α. Figure 2.6 shows absolute value of propagation speed in terms of α. We recognize that the propagation speed in chaotic regime is a smooth extension of the non-chaotic regime. That is, the (absolute value of) propagation speed increases with the increase of α.

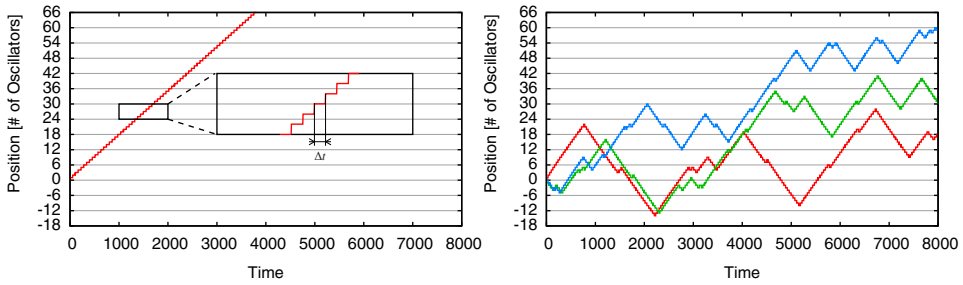

Figure 2.5: Propagating distance measured by oscillator number. (a) Non-chaotic propagating pulse wave for $\alpha = 0.100$. (b) Chaotic propagating pulse wave for $\alpha = 0.114$ (blue), 0.115 (red) and 0.116 (green). A pulse stays in one oscillator position for time Δt and suddenly moves to the next oscillator position, and vice versa. Small figure in (a) presents a magnified diagram. Same structure can be seen in (b).

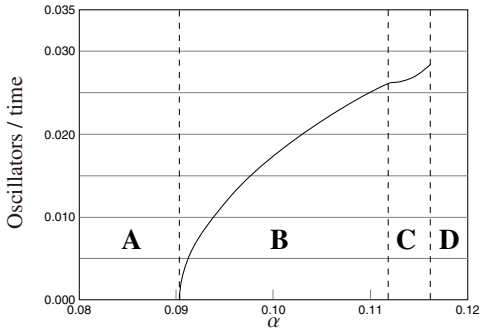

Figure 2.6: Propagating speed in terms of α. region A: standing pulse wave, region B: non-chaotic propagating pulse wave, region C: chaotic propagating pulse wave, region D: death.

We seek other cases in which chaos occurs for the ring of six-coupled bistable oscillators. In fact, there exists another standing wave such that two oscillators are alive and synchronized with reverse phase, and the rest one's are death (which is called Type 2). It can bifurcate to the

corresponding propagating pulse wave with the increase of α [7], but no chaos can be seen in this case, even if α is increased further. So far, we find no chaos other than that presented In this chapter.

2.4 Statistical characteristics of the chaotic propagating wave

Figure 2.7 (a), (b) and (c) demonstrates the probability density of one-direction propagation time (henceforth abbreviated as ODPT) for three values of α. Here, one-direction propagation time denotes the time length for which a chaotic pulse proceeds to one direction. The probability of occurrence of small ODPT and that of large ODPT are both large, while, that of medium ODPT is small. Moreover, maximum ODPT for small α is larger than that for large α. This means that the probability of propagating direction change is small for smaller values of α compared to larger values of α. One of the characteristic features of the probability density is its comb-like structure. This is because of the following reason. The time Δt in Fig. 2.5 denotes the time for a pulse to stay in one of the 6 oscillator position (locus of saddles and nodes), and the transition time from one position to next position is negligible compared to Δt. Thus ODPT can take only integral multiple of Δt.

Next, we will present the probability density of one-direction propagation distance (ODPD) in Fig. 2.8. The shape is almost similar to that of ODPT. However, no comb-like structure can be seen. This is because that ODPD is digitized to make histogram, therefore, all distance can be taken. After all, the shape of probability density of ODPT and ODPD is similar to that of Logistic map shown in Fig. 2.9. So far, we do not know the reason.

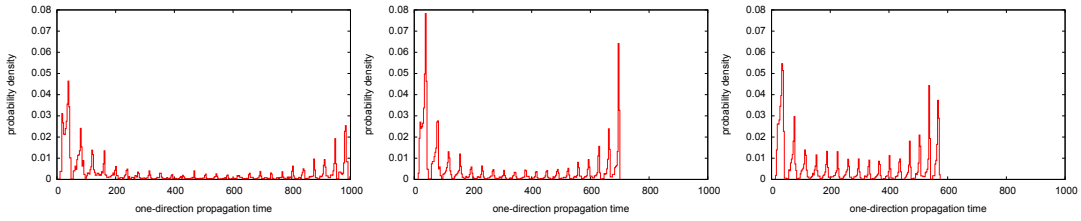

(a) (b) (c)

Figure 2.7: Probability density of one-direction propagation distance (ODPD) of a chaotic propagating pulse in the form of histogram in three different values of α: (a) $\alpha = 0.113$, (b) $\alpha = 0.114$, (c) $\alpha = 0.115$. The total time is 3,000,000 sec in Eq. (2.1).

2.5 Conclusion

We investigate properties of the chaotic propagating pulse wave in a ring of six-coupled oscillator system. Namely, we calculate propagating distance in term of time, propagating speed

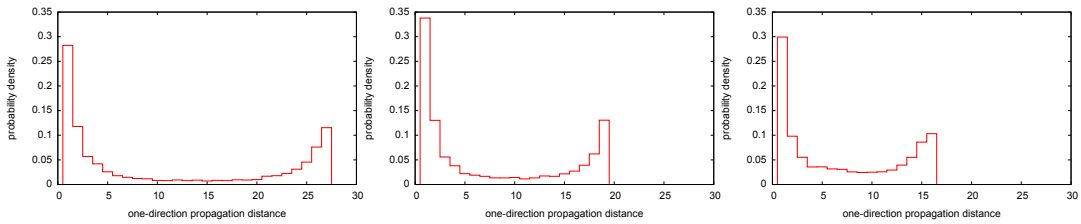

(a) (b) (c)

Figure 2.8: Probability density of one-direction propagation distance (ODPD) of a chaotic propagating pulse in the form of histogram in three different values of α: (a) $\alpha = 0.113$, (b) $\alpha = 0.114$, (c) $\alpha = 0.115$. The total time is 3,000,000 sec in Eq. (2.1).

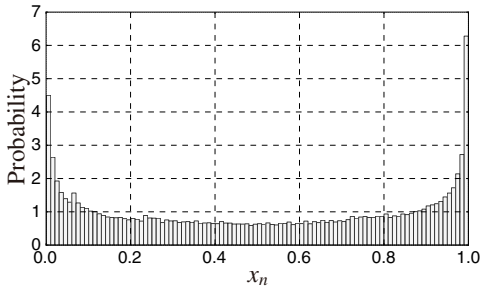

Figure 2.9: Probability density of Logistic map $x_{n+1} = 3.999x_n(1 - x_n)$ for $n = 0, 1, 2, \cdots, 100000$ for $x_0 = 0.123$.

in terms of coupling strength, and probability density of one-direction propagation time and distance. In the future, we investigate the generation mechanism of this chaos and find the reason why the shape of probability density of ODPT (ODPD) is similar to that of Logistic map. We perform rough computer simulation of Eq. (2.1) for other number of oscillators such as $N = 2, 3, 4, 5, 10, 100$ etc., but so far we find no chaos except this case. In the near future, we will try to find chaotic propagating wave solutions for other number of oscillators.

Appendix 2.A The method to obtain the time versus position diagram in Fig. 2.5

Figure 2.10(a) presents the time waveforms of six oscillators for one-direction propagation case. To obtain the diagram as shown in Fig. 2.5, we calculate the norm of $y_i = \sqrt{x_{2i}^2 + x_{2i+1}^2}, i = 0, 1, 2, 3, 4, 5$ in terms of time as in Fig. 2.10(b) and then sample y_i by every three second and pick up the oscillator number having largest y_i for $i = 0, 1, 2, 3, 4, 5$. Thus we can obtain the times series showing the oscillator number with largest norm at every sampling time.

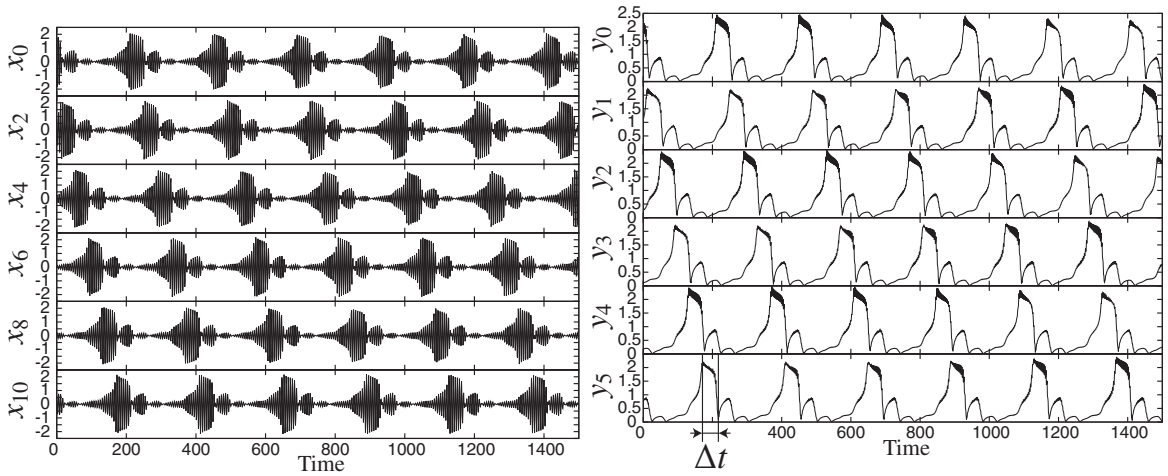

(a) (b)

Figure 2.10: Non-chaotic propagating pulse wave for $\alpha = 0.11$. (a) Time series of six oscillators x_0 to x_{10}. (b) Norm of y_0 to y_5. The time Δt denotes the one for a pulse to stay in one oscillator.

3 Bifurcation Analysis of the Propagating Wave and the Switching Solutions in a Ring of Six-Coupled Bistable Oscillators –Bifurcation Starting from Type 2 Solutions

In this chapter, we analyze the bifurcation of Type 2 periodic solution in a ring of six-coupled bistable oscillators. We show that pitchfork and heteroclinic bifurcations, which induce chaos, and cause a change from periodic (standing wave) solution to quasi-periodic (propagating wave) solution or the inverse when the coupling strength is varied. We also explain the existence of the switching solution, and presume that the birth and death of this switching solution are due to a pitchfork bifurcation of a quasi-periodic solution.

3.1 Introduction

Propagating wave phenomena in coupled oscillator systems have been reported [3, 5, 6, 8, 2]. Bifurcation mechanisms of the standing wave solution to the propagating wave solution in six-coupled bistable oscillators are described [6]. For a small coupling strength α, we obtain a periodic solution in which one "alive" oscillator is oscillating, and the other "dead" oscillators are not oscillating. These types of periodic solutions are referred to Type 1 solution. The Type 1 periodic solution loses its stability owing to pitchfork bifurcation and changes to the coexisting quasi-periodic (propagating wave) solution when α increases, as reported [6]. Further, as α decreases again, the quasi-periodic solution loses its stability to return to the periodic solution via a heteroclinic bifurcation.

In this chapter, we analyze the bifurcation of a Type 2 periodic solution in the same system, where two oscillators are alive (and inversely synchronized) and the other oscillators are dead. The results show that bifurcation between a Type 2 periodic solution and the corresponding quasi-periodic solution is due to pitchfork and heteroclinic bifurcations, similar to the case of Type 1 solution. The quasi-periodic solution, which is an invariant closed curve (ICC), becomes chaotic owing to the heteroclinic bifurcation. In addition, we find another quasi-periodic solution, which we call the "switching solution." This solution originates from

the periodic (standing wave) solution, and becomes an unstable quasi-periodic (switching) solution via pitchfork and saddle-node bifurcations. We show that this unstable quasi-periodic solution becomes stable when α reaches beyond some critical value by calculating the conditional Lyapunov exponent (LE). The death and birth of this quasi-periodic solution are possibly due to the subcritical pitchfork bifurcation [9].

3.2 Circuit and Equation

Fig. 3.1(a) depicts the circuit model where six oscillators are coupled by an inductance L_0. Each oscillator, called the hard-type oscillator, represents two states: oscillation or no oscillation depending on the initial condition [Fig. 3.1(b)]. This type of oscillator has the following fifth-power nonlinear conductance (NC) whose V-I characteristic is represented by $i_{NC} = g_1V - g_3V^3 + g_5V^5$ for $g_1, g_3, g_5 > 0$ [1]. After normalizing, the system equation for the circuit is shown in Fig. 3.1(a), the equation can be arranged as shown in Eq. (3.1).

$$\begin{cases} \dot{x}_i &= x_{i+1}, \\ \dot{x}_{i+1} &= -\epsilon(1 - \beta x_i^2 + x_i^4)x_{i+1} - (1-\alpha)x_i + \alpha(x_{i-2} - 2x_i + x_{i+2}), \end{cases} \quad (3.1)$$
$$i = 0, 2, 4, 6, 8, 10 \ \ (i : mod\ 12)$$

Here, the state variable denoted by an even number is proportional to the voltage of each oscillator and that denoted by an odd number is proportional to its derivative such that $x_{2i} \propto v_{i+1}$ and $x_{2i+1} \propto \dot{v}_{i+1}$ for $i = 0, 1, 2, 3, 4, 5$. Parameter α ($0 \leq \alpha \leq 1$) is the coupling factor between each oscillator, parameter β ($> 2\sqrt{2}$) determines the amplitude of oscillation, and parameter ϵ (> 0) represents the degree of nonlinearity. Throughout the paper, we will set $\beta = 3.20$ and $\epsilon = 0.36$.

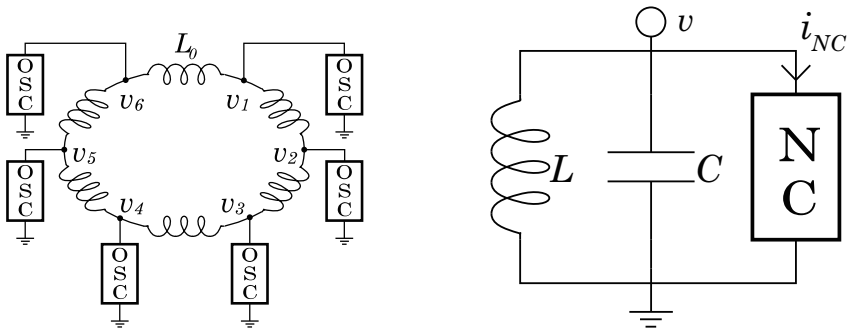

Figure 3.1: Circuit model. (a) A ring of six-coupled oscillators. (b) A model of bistable oscillator with hard-type nonlinearity whose V-I characteristic is given by $i_{NC} = g_1V - g_3V^3 + g_5V^5$ for $g_1, g_3, g_5 > 0$.

[1] The reason why we use the fifth-power NC is that oscillator can be bistable. In other words, the ordinary third-power NC can give only one oscillating state, hence monostable.

3.3 Bifurcation from Periodic to Quasi-Periodic Solution

We analyze a periodic solution for small α where two adjacent oscillators are oscillating and synchronized out-of phase, and the other oscillators are not oscillating [Fig. 3.2]. This type of solution is referred as Type 2 periodic solution that is different from the Type 1 periodic solution that was previously analyzed [6] [2].

Due to rotational symmetry of Eq. (3.1), there are co-existing six Type 2 periodic solutions, where oscillators (1,2), or (2,3), or (3,4), or (4,5), or (5,6), or (6,1) oscillate and others do not. This is clearly a standing wave solution. A Type 2 periodic solution becomes unstable when α becomes large. Then, the co-existing quasi-periodic solution that is a propagating wave solution appears as illustrated in Fig. 3.3.

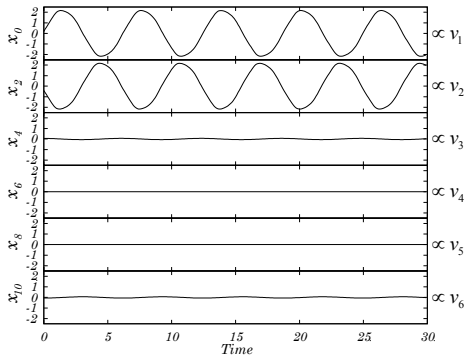

Figure 3.2: A Type 2 periodic solution for $\alpha = 0.01$ ($\beta = 3.2, \epsilon = 0.36$).

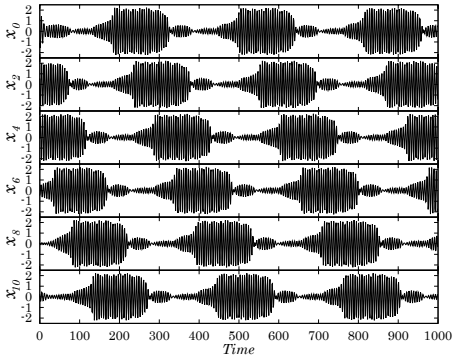

Figure 3.3: Quasi-periodic solution corresponding to Type 2 periodic solution for $\alpha = 0.12$ ($\beta = 3.2, \epsilon = 0.36$).

Fig. 3.4 is a one-parameter bifurcation plot of α versus x_0 [3]. The periodic solution corresponds to a stable node $D0$ and this node shows subcritical pitchfork bifurcation at $\alpha_{PF} = 0.0980$ to become an index 1 saddle $\tilde{D}1$. The index 1 saddle $\tilde{D}1$ and the corresponding index 2 saddle $D2$ meet together at $\alpha_{SN} = 0.0993$ and then disappear. On the other hand, there is a pair of index 1 saddle $D1$ emanating from α_{PF} in backward direction because α_{PF} is a subcritical pitchfork bifurcation point. The curve labeled as PW2 is a quasi-periodic solution presented as an average of L2 norm. The $\alpha_c = 0.0940$, i.e., the end point of PW2, is a heteroclinic bifurcation point that should be divided into two points α_{c1} and α_{c2} in finer scale. This will be discussed further in Section 4. For $\alpha > \alpha_{PF}$ the periodic (standing wave) solution becomes

[2] Type 1 periodic solution is a periodic solution in which only one oscillator oscillates and other oscillators do not oscillate.

[3] We consider Poincare section when x_1 goes across 0 from plus to minus. Hence this system becomes 11-dimensional phase space on the Poincare section. State variable x_0 is the first variable of the point $(x_0, x_2, x_3, ..., x_{11}) \in R^{11}$ on the Poincare section.

unstable and the co-existing quasi-periodic (propagating wave) solution appears. The quasi-periodic solution exists until α decreases and reaches α_c and the solution is then reduced to the periodic solution $D0$. We observe that there is hysteresis between $\alpha_c < \alpha < \alpha_{PF}$. Furthermore, we calculate the unstable manifold (UM) of $D1$, $\tilde{D}1$, and $D2$ saddles to clearly explain these bifurcations. Fig. 3.5 shows the connection of the UM for six typical values of α (point "a" to "f").

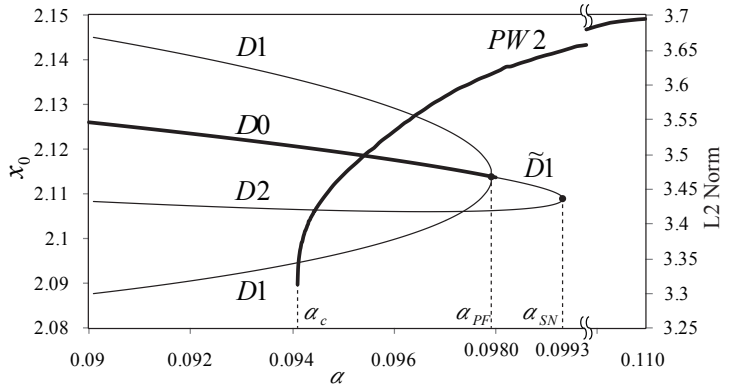

Figure 3.4: One-parameter bifurcation plot of α versus x_0 of the periodic solution of Type 2 ($\beta = 3.20$, $\epsilon = 0.36$). $D0$ denotes a stable node, $D1$ denotes an index 1 saddle, and $D2$ denotes an index 2 saddle. $PW2$ is a quasi-periodic solution presented as time average of L2 norm.

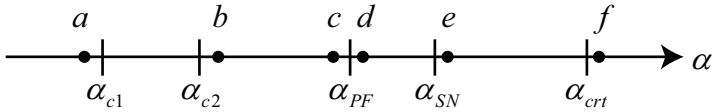

Figure 3.5: Location of parameter points "a" to "f" compared with bifurcation values on the α axis ($\beta = 3.2, \epsilon = 0.36$).

Fig. 3.6 shows a diagram for $\alpha = 0.0940 (< \alpha_{c1})$ (point "a"), where a pair of UM emanating from $D1$ (surrounding $D0$) goes to the present $D0$ and the next $D0$. Two pairs of UM emanating from $D2$ go to both the adjacent $D0$ and the present $D0$ [4]. Therefore, one of the six Type 2 periodic solutions [Fig. 3.2] can be determined for this coupling factor α.

Fig. 3.7 shows a schematic diagram for $\alpha = 0.0941$, which is greater than but close to α_{c2} (point "b"). Compared to Fig. 3.6, one of the UM of $D1$ goes to either a right rotating ICC (ICC_R) or a left rotating ICC (ICC_L), and others are almost the same as those in Fig. 3.6. In this case, six periodic solutions and ICC_R and ICC_L co-exist. Therefore, we show that the standing wave solution and the propagating wave solution coexist.

Fig. 3.8 represents a diagram for $\alpha = 0.0970 (\alpha_{c2} < \alpha < \alpha_{PF})$ (point "c"). The difference in point c compared to point b is that in the former, one of the UM of $D2$ goes to $D0$ located three

[4] The algorithm for drawing UM is reported in [10].

units ahead (or behind), to make a closed loop. Fig. 3.8(b) shows that there are three closed loops in total. Another difference is that the other pair of UM of $D2$ goes to ICC_R and ICC_L. This closed loop will become another quasi-periodic solution, which we call the "switching solution," for larger values of α. In this case, the attractors are six $D0$, ICC_R, and ICC_L.

Fig. 3.9 represents a diagram for $\alpha = 0.0980$, which is greater than but close to α_{PF} (point "d"). Compared to point c, the only change in point d is that although $D0$ is bifurcated to $\tilde{D}1$, there exists a closed loop connecting $\tilde{D}1$, $D2$, $\tilde{D}1$, and $D2$, which are located three units ahead. In this case, the attractors are only ICC_R and ICC_L. Compared to Fig. 3.8, two $D1$s and $D0$ merge together to become $\tilde{D}1$, whose UM goes to ICC_R and ICC_L. Therefore, the flow staying at $D0$ (periodic solution) before pitchfork bifurcation tends to flow to either ICC_R or ICC_L (quasi-periodic solution) along one of these UM after the bifurcation.

Fig. 3.10 represents a diagram for $\alpha = 0.0993$, which is greater than but close to α_{SN} (point "e") in which $\tilde{D}1$ and $D2$ coalesce to disappear. There is also a closed loop corresponding to unstable switching solution ICC (ICC_{SW}), which will be explained in Section 6. In this case, the attractors are only ICC_R and ICC_L.

Finally, Fig. 3.11 includes a diagram for $\alpha = 0.110 (> \alpha_{crt})$ (point "f") where the unstable ICC_{SW} in point e becomes stable ICC_{SW} (quasi-periodic switching solution). In this case, the attractors are ICC_R, ICC_L, and ICC_{SW}.

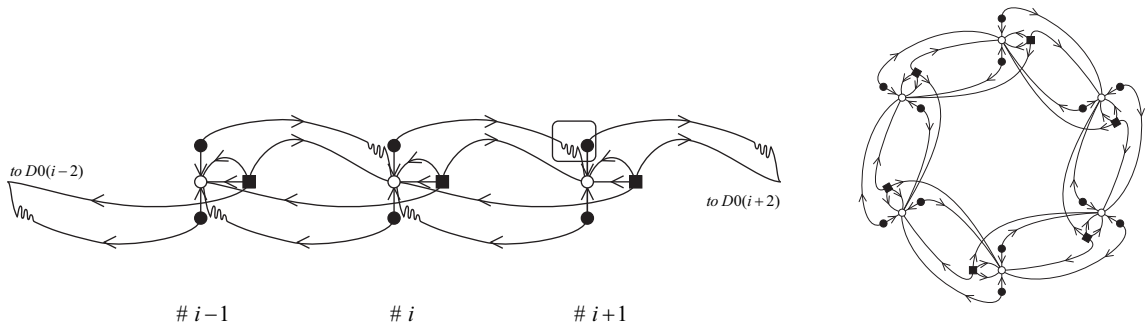

Figure 3.6: Connection of fixed points via UMs for point "a" of Fig. 3.5 ($\alpha = 0.0940, \beta = 3.20, \epsilon = 0.36$). Notation #$i$ denotes an ith Type 2 periodic solution. Notation $D0(i-2)$ denotes $D0$ for #$i-2$ and vice versa. White circle "$\circ$" denotes the stable node $D0$. Black circle "$\bullet$" denotes the saddle $D1$. Black square "$\blacksquare$" denotes the saddle $D2$. The square box denotes the region of heteroclinic tangle. (a) Magnified diagram. (b) Entire diagram.

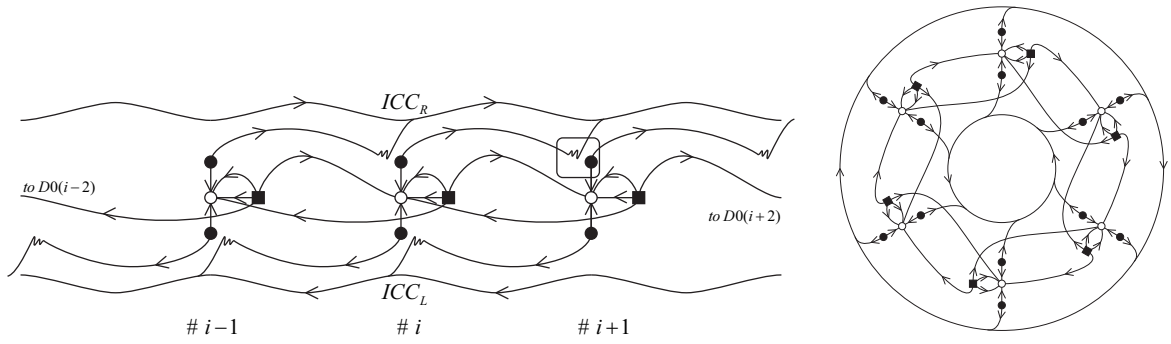

Figure 3.7: Connection of fixed points via UMs for point "b" of Fig. 3.5 ($\alpha = 0.0941, \beta = 3.20, \epsilon = 0.36$). Notations are very similar to those in Fig. 3.6. Notations ICC_R and ICC_L are used to describe the invariant closed curves (propagating wave solutions) rotating in right direction and left direction, respectively. The square box denotes the region of heteroclinic tangle. (a) Magnified diagram. (b) Entire diagram.

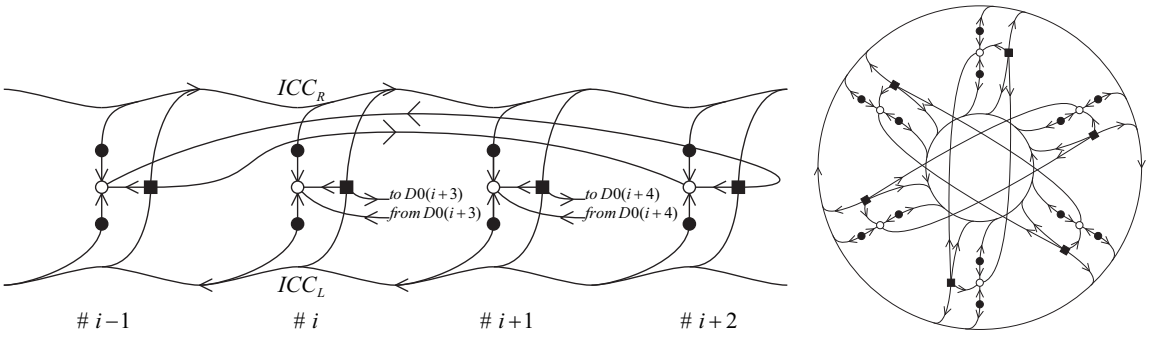

(a) (b)

Figure 3.8: Connection of fixed points via UMs for point "c" of Fig. 3.5 ($\alpha = 0.0970, \beta = 3.20, \epsilon = 0.36$). Notations are similar to those in Figs. 3.6 and 3.7. There is a closed loop connecting the fixed points which develops to the ICC associated with the switching solution ICC_{SW}. (a) Magnified diagram. (b) Entire diagram.

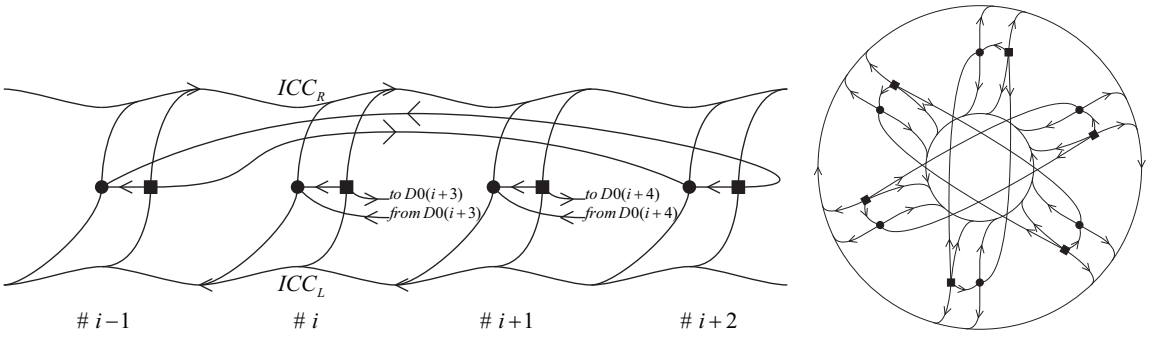

(a) (b)

Figure 3.9: Connection of fixed points via UMs for point "d" of Fig. 3.5 ($\alpha = 0.0980, \beta = 3.20, \epsilon = 0.36$). Notations are very similar to those in Figs. 3.6 and 3.7, except that "•" represents $\tilde{D}1$. There is a closed loop connecting the fixed points, which develops to ICC_{SW}. (a) Magnified diagram. (b) Entire diagram.

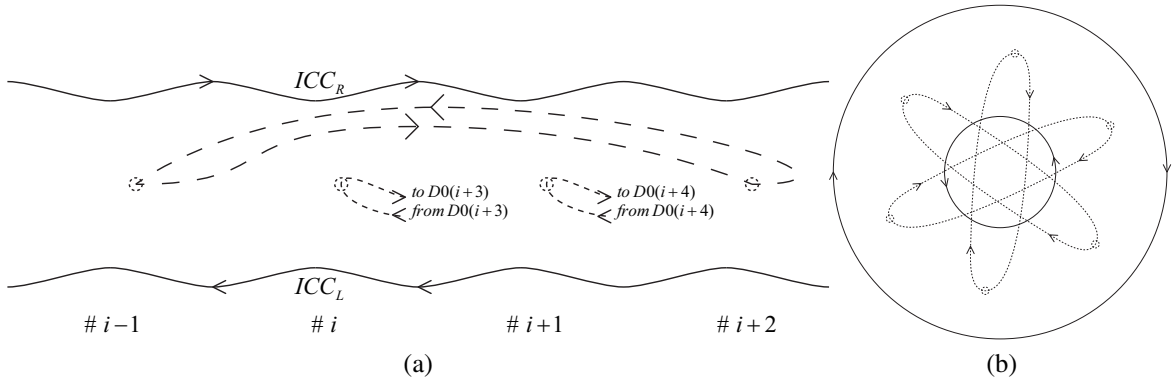

Figure 3.10: Connection of fixed points via UMs for point "e" of Fig. 3.5 ($\alpha = 0.0993, \beta = 3.20, \epsilon = 0.36$). Notations are similar to those in Figs. 3.6 and 3.7. There is an unstable ICC_{SW} that becomes stable for a larger α value. (a) Magnified diagram. (b) Entire diagram.

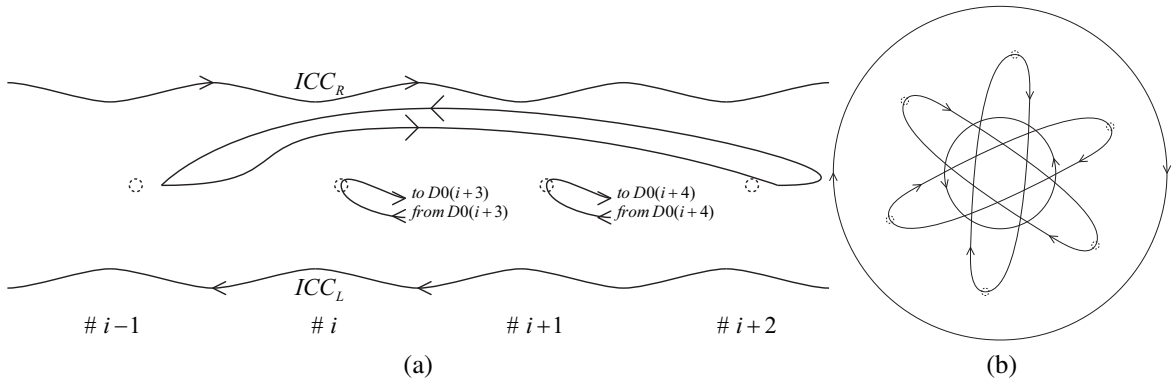

Figure 3.11: Connection of fixed points via UMs for point "f" of Fig. 3.5 ($\alpha = 0.1100, \beta = 3.20, \epsilon = 0.36$). There is an ICC_{SW} that associates with the switching solution. (a) Magnified diagram. (b) Entire diagram.

3.4 Heteroclinic Tangle Between Stable and Unstable Manifold for α_c

When α is decreased beyond $\alpha_c \simeq 0.094$, the quasi-periodic solutions ICC_R and ICC_L disappear at the same time, and the periodic solution $D0$ appears as shown in Figs. 3.6 and 3.7. In this section, we will investigate the reason for this disappearance of the quasi-periodic solution in view of the bifurcation theory. This bifurcation is called "Heteroclinic Bifurcation" which occurs around $\alpha_{c1} \simeq 0.094088$ and $\alpha_{c2} \simeq 0.094090$. At α_{c1} and α_{c2}, the stable manifold (SM) and the UM are tangent to each other, but their exact values are unknown. We focus on the upper $D1$ of $\#i + 1$, hereafter it is denoted as $D1(i + 1)$, and represented by a square box in Figs. 3.6 and 3.7. This is an index 1 saddle accompanied with subcritical pitchfork bifurcation. The saddle $D1$ has a one-dimensional UM and a ten-dimensional SM [5].

We will show the relationship between SM and UM of two successive $D1$'s around α_c. At α_{c1} and α_{c2}, the SM of $D1(i + 1)$ and UM of $D1(i)$ are tangent to each other. However, we do not know their exact values till date. We can draw UM in a three-dimensional phase space but not SM, because SM is ten dimensional. Thus, we consider a two-dimensional eigenspace corresponding to stable dominant eigenvalues, which are complex conjugate in this case, as an approximate representation of the SM [6].

Fig. 3.12 includes three schematic diagrams each showing the relationship between SM and UM for three cases. In Fig. 3.12(a), where $\alpha < \alpha_{c1}$, the UM of $D1(i)$ does not touch the SM of $D1(i + 1)$. In Fig. 3.12(b), where $\alpha_{c1} < \alpha < \alpha_{c2}$, UM and SM intersect transversally. In Fig. 3.12(c), where $\alpha_{c2} < \alpha$, UM goes to the other side of SM but does not intersect it.

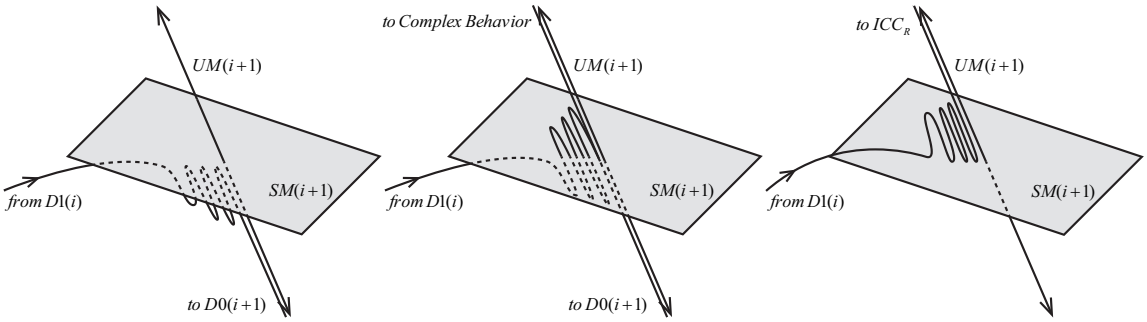

(a) $\alpha < \alpha_{c1}$ (b) $\alpha_{c1} < \alpha < \alpha_{c2}$ (c) $\alpha_{c2} < \alpha$

Figure 3.12: Schematic diagrams representing the relationship between SM($i + 1$) and UM(i).

The study continues with a numerical analysis. Fig. 3.13(a) represents the relationship between UM of $D1(i)$ and SM of $D1(i + 1)$ for $\alpha = 0.0940872$. We observe that the UM

[5] Since Eq. (3.1) is 12 dimensional, this system becomes 11 dimensional on the Poincare section.

[6] Dominant complex conjugate eigenvalues are those of which absolute value is smaller than and closest to unity. For example, they are $0.730856 \pm 0.064535i$ for $\alpha = 0.094089$. Compared to this case, in Type 1 case [6], the dominant eigenvalue is a real number, so the dominant stable eigenvector is one dimensional.

oscillates near the SM but does not intersect it, and that the UM tends to $D0(i+1)$ eventually. As a result, we observe that this value of α should be smaller than α_{c1}; Fig. 3.13(b) shows the relationship between the same UM and the same SM for $\alpha = 0.0940890$. We note that the UM is stretched in two directions, that is, depending on the initial condition, the mapped points can go to either direction. This is the evidence that UM and SM intersect transversally, and this is a heteroclinic tangle. Hence, the value of α should be between α_{c1} and α_{c2}. Fig. 3.13(c) shows what happens when $\alpha = 0.0940910$. The UM oscillates near SM asymptotically, and goes to ICC_R eventually (the direction opposite to that shown in Fig. 3.13(a)). As a result, the value of α should be greater than α_{c2}.

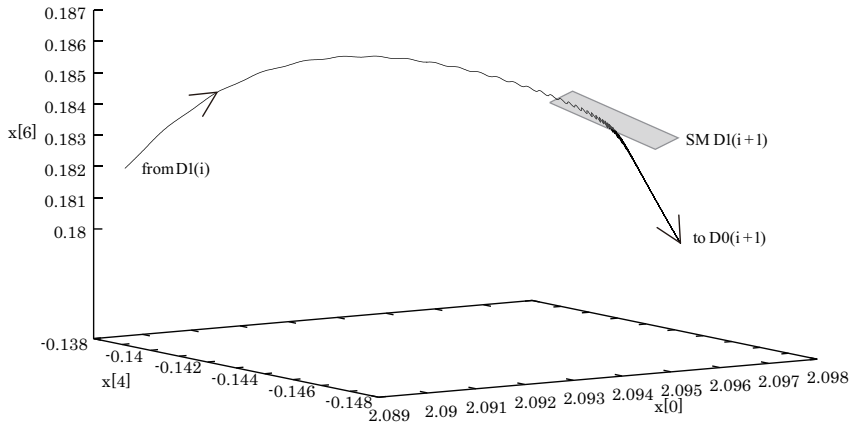

(a) $\alpha < \alpha_{c1}$

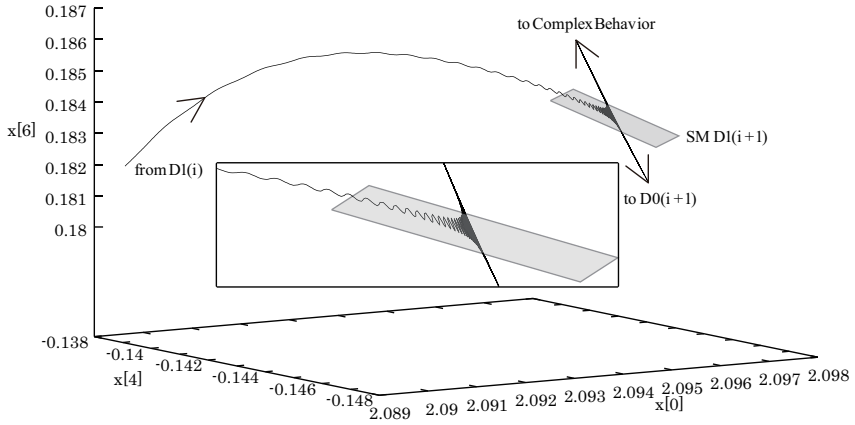

(b) $\alpha_{c1} < \alpha < \alpha_{c2}$

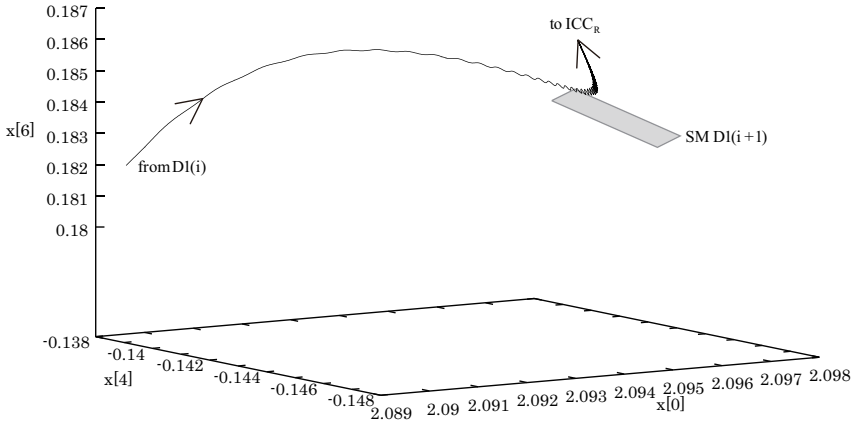

(c) $\alpha_{c2} < \alpha$

Figure 3.13: Computer simulation demonstration for three values of α: (a) $\alpha = 0.0940872$, (b) $\alpha = 0.0940890$, and (c) $\alpha = 0.0940910$. Each curve and plane denote UM and approximate SM respectively projected onto the (x_0, x_4, x_6)-direction.

3.5 Attractors Influenced by Heteroclinic Tangle

In this section, we discuss the effect of heteroclinic tangle on attractors. Fig. 3.14 illustrates the largest LE (excluding zero) in terms of α near α_{C1} and α_{C2} with respect to ICC_R [7]. The ICC_R is quasi-periodic for α much larger than α_{c2}, but it becomes chaotic as α approaches α_{c2}. In addition, there are many periodic windows as α moves close to α_{c2}, which are characterized by a negative LE. As α decreases further beyond α_{c2}, ICC_R survives and the largest LE grows larger until finally at $\alpha = \alpha_{c1}$, the chaotic ICC_R disappears and the co-existing stable node $D0$ appears [8]. Fig. 3.15 demonstrates ICC_R on the Poincare section for typical values of α. Fig. 3.15a presents a quasi-periodic attractor for a sufficiently large value of α, which is a smooth closed curve. Fig. 3.15b shows a (complex) periodic attractor at point "r" [Fig. 3.14], where the number of mapped points are finite. In Fig. 3.15c, we illustrate a quasi-periodic attractor close to chaos at point "q" [Fig. 3.14], where the mapped points appear similar to those for chaos in Fig. 3.15d, but the largest LE is almost zero. Fig. 3.15d represents a chaotic ICC_R at point "p" [Fig. 3.14], whose largest LE is positive. It follows that as α approaches the heteroclinic tangle interval, the attractor becomes non-smooth, which is an evidence of chaos. From the Smale-Birkhoff theorem [11, pp.106–111, pp.252–253], the existence of heteroclinic orbits (tangle) suggests that there is a horseshoe map, which implies that there is "transient chaos." In this case, it seems that there is a chaotic ICC_R attractor instead of transient chaos.

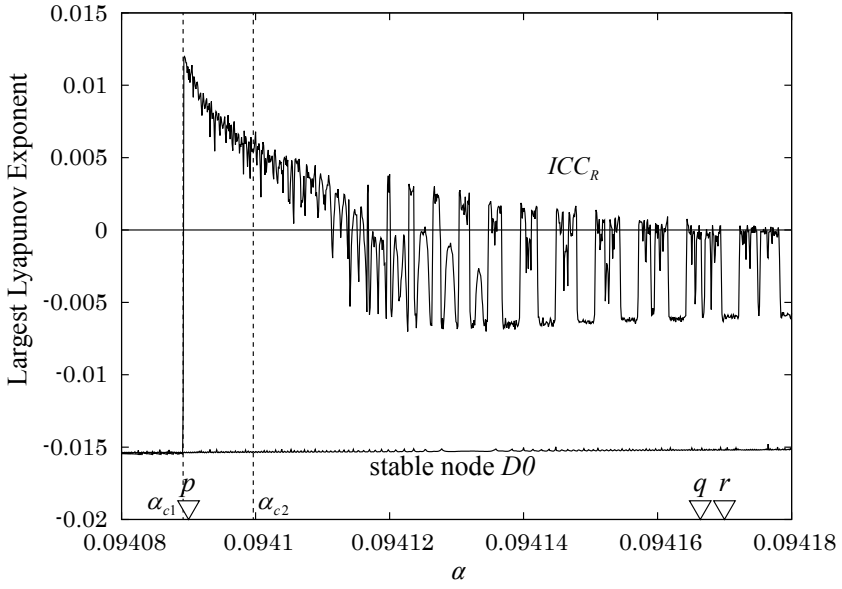

Figure 3.14: Variation of the largest LE in terms of α for a small interval including $\alpha_{c1} = 0.094088$ and $\alpha_{c2} = 0.094090$. Zero LE for autonomous system is excluded. Calculation time for each α is 50000 s, neglecting the first 3000 s for excluding the influence of transient.

[7] There exists ICC_L as well. Without confusion, we represent the attractors by ICC_R for simplicity.

[8] $D0$ cannot be influenced by heteroclinic tangle.

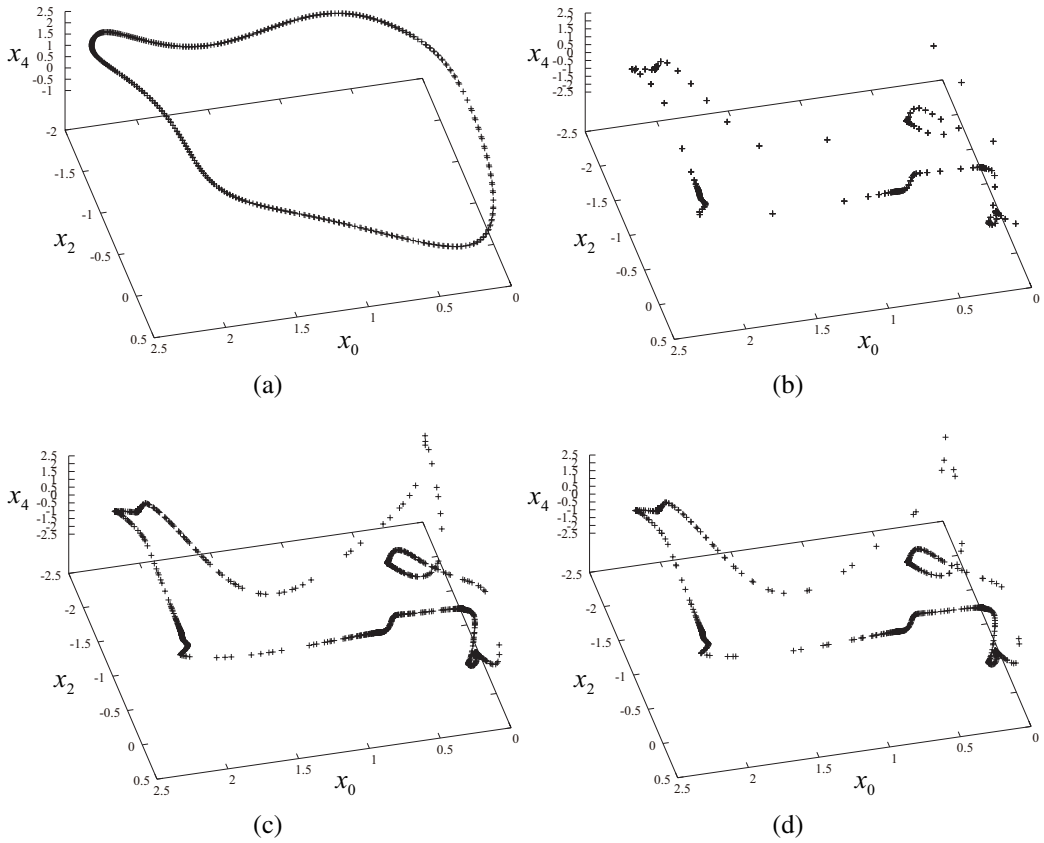

Figure 3.15: Poincare maps for ICC_R projected onto the (x_0, x_2, x_4)-subspace with typical values of α. (a) Quasi-periodic ICC_R for $\alpha = 0.6000000$. (b) Periodic ICC_R for $\alpha = 0.0941700$ (point "r" in Fig. 3.14). (c) Quasi-periodic ICC_R for $\alpha = 0.0941662$ close to chaos (point "q" in Fig. 3.14). (d) Chaotic ICC_R for $\alpha = 0.0940900$ (point "p" in Fig. 3.14).

3.6 Bifurcation of Quasi-Periodic Switching Solution

In this section, we will investigate another type of quasi-periodic solution. Fig. 3.16 depicts an example of this type of quasi-periodic oscillation, which we call the switching solution, because two pairs of oscillators (v_1, v_2) (x_0 and x_2) and (v_4, v_5) (x_6 and x_8) repeat a large amplitude oscillation and a small amplitude oscillation alternately. Here, oscillators 1 and 2 (also 4 and 5) are synchronized with reverse phase. Due to rotational symmetry, two pairs of oscillators (2,3) and (5,6) and those of (3,4) and (6,1) repeat the same behavior. We now investigate this type of quasi-periodic oscillation.

From our computer simulation results (for $\alpha = 0.12$), we notice that this quasi-periodic solution moves inside the six-dimensional linear subspace of 12-dimensional phase space in Eq. (3.1). The solution is constrained to the rest six-dimensional linear subspace. The constrained condition is as follows:

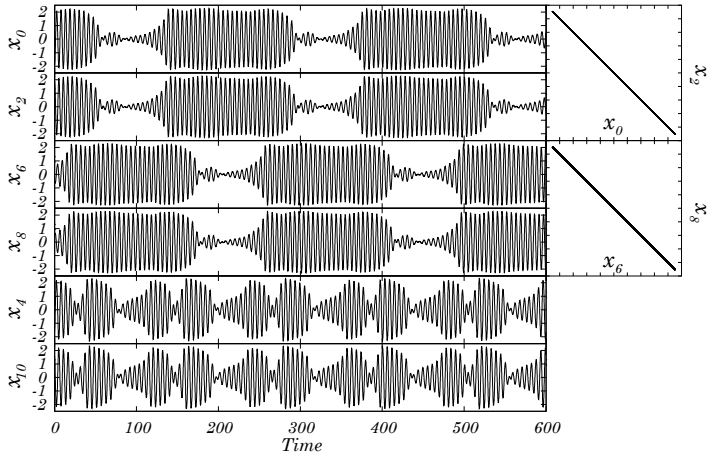

Figure 3.16: Demonstration of the switching solution ($\alpha = 0.12, \beta = 3.20, \epsilon = 0.36$). The initial condition is given by: $x_0(0) = 2.0, x_2(0) = -2.0$, and others are 0.0 with stepsize = 0.001 using the 4th-order RK algorithm.

$$\begin{cases} x_0 = -x_2, \\ x_1 = -x_3, \\ x_4 = -x_{10}, \\ x_5 = -x_{11}, \\ x_6 = -x_8, \\ x_7 = -x_9. \end{cases} \tag{3.2}$$

Since the quasi-periodic solution moves in the above constrained system, we perform the following transformation of variables so that the constrained point becomes zero.

$$\begin{cases} y_0 = x_0, \\ y_1 = x_1, \\ y_2 = x_4, \\ y_3 = x_5, \\ y_4 = x_6, \\ y_5 = x_7, \\ y_6 = x_0 + x_2, \\ y_7 = x_1 + x_3, \\ y_8 = x_4 + x_{10}, \\ y_9 = x_5 + x_{11}, \\ y_{10} = x_6 + x_8, \\ y_{11} = x_7 + x_9. \end{cases} \tag{3.3}$$

Through transformation of Eq. (3.3), Eq. (3.1) can be transformed into Eq. (3.4), where the linear subspace $H(\subset R^6)$ consists of y_0 to y_5:

$$H = \{(y_0, \cdots, y_{11}) \in R^{12} \mid y_6 = \cdots = y_{11} = 0\},$$

and the complementary subspace $H^{\perp}(\subset R^6)$ consists of y_6 to y_{11}:

$$H^{\perp} = \{(y_0, \cdots, y_{11}) \in R^{12} \mid y_0 = \cdots = y_5 = 0\}.$$

$$\left\{\begin{array}{ll}
\dot{y}_0 &= y_1,\\
\dot{y}_1 &= -\epsilon(1-\beta y_0^2+y_0^4)y_1-(1-\alpha)y_0+\alpha(-3y_0-y_2+y_6+y_8),\\
\dot{y}_2 &= y_3,\\
\dot{y}_3 &= -\epsilon(1-\beta y_2^2+y_2^4)y_3-(1-\alpha)y_2+\alpha(-y_0-y_2+y_4+y_6),\\
\dot{y}_4 &= y_5,\\
\dot{y}_5 &= -\epsilon(1-\beta y_4^2+y_4^4)y_5-(1-\alpha)y_4+\alpha(y_2-3y_4+y_{10}),\\
\dot{y}_6 &= y_7,\\
\dot{y}_7 &= -\epsilon(1-\beta y_0^2+y_0^4)y_1-\epsilon(1-\beta(y_6-y_0)^2+(y_6-y_0)^4)(y_7-y_1)-(1-\alpha)y_6+\alpha(y_8-y_6),\\
\dot{y}_8 &= y_9,\\
\dot{y}_9 &= -\epsilon(1-\beta y_2^2+y_2^4)y_3-\epsilon(1-\beta(y_8-y_2)^2+(y_8-y_2)^4)(y_9-y_3)-(1-\alpha)y_6+\alpha(-2y_8+y_{10}+y_6),\\
\dot{y}_{10} &= y_{11},\\
\dot{y}_{11} &= -\epsilon(1-\beta y_4^2+y_4^4)y_5-\epsilon(1-\beta(y_{10}-y_4)^2+(y_{10}-y_4)^4)(y_{11}-y_5)-(1-\alpha)y_{10}+\alpha(y_8-y_{10}).
\end{array}\right. \tag{3.4}$$

The quasi-periodic (switching) solution moves in the constrained linear subspace H with the complementary subspace $H^{\perp}$ components y_6 to $y_{11} = 0$. Next, we investigate the stability of the switching solution in the $H^{\perp}$ direction. If the solution is asymptotically stable in the $H^{\perp}$ direction, it is asymptotically stable in the total space. This is performed by investigating the stability of zero solution: $(y_6, y_7, y_8, y_9, y_{10}, y_{11}) = (0)$ in the following variational system with respect to y_6 to y_{11} where $(y_0, y_1, y_2, y_3, y_4, y_5)$ follows the switching solution.

$$\left\{\begin{array}{lll}
\dot{u}_0 &= & u_1,\\
\dot{u}_1 &= & (\epsilon(2\beta y_0-4y_0^3)y_1-1)u_0-\epsilon(1-\beta y_0^2+y_0^4)u_1+\alpha u_2,\\
\dot{u}_2 &= & u_3,\\
\dot{u}_3 &= & \alpha u_0+(\epsilon(2\beta y_2-4y_2^3)y_3-1-\alpha)u_2-\epsilon(1-\beta y_2^2+y_2^4)u_3+\alpha u_4,\\
\dot{u}_4 &= & u_5,\\
\dot{u}_5 &= & \alpha u_2+(\epsilon(2\beta y_4-4y_4^3)y_5-1)u_4-\epsilon(1-\beta y_4^2+y_4^4)u_5,
\end{array}\right. \tag{3.5}$$

where $y_{i+6} = u_i, \quad |u_i| \ll 1 \quad \text{for } i = 0, 1, 2, ..., 5.$

Solving the variational equation with respect to the switching solution, we can calculate the largest LE [9]. Fig. 3.17 shows the variation of this largest LE with respect to α associated to the bifurcation diagram of the periodic solution $D0$ of the H-constrained equation. As a result of Fig. 3.17, we make two observations.

1. The periodic solution $D0$ is stable for $\alpha < \alpha_{PF}$ and becomes unstable resulting in $\tilde{D}1$ at $\alpha = \alpha_{PF}$ via pitchfork bifurcation. The index 1 saddle $\tilde{D}1$ exists for $\alpha_{PF} < \alpha < \alpha_{SN}$.

[9] Making a simultaneous equation with the H-constrained Eqs. (3.4) and (3.5), the variational equation can be solved. The H-constrained equation of (3.4) is the system of first six equations in (3.4) with y_6 to $y_{11} = 0$.

2. The unstable quasi-periodic (switching) solution is born via saddle-node bifurcation of $\tilde{D}1$ and $D2$ at $\alpha = \alpha_{SN}$. The unstable switching solution exists for $\alpha_{SN} < \alpha < \alpha_{crt}$. At $\alpha = \alpha_{crt}$, where the largest LE changes its sign from plus to minus, it becomes stable.

It follows that although the switching solution exists for $\alpha_{SN} < \alpha < \alpha_{crt}$, it is not visible in the whole space, because it is unstable in the $H^{\perp}$-direction in this region. But, it becomes stable in the whole space beyond $\alpha > \alpha_{crt}$, because it is stable in the $H^{\perp}$-direction in this region. We infer that this is a subcritical pitchfork bifurcation of the quasi-periodic solution [9], although we cannot find two unstable quasi-periodic solutions surrounding a stable one till date.

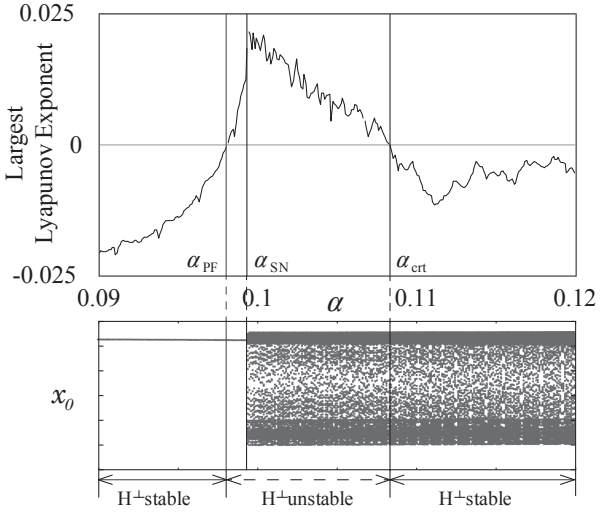

Figure 3.17: Largest LE (upper trace) and the associated one-parameter bifurcation diagram restricted to H (lower trace) in terms of α ($\beta = 3.20, \epsilon = 0.36$).

3.7 Supercritical Pitchfork Bifurcation of the Quasi-Periodic Switching Solution

In this section, we calculate unstable switching solution (SW-solution) by using our bisection algorithm (Chapter 6). We investigate the bifurcation of switching solution at the edge of stability and clarify that it is a supercritical pitchfork (PF) bifurcation [11].

Fig. 3.18 presents a series of Poincare maps of attractors of SW-solution projected onto the (x_4, x_{10}) plane with decrease of $\alpha(< \alpha_{crt})$. SW-solution is placed in H for $\alpha > \alpha_{crt}$, and α is gradually decreased across α_{crt} in Figs. 3.18(a), (b), and (c) by using the continuation method [10]. The -45 degree (blue) line presents unstable SW-solution (USW) in the linear subspace H. Fig. 3.18(a) presents two attractors for α a little smaller than α_{crt}. Red one presents one bifurcated SW-solution (SSW1) and green one presents the other bifurcated SW-solution (SSW2). These two bifurcated attractors are located in the proximity of H with

[10] In fact, we add small amount of noise in the process of continuation method.

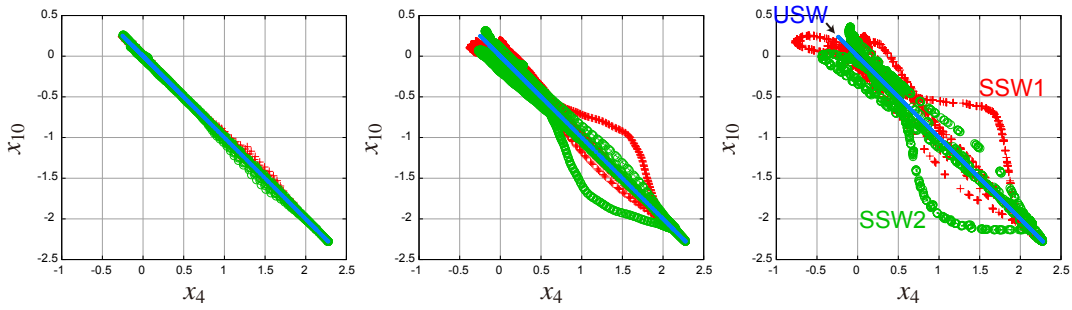

Figure 3.18: SSW1, SSW2 and USW on the Poincare section projected onto the (x_4, x_{10}) plane. The red plus marks denotes SSW1, the green circle marks denotes SSW2, and the -45 degree line (blue) denotes USW. (a) $\alpha = 0.10825(<, \simeq \alpha_{crt})$, (b) $\alpha = 0.10800(< \alpha_{crt})$, (c) $\alpha = 0.10700(\ll \alpha_{crt})$.

symmetrical position with respect to H. Fig. 3.18(b) presents SSW1 and SSW2 (red and green, respectively) for α apart from α_{crt} to some extent. The two bifurcated attractors are removed from the -45 degree line to some extent. Fig. 3.18(c) presents SSW1 and SSW2 for α departing from α_{crt} considerably. The two attractors are removed from the -45 degree line largely.

Fig. 3.19 demonstrates the stable and unstable quasi-periodic SW-solutions (SSW and USW, respectively) in H and two bifurcated SW-solutions: SSW1 and SSW2 out of H in the α versus D plane, which shows clearly that this is a supercritical PF bifurcation of SSW. We define the signed distance D of the quasi-periodic solution from H in Appendix A. The non-smooth parts of SSW1 and SSW2 appear due to frequency locking of the quasi-periodic solution.

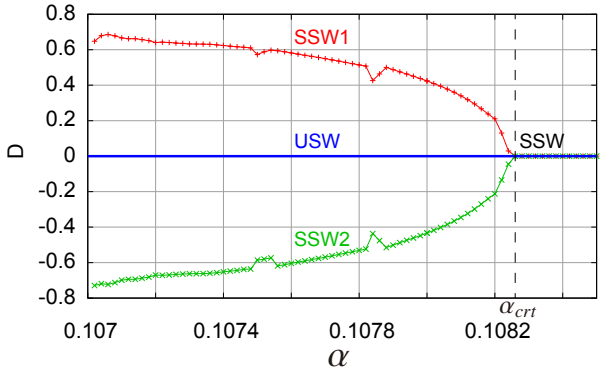

Figure 3.19: One-parameter-bifurcation diagram of SSW, SSW1, SSW2, and USW in terms of α showing supercritical PF bifurcation at α_{crt}. The vertical axis denotes the signed distance D from H.

Fig. 3.20 shows a schematic showing a series of bifurcations of periodic solutions and SW-solutions including chaotic solutions. Namely, for small $\alpha(< \alpha_{PF})$ there co-exist periodic solutions a and a' which correspond to the Type 2 periodic solution $D0$ explained before. The

periodic solution a (a') presents a subcritical PF bifurcation at $\alpha = \alpha_{PF}$ to become index 1 periodic solution $\tilde{D}1$ which is written as c (c'). The curves b1 and b2 (b1' and b2') are index 1 saddles appeared as a result of subcritical PF bifurcation. The d (d') presents index 2 saddle, and c and d (c' and d') merge together via SN bifurcation at $\alpha = \alpha_{SN}$. After SN bifurcation, two coexisting saddle pairs (c, d), and (c', d') disappear simultaneously, and USW appears. USW, SSW1, and SSW2 represent supercritical PF bifurcation at $\alpha = \alpha_{crt}$ to be SSW.

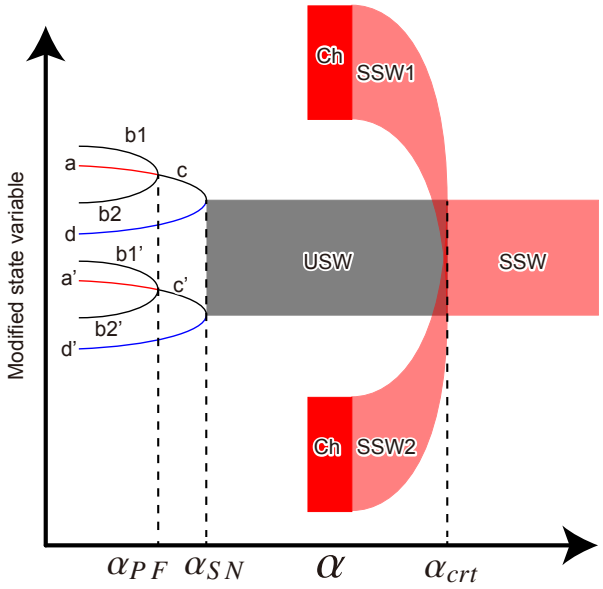

Figure 3.20: Schematic representing various bifurcations starting from Type 2 stable periodic solutions a and a' ($D0$). Curves b1 and b2 (b1' and b2') are index 1 saddles ($D1$) bifurcated from subcritical PF bifurcation. The curve c (c') is index 1-Type 2 periodic solution ($\tilde{D}1$). The curve d (d') is index 2 saddle ($D2$). USW and SSW denote unstable and stable SW-solutions. SSW1 (SSW2) denotes stable quasi-periodic solution bifurcated from supercritical PF bifurcation. Ch denotes chaos bifurcated from SSW1 (SSW2). See Fig. 3.4.

Fig. 3.21 presents a schematic showing qualitative changes of unstable manifolds (UMs) and invariant closed curves (ICCs) on Poincare section representing USW and SSW with the increase of α. (a) For $\alpha < (\simeq)\alpha_{PF}$, there coexist two stable nodes each of which presents a periodic solution such that only two oscillators oscillate and synchronized with reverse phase. (b) At $\alpha = \alpha_{PF}$, a subcritical PF bifurcation occurs and the stable nodes becomes unstable in the $H^{\perp}$ direction. The unstable nodes exist for $\alpha_{PF} < \alpha < \alpha_{SN}$. (c) At $\alpha = \alpha_{SN}$, SN bifurcation occurs and the periodic solutions (unstable nodes) become an unstable quasi-periodic solution in the $H^{\perp}$ complement direction. This is USW and it exists for $\alpha_{SN} < \alpha < \alpha_{crt}$. (d) For α smaller than but close to α_{crt}, there appear two stable SW-solutions: SSW1 and SSW2 around USW as a result of supercritical PF bifurcation at $\alpha = \alpha_{crt}$. (e) For $\alpha_{crt} < (\simeq)\alpha$, SSW1, SSW2, and USW are merged to become SSW as a result of supercritical PF bifurcation. Figs. 3.21 (a), (b), (c), and (e) correspond to one of three inner oval circles of Fig. 3.8(b), Fig. 3.9(b), Fig. 3.10(b) and Fig. 3.11(b), repectively.

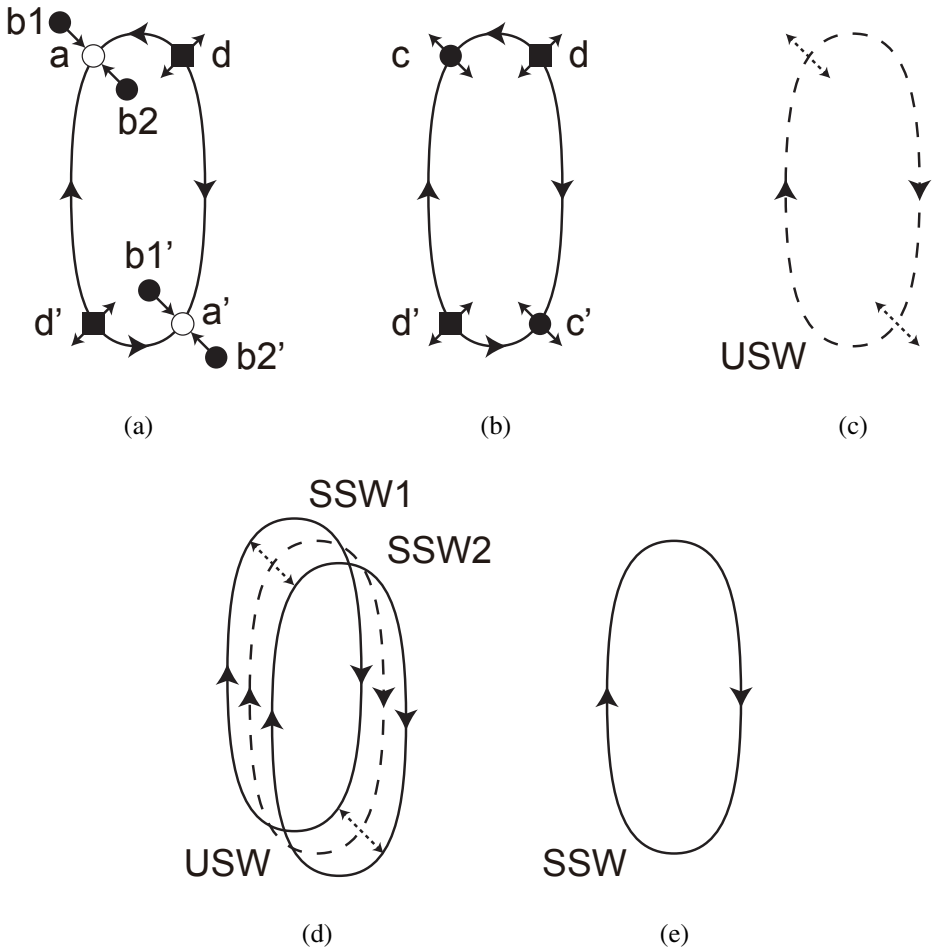

Figure 3.21: Schematic showing variation of connections of UMs in terms of α. (a) $\alpha < (\simeq)\alpha_{PF}$, (b) $\alpha_{PF} < \alpha < \alpha_{SN}$, (c) $\alpha_{SN} < \alpha < \alpha_{crt}$, (d) $\alpha < (\simeq)\alpha_{crt}$, (e) $\alpha_{crt} < \alpha$. Figures (a), (b), (c) and (e) correspond to one of three inner oval circles of Fig. 3.8(b), Fig. 3.9(b), Fig. 3.10(b) and Fig. 3.11(b), repectively.

3.8 Conclusion

We investigated periodic and quasi-periodic solutions originating in a Type 2 periodic solution in a ring of six-coupled hard-type oscillators. A Type 2 solution is a periodic solution in which two adjacent oscillators oscillate with a large amplitude and the other oscillators do not oscillate. We presented two types of quasi-periodic oscillations. The first type is a propagating wave solution and the second type is a switching solution. The bifurcation mechanism of appearance and disappearance of the propagating quasi-periodic solution is due to the heteroclinic bifurcation and that of the switching type quasi-periodic solution is due to the spercritical pitchfork bifurcation. The various bifurcations from Type 2 periodic solution to unstable and stable switching solutions is clarified by using the behavior of UMs of saddles and LEs. The progress compared to [9] is that PF bifurcation of (quasi-periodic) switching solution is calculated including USW, as an actual one-parameter-bifurcation diagram.

4 Bifurcation of Quasi-Periodic Solution in Mutually Coupled Bistable Oscillators: Demonstration of Unstable Quasi-Periodic Orbits

In this chapter, we obtain bifurcations of quasi-periodic orbits occuring in mutually coupled hard-type oscillators by using our recently developed computer algorithm to directly determine the unstable quasi-periodic orbits. So far, there is no computer algorithm to draw unstable invariant closed curves on a Poincaré map representing quasi-periodic orbits. Recently, we developed a new algorithm to draw unstable invariant closed curves by using the bisection method. The results of this new algorithm are compared with the previously obtained averaging method results. Several new results are found, which could not be clarified by the averaging method.

4.1 Introduction

Synchronized and asynchronized oscillations in mutually coupled oscillators have been investigated by many researchers for a long time [12, 13, 14]. In particular, it is well known that a quasi-periodic oscillation may occur in two mutually coupled identical hard-type oscillators. Perhaps, this fact was first clarified in [15], and more intensive analysis of the similar system was performed by using the averaging method [16, 17]. Specifically, when we draw the flow obtained from the averaging method in the phase plane, representing the amplitudes of two independent oscillation components in the horizontal and vertical directions as in Fig. 4.4, a quasi-periodic oscillation appears as a node or a saddle with non-zero horizontal and vertical axis components. In contrast, a periodic oscillation appears as a node or repeller on the horizontal or vertical axis. In conclusion, the averaging method yields one stable quasi-periodic oscillation (two-torus), which is called the "double mode oscillation," and three stable periodic oscillations, which correspond to "the same and the reverse phase synchronized oscillations" and "no oscillation." In addition, we find three saddles associated with unstable quasi-periodic oscillations and two repellers associated with unstable periodic oscillations.

In this example, we can investigate the bifurcation of quasi-periodic oscillations using the phase diagram obtained from the averaging method. In general, however, there is no method to investigate the bifurcation of quasi-periodic solutions except for particular cases [9], because

there is no algorithm to draw unstable invariant closed curves in the phase space. This situation is different from the periodic orbits in which unstable fixed points can be trapped by using the "fixed point algorithm," thereby identifying bifurcations of periodic orbits [1].

In this chapter, we draw a pair of stable and unstable invariant closed curves on the Poincaré map to confirm directly the saddle-node and pitchfork bifurcations of the quasi-periodic orbits by using our recently developed algorithm [18]. As a result, we have succeeded in verifying that saddle-node and pitchfork bifurcations are possible for quasi-periodic orbits. In addition, we found some discrepancies between the averaging method and the direct method results. That is, in the averaging method, the pitchfork bifurcation occurs for all values of $\alpha (0 \leq \alpha \leq 1$: coupling factor), but in the direct method, the saddle-node bifurcation occurs for almost all values of α, and the pitchfork bifurcation can only occur for special α values.

4.2 Model of mutually coupled oscillators and averaging method results [16]

Figure 4.1 presents two mutually coupled oscillators with hard-type nonlinearity. Each oscillator consists of a parallel connection of a simple LC and a nonlinear conductance (NC) whose I-V characteristic is represented by $i = g_1 v - g_3 v^3 + g_5 v^5$ for g_1, g_3 and $g_5 > 0$. An oscillator with this hard-type nonlinearity is bistable, i.e., both oscillation and no oscillation are possible. Here, two oscillators are coupled with two parallel inductors L_0s [1].

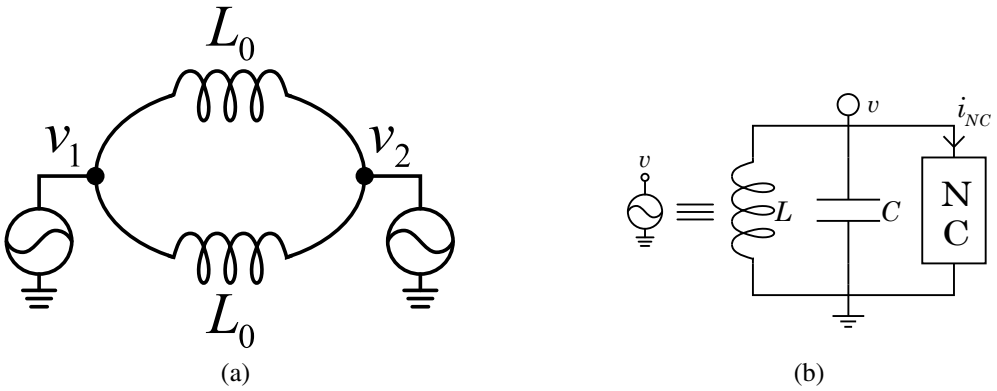

Figure 4.1: Mutually coupled identical oscillators. (a) Electrical circuit model of two-inductor coupled oscillators. (b) Configuration of hard-type oscillators.

After normalization ($x_1 \propto v_1, x_2 \propto v_2$), this system can be represented by the following

[1] In our previous model [16], two oscillators are coupled with one inductor L_0. The reason we adopt a two-inductor coupled model is that we aim to expand the model to a ring of more than three coupled oscillators. For that purpose, a two-inductor coupled model is more convenient than a one-inductor coupled model.

vector differential equation:

$$\begin{aligned} &\ddot{x} + Bx = -\epsilon\dot{x} + \tfrac{1}{3}\epsilon\beta\dot{x}_c - \tfrac{1}{5}\epsilon\dot{x}_f \\ &\text{where } x = [x_1, x_2]^T, x_c = [x_1^3, x_2^3]^T, x_f = [x_1^5, x_2^5]^T, \\ &\text{and where } B = \begin{bmatrix} 1+\alpha & -2\alpha \\ -2\alpha & 1+\alpha \end{bmatrix} \end{aligned} \tag{4.1}$$

In Eq. (4.1) $\epsilon > 0$ is a small number representing the degree of nonlinearity, α ($0 \le \alpha \le 1$) denotes a coupling factor, and β determines the oscillation magnitude [2]. In the averaging method we first assume a solution with $\epsilon = 0$. Choosing the appropriate linear transformation [16], leads to the following solution [3],

$$\begin{cases} x_1 = \sqrt{U_1/2}\sin(\sqrt{1-\alpha}\cdot t + \phi_1) + \sqrt{U_2/2}\sin(\sqrt{1+3\alpha}\cdot t + \phi_2), \\ x_2 = \sqrt{U_1/2}\sin(\sqrt{1-\alpha}\cdot t + \phi_1) - \sqrt{U_2/2}\sin(\sqrt{1+3\alpha}\cdot t + \phi_2). \end{cases} \tag{4.2}$$

When $\epsilon \neq 0$ but close to 0, we can apply the averaging method to Eq. (4.1) and the dynamics of $U_1 \ge 0$ and $U_2 \ge 0$ satisfy the following averaged equation [4], if we assume that the ratio of the two mode frequencies $\sqrt{1-\alpha}/\sqrt{1+3\alpha}$ is incommensurate [5].

$$\begin{cases} \dot{U}_1 = -\epsilon U_1(1 - \frac{1}{3}\beta U_1 - \frac{1}{4}\beta U_2 + \frac{1}{32}U_1^2 + \frac{3}{32}U_2^2 + \frac{3}{16}U_1U_2), \\ \dot{U}_2 = -\epsilon U_2(1 - \frac{1}{3}\beta U_2 - \frac{1}{4}\beta U_1 + \frac{1}{32}U_2^2 + \frac{3}{32}U_1^2 + \frac{3}{16}U_2U_1). \end{cases} \tag{4.3}$$

The steady state of the oscillations can be determined by the equilibrium points of the averaged equation. The stable equilibrium points are as follows, where "zz" denotes no oscillating attractor, "ss" the same-phase periodic attractor, "s-s" the reverse-phase periodic attractor, and "SICC" the two-torus quasi-periodic attractor:

(1) zz (stable region: all $\beta > 0$) : $(0, 0)$ node

(2) ss (stable region: $\beta > 2\sqrt{2}$) : $(2\beta + 2\sqrt{\beta^2 - 8}, 0)$ node

(3) s-s (stable region: $\beta > 2\sqrt{2}$): $(0, 2\beta + 2\sqrt{\beta^2 - 8})$ node

(4) SICC (stable region: $4\sqrt{5}/3 < \beta < 4$) : $((3\beta + \sqrt{9\beta^2 - 80})/5, (3\beta + \sqrt{9\beta^2 - 80})/5)$ node

The unstable equilibrium points are as follows, where "uu" and "u-u" denote the same-phase periodic repeller, and the reverse-phase periodic repeller, respectively. The "UICC1"–"UICC" are the two-torus quasi-periodic saddles.

(5) uu (unstable region:$\beta > 2\sqrt{2}$): $(2\beta - 2\sqrt{\beta^2 - 8}, 0)$ node (repeller)

[2] To start up an uncoupled hard-type oscillator, β should be: $\beta \ge 2\sqrt{2}$.

[3] Phases ϕ_1 and ϕ_2 are arbitrary constants in this case.

[4] The averaged equation can be obtained from Eq. (10) [16] with $N = 2$ and $\alpha_G = 0$.

[5] The frequency ratio, which should be avoided is determined from the nature of NC, and can be relaxed substantially in practice. At a minimum, we should avoid small integer ratios such as 1/2, 1/3 and 1/5, etc.

(6) u-u (unstable region:$\beta > 2\sqrt{2}$): $(0, 2\beta - 2\sqrt{\beta^2 - 8})$ node (repeller)

(7) UICC1 (unstable region:$0 < \beta < 4$): $(\beta + \sqrt{16 - \beta^2}, \beta - \sqrt{16 - \beta^2})$ saddle

(8) UICC2 (unstable region:$0 < \beta < 4$): $(\beta - \sqrt{16 - \beta^2}, \beta + \sqrt{16 - \beta^2})$ saddle

(9) UICC3 (unstable region: $\beta > 4\sqrt{5}/3$): $((3\beta - \sqrt{9\beta^2 - 80})/5, (3\beta - \sqrt{9\beta^2 - 80})/5)$ saddle

(10) UICC (unstable region: $\beta > 4$): $((3\beta + \sqrt{9\beta^2 - 80})/5, (3\beta + \sqrt{9\beta^2 - 80})/5)$ saddle

Figures 4.2–Fig. 4.5 present flows in the phase plane (U_1, U_2) calculated from the averaged equation Eq. (4.3) for typical values of β. Figure 4.2 shows flows for $\beta = 2.75$ where all flows converge to "zz." A similar phase diagram can be obtained for $0 < \beta < 2\sqrt{2} \simeq 2.828$. Figure 4.3 shows stable and unstable manifolds of saddles for $\beta = 2.96$ where two saddles, the "UICC1" and the "UICC2" and one node "zz" exist. The stable manifold of the "UICC1" and the "UICC2" separates the region of attraction of the "ss," the "zz," and the "s-s." A similar phase diagram can be obtained for $2\sqrt{2} \simeq 2.828 < \beta < 4\sqrt{5}/3 \simeq 2.980$. Figure 4.4 shows stable and unstable manifolds of saddles for $\beta = 3.5$ where three saddles, the "UICC1," the "UICC2," and the "UICC3," and four nodes, the "zz," the "ss," the "s-s," and the "SICC" exist. The stable manifold of each saddle separates the region of attraction of the "ss," the "s-s," the "SICC," and the "zz." A similar phase diagram can be obtained for $4\sqrt{5}/3 \simeq 2.980 < \beta < 4$. Figure 4.5 represents stable and unstable manifolds of saddles for $\beta = 4.1$ where two saddles, the "UICC," the "UICC3," and three nodes, the "ss," the "s-s," and the "zz" exist. The stable manifold of each saddle separates the region of attraction of the "ss," the "s-s," and the "zz." A similar phase diagram can be obtained for $\beta > 4$. The above results can be explained via

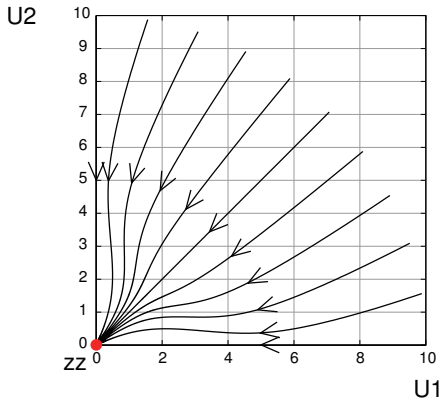

Figure 4.2: Phase plane diagram obtained from the averaged equation (4.3) for $\beta = 2.75$.

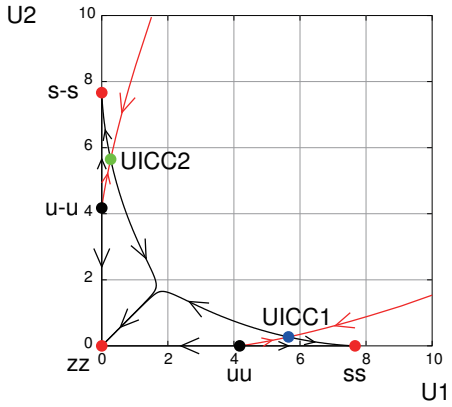

Figure 4.3: Phase plane diagram obtained from the averaged equation (4.3) for $\beta = 2.96$.

bifurcation theory. That is, at $\beta = 4$ the "SICC," the "UICC1" and the "UICC2" coalesce into the "UICC" as shown in Fig. 4.6. This is clearly a subcritical pitchfork bifurcation. Further, at $\beta = 4\sqrt{5}/3 \simeq 2.980$, the "SICC" and the "UICC3" coalesce and disappear as in Fig. 4.7. This is a saddle-node bifurcation.

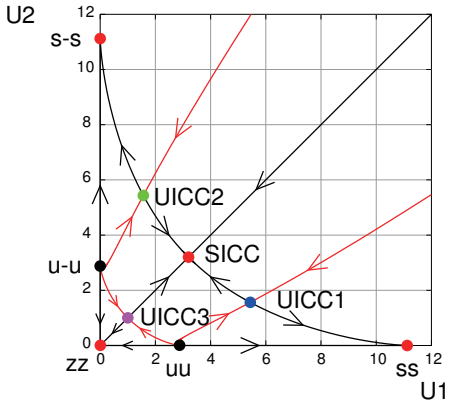

Figure 4.4: Phase plane diagram obtained from the averaged equation (4.3) for $\beta = 3.50$.

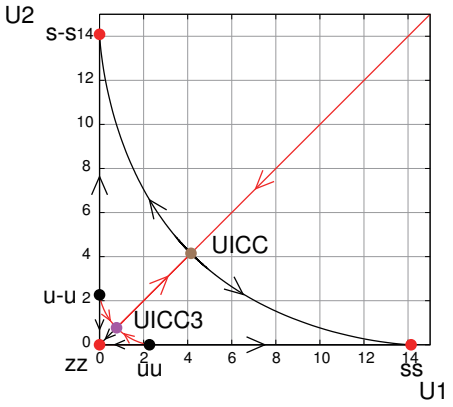

Figure 4.5: Phase plane diagram obtained from the averaged equation (4.3) for $\beta = 4.10$.

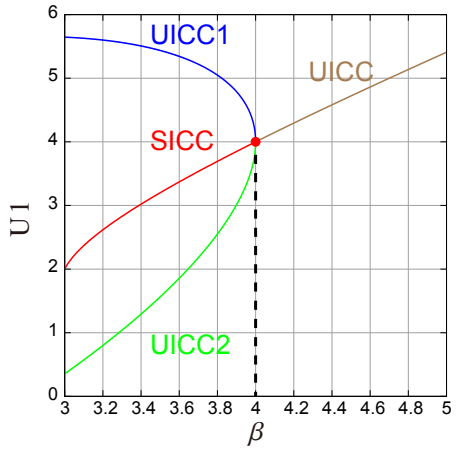

Figure 4.6: Subcritical pitchfork bifurcation obtained from equilibrium points of the averaged equation (4.3). The equilibrium points associated with the "SICC" (red), the "UICC1" (blue), and the "UICC2" (green) coalesce into the "UICC" (brown) at $\beta = 4.00$ as β is increased.

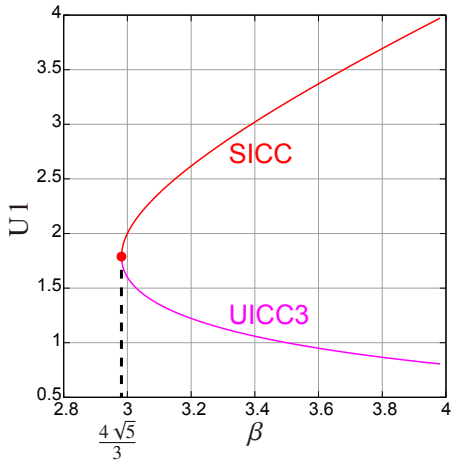

Figure 4.7: Saddle-node bifurcation obtained from equilibrium points of the averaged equation (4.3). The equilibrium points associated with the "SICC" (red) and the "UICC3" (violet) coalesce and disappear at $\beta = 4\sqrt{5}/3 \approx 2.98$ as β is decreased.

4.3 Numerical confirmation of saddle-node and pitchfork bifurcations for small $\epsilon(= 0.1)$

In this section, we will confirm the results of the averaging method obtained in the previous section by drawing directly stable and unstable invariant closed curves. First, we will rewrite Eq. (4.1) in the following scalar form:

$$\begin{cases} \dot{x}_0 &= x_1, \\ \dot{x}_1 &= -\epsilon(1-\beta x_0^2+x_0^4)x_1-(1-\alpha)x_0+\alpha(x_2-2x_0+x_2), \\ \dot{x}_2 &= x_3, \\ \dot{x}_3 &= -\epsilon(1-\beta x_2^2+x_2^4)x_3-(1-\alpha)x_2+\alpha(x_0-2x_2+x_0). \end{cases} \tag{4.4}$$

where $x_1(x_2)$ in Eq. (4.1) is replaced by $x_0(x_2)$. Next, we introduce a Poincaré section at $x_1 = 0$ (- to +) and consider a mapped point in the (x_0, x_2, x_3)-space. In the following ϵ is set as 0.1 so that the results can be compared with those from the averaging method.

Figure 4.8 presents a transition diagram obtained from Eq. (4.4) in the following manner. We choose a set of $(\alpha,\beta) = (0.13, 3.2)$ (* mark) to realize the "SICC" first, and increase β by using the continuation method. Then, the "SICC" jumps to the "ss" or the "s-s" for a certain value of β. Next, we decrease β from $\beta = 3.2$ via the continuation method. Then, we obtain the "zz" for a certain value of β. For all possible α, we record the various attractor types (the "SICC," the "ss," the "s-s," the "zz," etc.) that materialize, and assign a color to each type. Some colors in the grey (the "SICC") region denote periodic solutions with various periods. In particular, the green region presents the period-2 solution which consists of two mode frequencies $\sqrt{1-\alpha}$ and $\sqrt{1+3\alpha}$ synchronized with 1:2 ratio.

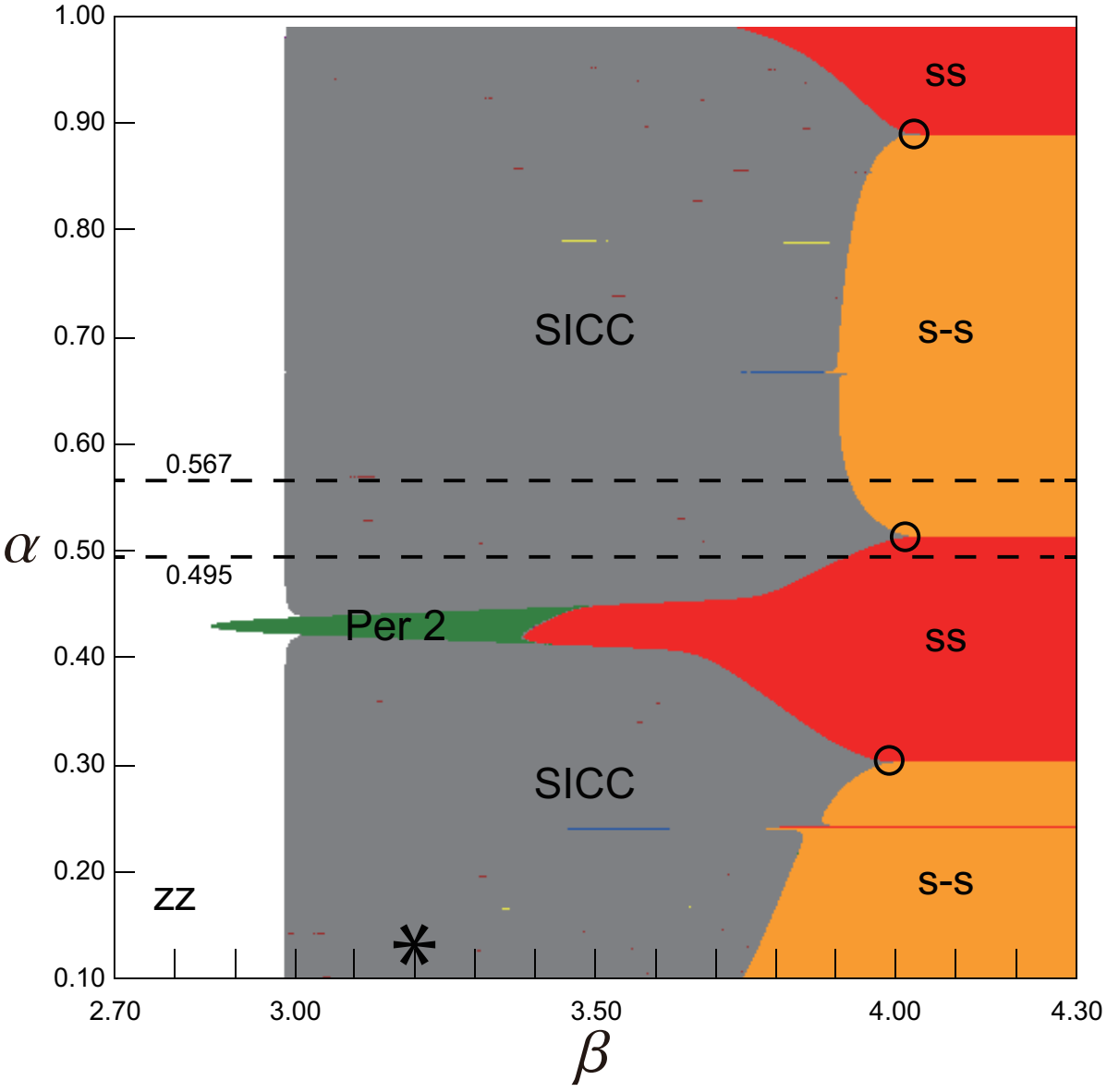

Figure 4.8: Transition diagram from the "SICC" (grey) to the "ss" or the "s-s" as β is increased and to "zz" as β is decreased in the (α,β)-plane for $\epsilon = 0.1$. The green region denotes the period-2 solution regime. Various colors in the grey region denote periodic solutions. The "$*$" denotes the starting point of simulation. The PF bifurcations occur, at least, at the encircled "$\bigcirc$" points.

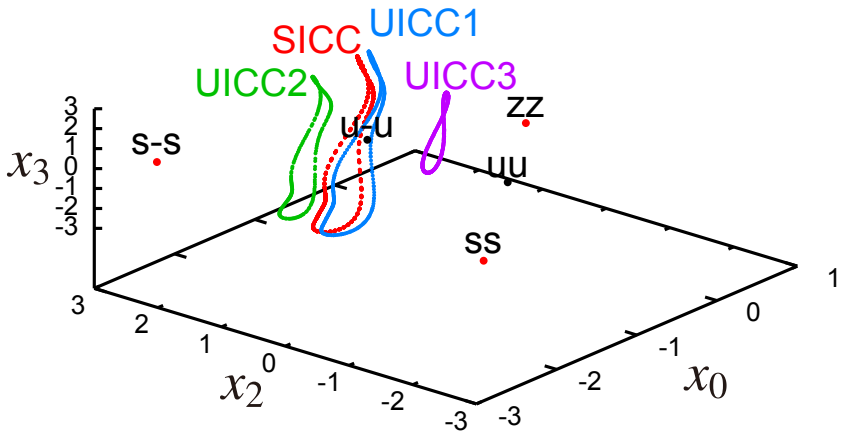

(a)

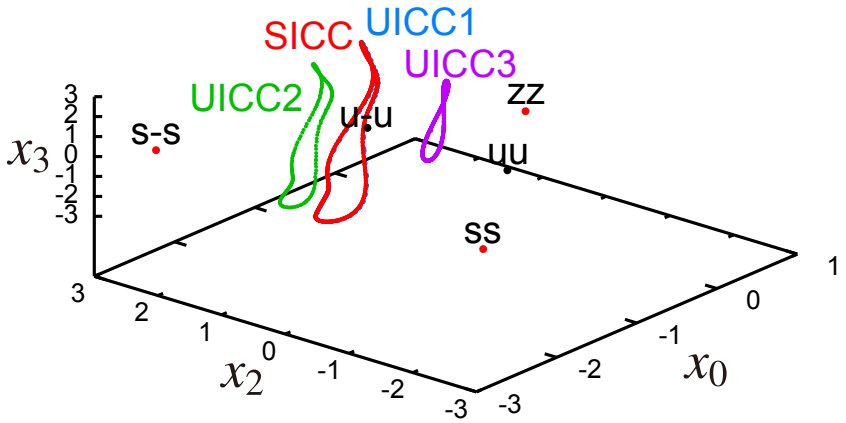

(b)

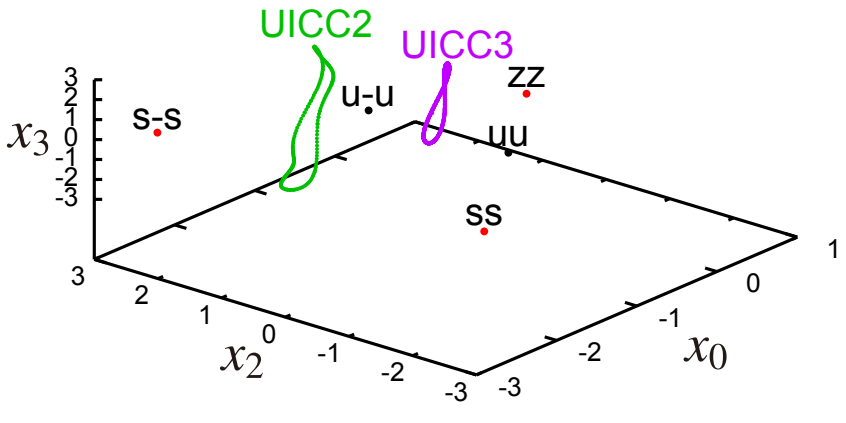

(c)

Figure 4.9: Saddle-node bifurcation of the quasi-periodic attractor for $\alpha = 0.495$ and $\epsilon = 0.1$: the "SICC" (red) incorporates with the "UICC1" (blue) and disappears as β is increased. (a) Before the SN bifurcation for $\beta = 3.898$ (b) At the SN bifurcation for $\beta = 3.909$ (c) After the SN bifurcation for $\beta = 3.910$. The green colored closed curve associates with the "UICC2" and violet colored closed curve associates with the "UICC3."

From this figure, we notice that as β is decreased, the "SICC" jumps to the "zz" at $\beta \simeq 2.98$ for all values of α as expected from the averaging method (predicted value: $\beta = 4\sqrt{5}/3 \simeq 2.98$). However, as β is increased, the "SICC" jumps to the "ss" or the "s-s" depending on the value of α. This result cannot be explained from averaging method. In particular, what happens at the border of "ss" and "s-s." This will be clarified as following.

Figure 4.9 represents the relationship between the "UICC1," the "SICC," and the "UICC2" for $\alpha = 0.495$. Figure 4.9(a) represents them for $\beta = 3.898$ in which the "SICC" and the "UICC1" are close but still some distance apart. Figure 4.9(b) represents them for $\beta = 3.909$ in which they almost overlap. Therefore, for $\beta = 3.910 (> 3.909)$ the quasi-periodic attractor "SICC" and the quasi-periodic saddle "UICC1" disappear as demonstrated in Fig. 4.9(c). This is a demonstration of the saddle-node (SN) bifurcation of the "SICC" and the "UICC1." After the SN bifurcation, two quasi-periodic saddles, the "UICC2" and the "UICC3" are left as seen in Fig. 4.9(c). The "UICC2" is in the basin boundary of the "ss" and the "s-s," and the "UICC3" is in the basin boundary of the "zz" and the "ss." After all, as we observe the "SICC" by increasing β using the continuation method for $\alpha = 0.495$, the "SICC" jumps to the "ss" after the SN bifurcation for $\beta = 3.910$ [6].

Figure 4.10 represents the relationship between the "UICC1," the "SICC," and the "UICC2" for $\alpha = 0.567$. Figure 4.10(a) represents them for $\beta = 3.90$ in which the "SICC" and the "UICC2" are close but still some distance apart. Figure 4.10(b) represents them for $\beta = 3.9075$ in which they almost overlap. Therefore, for $\beta = 3.910$ the quasi-periodic attractor the "SICC" and quasi-periodic saddle the "UICC2" disappear via the SN bifurcation as shown in Fig. 4.10(c). After the SN bifurcation, two quasi-periodic saddles the "UICC1" and the "UICC3" are left. The "UICC1" is in the basin boundary of the "ss" and the "s-s," and the "UICC3" is in the basin boundary of the "zz" and the "s-s." After all, as we trace the "SICC" by increasing β via the continuation method for $\alpha = 0.567$, the "SICC" jumps to the "s-s" after the SN bifurcation for $\beta = 0.3910$ [7].

Figure 4.11 represents the situation just before the SN bifurcation of the "SICC" and the "UICC3" for three values of $\alpha = 0.1(\beta = 2.985), 0.5(\beta = 2.982)$ and $0.9(\beta = 2.982)$. After they disappear, the "SICC" jumps to the "zz," and the "UICC1" and the "UICC2" are left in the basin boundary separating the "s-s" and the "zz" and the basin boundary separating the "ss" and the "zz," respectively.

[6] The reason the "SICC" jumps to the "ss" is clear from the schematic diagram in Fig. 4.15(a). In this case, the initial condition is above the "UICC2" in the basin of the "ss."

[7] The reason the "SICC" jumps in this case to the "s-s" is that the initial condition (a node representing the "SICC") is below the "UICC1" in the basin of the "s-s" as seen in Fig. 4.15(c).

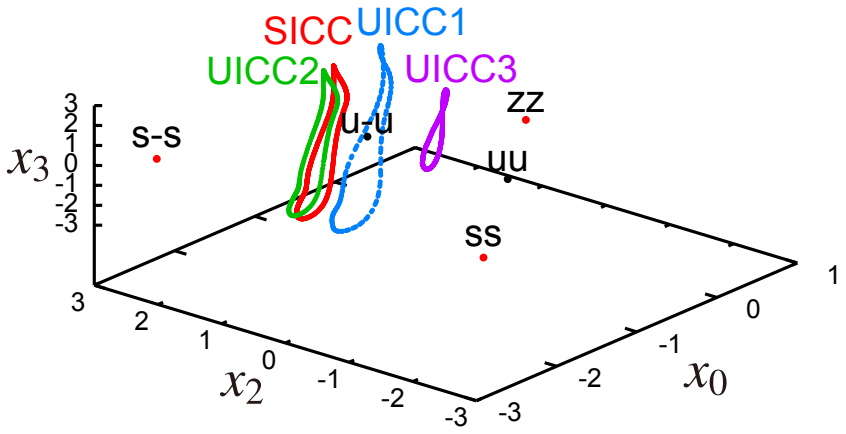

(a)

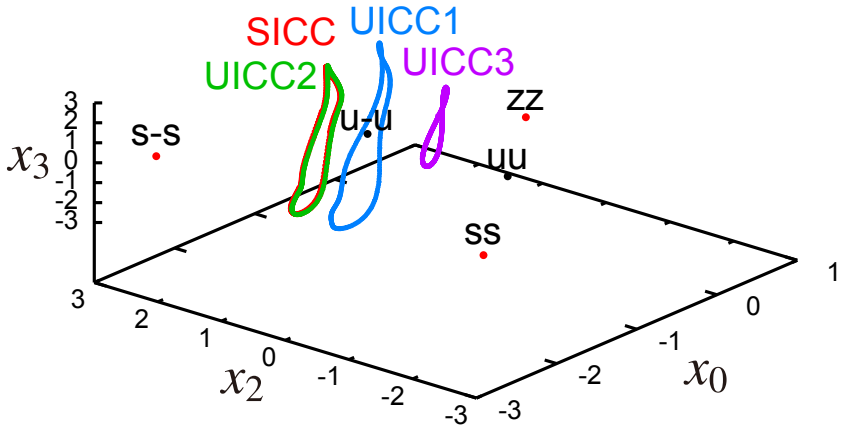

(b)

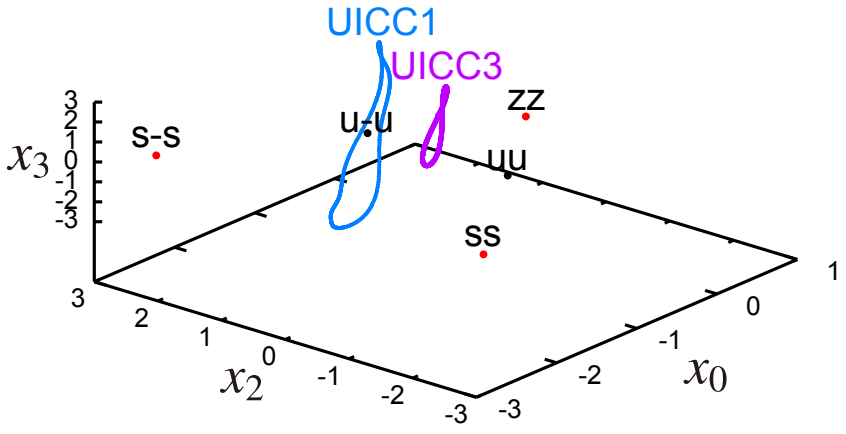

(c)

Figure 4.10: Saddle-node bifurcation of the quasi-periodic attractor for $\alpha = 0.567$ and $\epsilon = 0.1$: the "SICC" (red) incorporates with the "UICC2" (green) and disappears as β is increased. (a) Before the SN bifurcation for $\beta = 3.9000$ (b) At the SN bifurcation for $\beta = 3.9075$ (c) After the SN bifurcation for $\beta = 3.9100$ Blue colored closed curve associates with the "UICC1" and violet colored closed curve associates with the "UICC3."

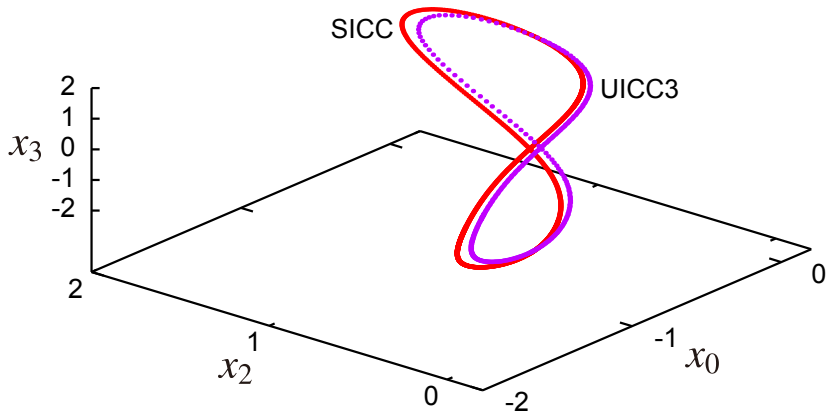

(a)

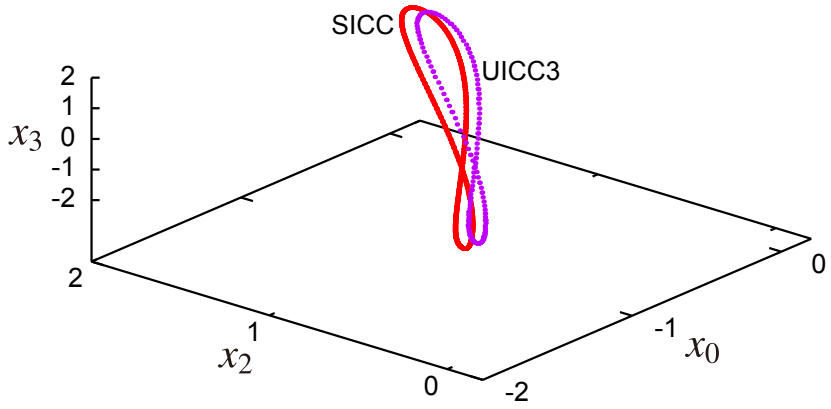

(b)

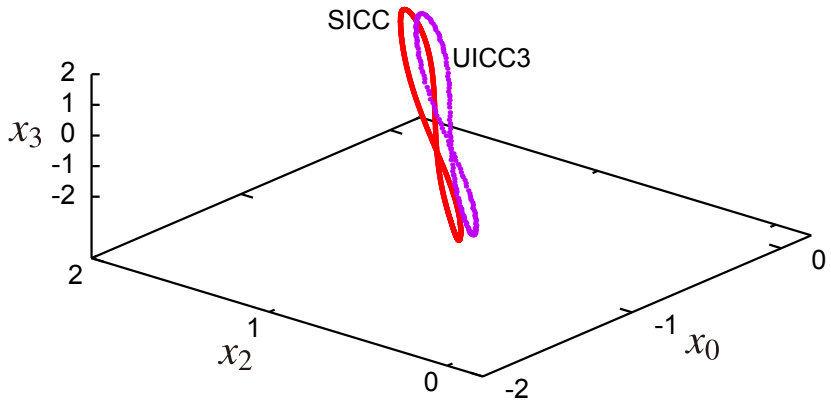

(c)

Figure 4.11: Situation just before saddle-node bifurcation of quasi-periodic attractor for three α values. The "SICC" (red) incorporates with the "UICC3" (violet). (a) $(\alpha, \beta) = (0.1, 2.985)$ (b) $(\alpha, \beta) = (0.5, 2.982)$ (c) $(\alpha, \beta) = (0.9, 2.982)$. The "UICC1" and the "UICC2" are eliminated for simplicity.

Figure 4.12 represents the situation just before the simultaneous disappearance of the "uu," the "ss," and the "UICC1" (the "u-u," the "s-s," and the "UICC2") via the degenerate SN and Neimark-Sacker (NS) bifurcations [8]. After their disappearance, there are no attractors and saddles left, except for the "zz." Therefore, all flows converge to zero.

Next, we investigate the pitchfork (PF) bifurcation that occurs near $\alpha = 0.30, 0.51$, and 0.89. For example, we will confirm the existence of a pitchfork bifurcation around $\alpha = 0.51$. Figure 4.13 shows the situation just before the PF bifurcation where the "SICC" is sandwiched between the "UICC1" and the "UICC2" for $\alpha = 0.5124$ and $\beta = 3.99$. However, if we increase β by a small amount, either the "UICC1" or the "UICC2" comes closer to the "SICC," and eventually we will see an SN bifurcation. That is, the PF bifurcation is very sensitive to small changes in α. Therefore, let us consider a different method. Figure 4.14(a) shows the overlapped representation of the "UICC2" (green) before the SN bifurcation ($\beta = 3.985$) and the "UICCX" (light blue) after the SN bifurcation ($\beta = 3.990$) for $\alpha = 0.511$. Figure 4.14(b) shows the overlapped representation of the "UICC1" (blue) before the SN bifurcation ($\beta = 3.996$) and the "UICCX" (light blue) after the SN bifurcation ($\beta = 3.999$) for $\alpha = 0.513$. Note that the "UICC2" is smoothly connected to the "UICCX" for $\alpha = 0.511$; therefore, the "UICCX" can be regarded as a natural extension of the "UICC2." In the same manner, the "UICCX" can be regarded as a natural extension of the "UICC1" for $\alpha = 0.513$. The SN bifurcation for $\alpha = 0.511$ corresponds to the schematic diagram of Fig. 4.15(a) and for $\alpha = 0.513$ to that of Fig. 4.15(c); therefore, we can prove the existence of a PF bifurcation as shown in Fig. 4.15(b) for a value of α between 0.511 and 0.513.

From the averaging theory, the "SICC," the "UICC1," and the "UICC2" coalesce into the "UICC" via the PF bifurcation for all α values satisfying $0 \leq \alpha \leq 1$. However, the SN bifurcation occurs instead of the PF bifurcation for almost all values of α in the direct computer simulation except for some special α values including the above three. This is an interesting discrepancy between the averaging method result and the direct computer simulation result. We conjecture that this discrepancy results from the symmetric property of the fundamental Eq. 4.4. That is, if we introduce a slight asymmetry between the two oscillators, the PF bifurcation in the averaged equation is resolved and the SN bifurcation will appear instead. Figure 4.16(a) and (b) represent computer-generated bifurcation diagrams before and after the PF bifurcation for $\alpha = 0.511$ and $\alpha = 0.513$, respectively. Explicitly, the maximum value of $x_0(t) + x_2(t)$ with respect to t in the corresponding stable and unstable quasi-periodic oscillations is shown in the vertical direction in terms of β. This result agrees with the schematic diagram in Fig. 4.15.

[8] The reason such degenerate bifurcation occurs is that the system Eq. 4.4 has the symmetric property. This follows from the fact that we coupled two "identical" oscillators. If we assume each oscillator's shunt capacitor C in Fig .4.1(b) is different such as C_1 and C_2, the degeneracy can be resolved as explained in Appendix B.

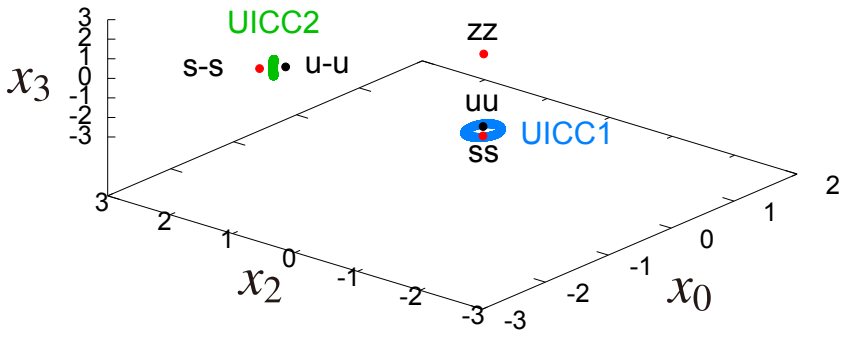

Figure 4.12: Invariant curves and fixed points just before disappearance of the "uu," the "ss," and the "UICC1" (the "u-u," the "s-s," and the "UICC2") via degenerate SN and NS bifurcations.

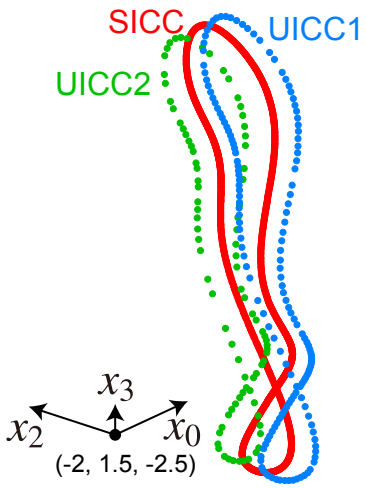

Figure 4.13: Near a pitchfork bifurcation of the quasi-periodic attractor for $\alpha = 0.5124$ and $\beta = 3.99$ and $\epsilon = 0.1$. The "SICC" (red) incorporates with the "UICC1" (green) and the "UICC2" (blue).

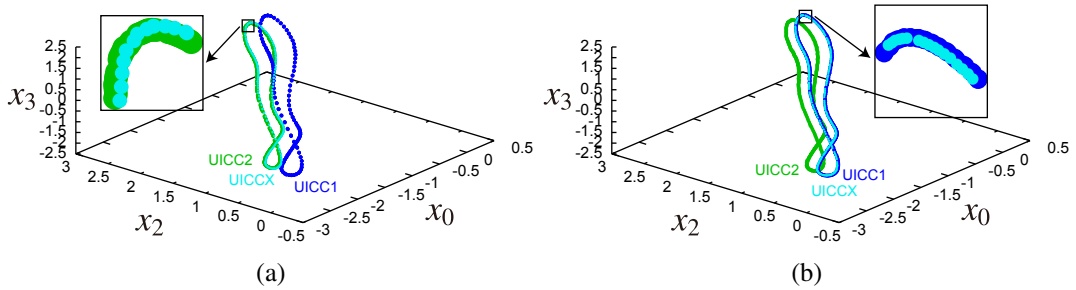

Figure 4.14: Interchange of saddle-node pair in terms of α for $\epsilon = 0.1$. Only related UICCs are drawn to avoid confusion. (a) Overlapped representation of the "UICC2"(green) for $\beta = 3.985$ (just before the SN bifurcation) and the "UICCX" (light blue) for $\beta = 3.990$ (just after the SN bifurcation) for $\alpha = 0.511$. The "UICC2"and the "UICCX" are almost identical; therefore, the "UICCX" can be considered as an extension of the "UICC2." (b) Overlapped representation of the "UICC1"(blue) for $\beta = 3.996$ (just before SN bifurcation) and the "UICCX" (light blue) for $\beta = 3.999$ (just after SN bifurcation) for $\alpha = 0.513$. The "UICC1" and the "UICCX" are almost identical; therefore, the "UICCX" can be considered as an extension of the "UICC1."

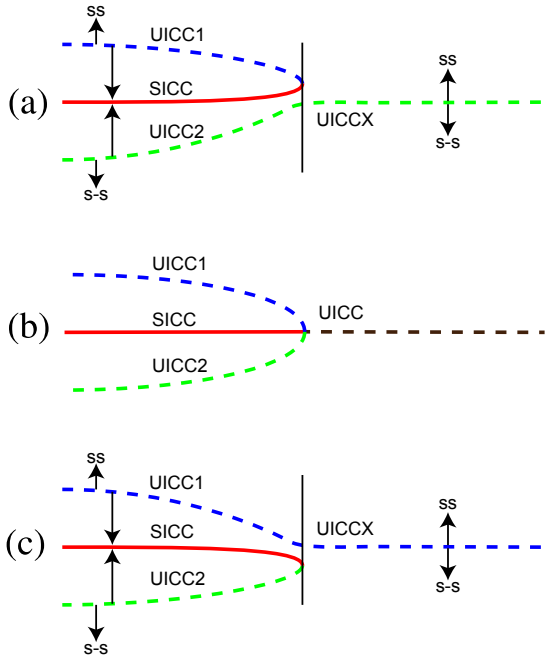

Figure 4.15: Schematic diagrams representing interchange of the branch around pitchfork bifurcation in terms of α (a) $\alpha = 0.511 < \alpha_{PF}$ (b) $\alpha = \alpha_{PF}$ (c) $\alpha = 0.513 > \alpha_{PF}$ Vertical : $MAX(x_0(t) + x_2(t))$ Horizontal : β

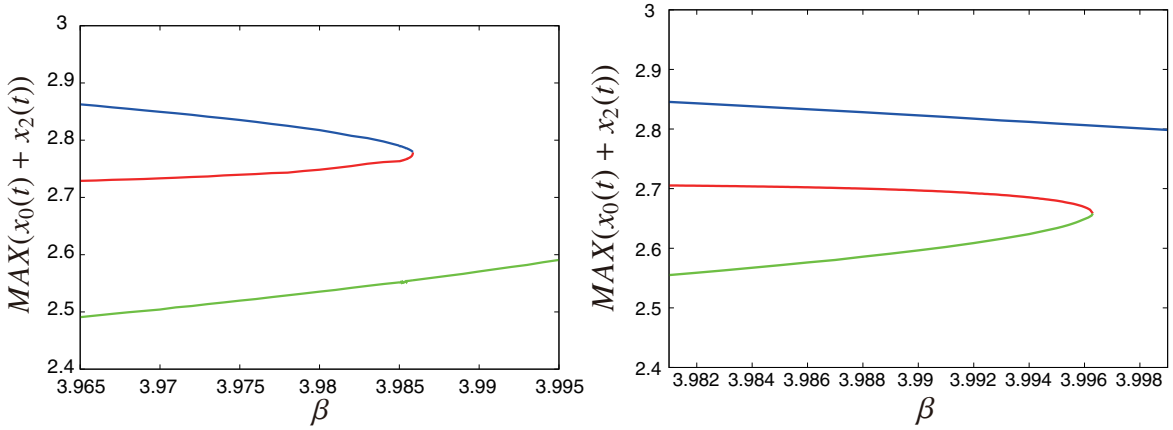

Figure 4.16: Computer simulation results of β versus $MAX(x_0(t) + x_2(t))$ representing interchange of branch before and after the pitchfork bifurcation. (a) $\alpha = 0.511$ (corresp. to Fig. 4.15(a)) (b) $\alpha = 0.513$ (corresp. to Fig. 4.15(c)) The "UICC1," the "SICC," and the "UICC2" are denoted by blue, red and green curves, respectively.

4.4 Transition for larger value of ϵ (= 0.36)

In this section we briefly state the results for a larger value of ϵ (= 0.36). Figure 4.17 shows the computer generated transition diagram obtained by applying the "brute force" method for $\epsilon = 0.36$ in the same procedure as in Fig. 4.8. This diagram shows the transition from the "SICC" to the "ss" or the "s-s" (or the "zz") in the (α, β)-plane as β is increased or decreased. The green region denotes the regime of the period-2 solution consisting of the 1/2-phase locking solution of two mode frequencies. Various colored regions such as the blue region, denote small periodic regimes. Compared to the similar diagram in Fig. 4.8 for $\epsilon = 0.1$, more periodic solutions appear; in particular, the green region for the period-2 solution expands considerably. This is because of the increased nonlinearity. As in Fig. 4.8, the transition from the "SICC" to the "ss" or the "s-s" is due to the SN bifurcation, except for the special α values where the PF bifurcation occurs. Figure 4.18(a) and (b) show the situations just before and

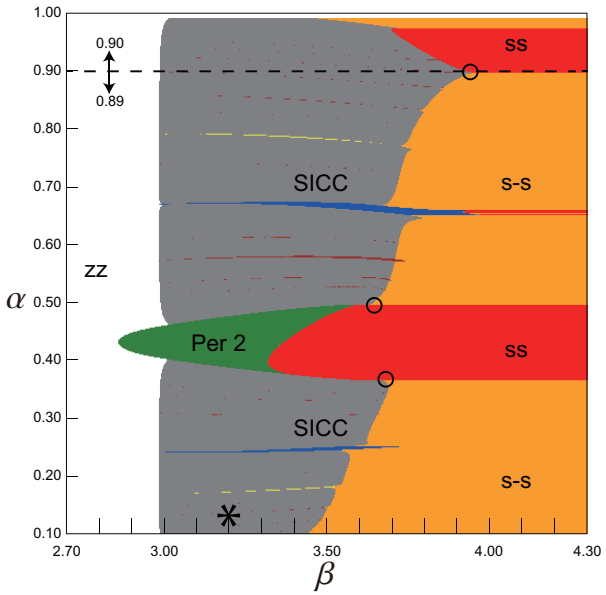

Figure 4.17: Transition diagram from the "SICC" (grey) to the "ss" or the "s-s" in the (α, β)-plane as β is increased for $\epsilon = 0.36$. Green region denotes the regime of the period-2 solution. Other colored regions denote periodic solutions. The meaning of "$*$" and "$\bigcirc$" is the same as that of Fig. 4.8.

after the SN bifurcation of the "SICC" and the "UICC2" for $\alpha = 0.89$. Figure 4.18(a) and (b) show the situations just before and after the SN bifurcation of the "SICC" and the "UICC1" for $\alpha = 0.90$. The corresponding "UICC" is interchanged in $0.89 < \alpha < 0.90$; therefore the PF bifurcation is expected in-between.

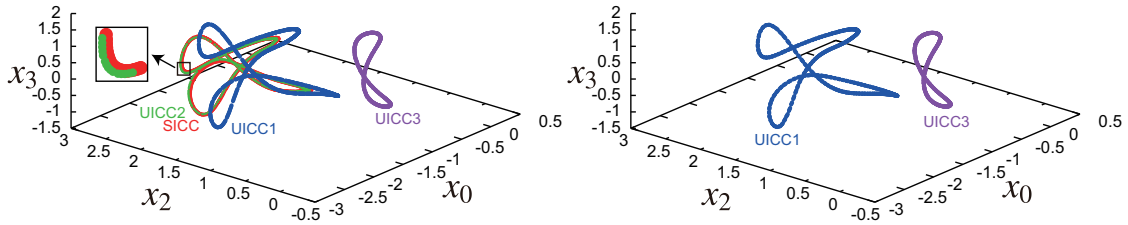

(a) (b)

Figure 4.18: Saddle-node bifurcation of the quasi-periodic attractor for $\alpha = 0.89$ ($\epsilon = 0.36$): the "SICC" (red) incorporates with tthe "UICC2" (green) and disappears as β is increased. (a) Before the bifurcation for $\beta = 3.917$. (b) After the bifurcation for $\beta = 3.920$. The blue colored closed curve associates with the "UICC1" and the violet colored closed curve associates with the "UICC3."

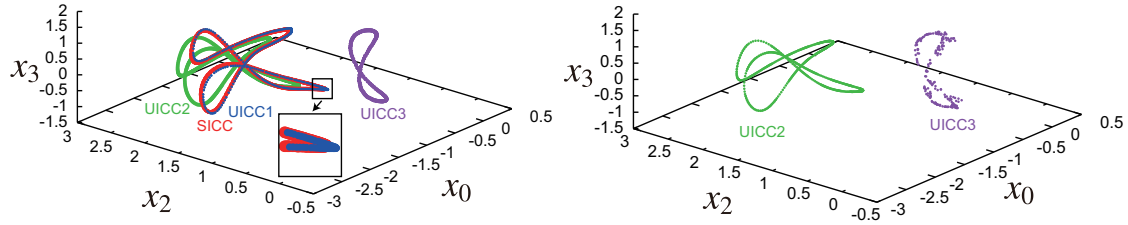

(a) (b)

Figure 4.19: The saddle-node bifurcation of the quasi-periodic attractor for $\alpha = 0.90$ ($\epsilon = 0.36$): the "SICC" (red) incorporates with the "UICC1" (blue) and disappears as β is increased. (a) Before the bifurcation for $\beta = 3.905$. (b) After the bifurcation for $\beta = 3.912$. The green colored closed curve associates with the "UICC2" and the violet colored closed curve associates with the "UICC3."

4.5 Conclusion

In this chapter, we use our new method to demonstrate unstable quasi-periodic oscillations (the "UICC"). This method is based on the Nusse and Yorke algorithm for obtaining chaotic saddles [19]. The system we investigate consists of the mutually coupled oscillators shown in Fig. 4.1 which was already investigated via the averaging method. The saddle equilibrium points in the phase plane of the averaged equation correspond to the UICC. Therefore, we have succeeded in reproducing various SN bifurcations predicted by the averaging method, by directly solving the system Eq. 4.4. One of the new results is that the PF bifurcation, which is predicted by the averaging method for all values of α, cannot occur except for special values of α. Instead, the SN bifurcation can be seen for almost all values of α. In the future, we will apply this method to higher-order systems for further validation.

Acknowledgement

The work of the second author (M. Komuro) was partially supported by the Aihara Project, the FIRST program from JSPS, initiated by CSTP. The authors would like to thank Dr. Miki U. Kobayashi (FIRST, Aihara Innovative Mathematical Modelling Project, Japan Science and Technology Agency) and Prof. Tsuyoshi Mizuguchi from Osaka Prefecture University for giving us invaluable information regarding chaotic saddles.

Appendix 4.A The method to obtain an unstable invariant curve on Poincaré map

Here, we will briefly explain the method to obtain an unstable invariant closed curve (the UICC) on the Poincaré section. So far, this method is valid for the UICC with a one-dimensional instability. There is an UICC or a saddle in the basin boundary of the two attractors. Therefore, if we map a point close to the basin boundary in such a manner that mapped points do not diverge towards an unstable direction, we can, in principle, trace the UICC. Although different from the shooting algorithm (Newton method) for obtaining a fixed point on a Poincaré section, we cannot pursuit the UICC via the gradient algorithm. Therefore, we must use an algorithm based on the bisection method, which takes more time as compared to the shooting algorithm. Figure 4.20 presents the schematic diagram explaining our idea. First, we pick up

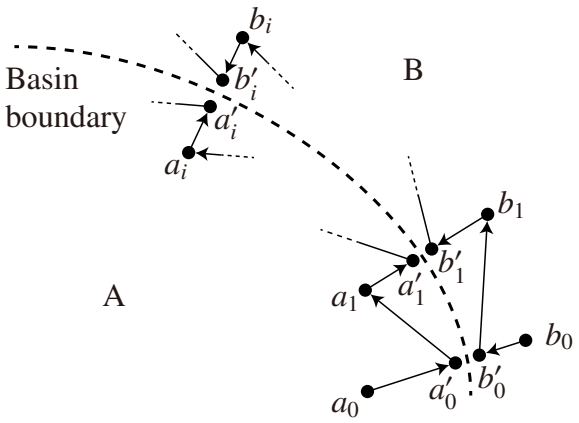

Figure 4.20: Schematic diagram showing algorithm for tracing an "UICC."

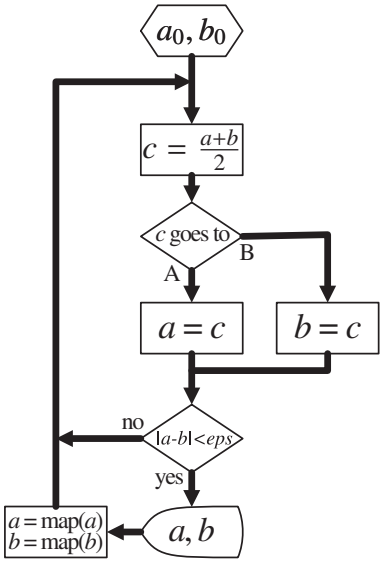

Figure 4.21: Flow chart for tracing an "UICC."

two points a_0 and b_0, where $a_0(b_0)$ is selected in the basin of the attractor A (B). Next, we try to approximate these two points to the basin boundary by using the bisection algorithm. That is, if mapped points starting from the middle point of a_0 and b_0 move to the attractor A, we

replace a_0 by the middle point and vice versa. Repeating this process untill the distance between a_0 and b_0 becomes less than eps, we rename $a_0(b_0)$ by a'_0 (b'_0). Since $a_1(b_1)$, the mapped point of $a'_0(b'_0)$, is in the basin of attractor A (B), we can apply the bisection algorithm again to a_1 and b_1. By repeating the bisection algorithm and the Poincaré mapping, we can calculate a UICC to within eps accuracy. Eventually, we can obtain a "UICC" or a saddle as the core of a basin boundary. Figure 4.21 presents a flow chart of the algorithm.

Appendix 4.B Unfolding of the degenerate bifurcation

If we assume that each oscillator's shunt capacitor C in Fig. 4.1(b) is not the same such as C_1 and C_2, the fourth equation of Eq. 4.4 can be modified as: $\dot{x}_3 = k^2[-\epsilon(1-\beta x_2^2 + x_2^4)x_3 - (1-\alpha)x_2 + \alpha(x_0 - 2x_2 + x_0)]$ where k^2 denotes C_1/C_2. Figure 4.22 presents a bifurcation diagram of the "ss," the "uu," and the "UICC1" as well as the "s-s," the "u-u," and the "UICC2" for the asymmetric case: $k^2 = 1.08$. That is, as β is increased from 2.86, the "uu" of index 3 and the

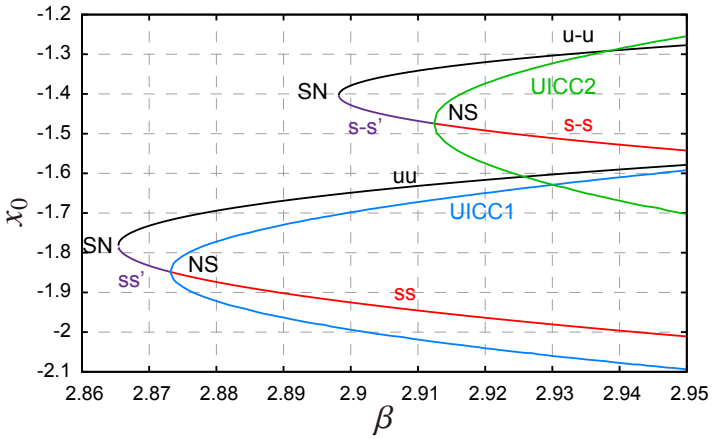

Figure 4.22: Bifurcation diagram of "ss," "uu" and "UICC1" as well as "s-s," "u-u" and "UICC2." SN presents saddle-node bifurcation and NS presents Neimark-Sacker bifurcation. Maximum and minimum values of $x_0(t)$ of the unstable invariant closed curves "UICC1" and "UICC2" are shown.

"ss′" of index 2 appear via the SN bifurcation. Note that at this stage, the "ss′" is unstable. Around $\beta \simeq 2.873$, the "ss′" becomes the "ss" of index 0 and the "UICC1" of index 1 via NS bifurcation. In the same manner, the "u-u" of index 3 and the "s-s′" of index 2 appear via the SN bifurcation around $\beta \simeq 2.898$, and vice versa. Note that the two SN bifurcation points as well as the two NS bifurcation points differ considerably due to the asymmetry. As k^2 approaches 1, these points coalesce into one point, and as a result, the "uu" of index 3, the "ss" of index 0, and the "UICC1" of index 1 as well as the "u-u" of index 3, the "s-s" of index 0, and the "UICC2" of index 1 appear and disappear at the same parameter value. This is the

degenerate bifurcation. The asymmetry has little influence over other bifurcations shown in Figs. 4.9–4.11, etc.

5 Bifurcation Analysis of the Quasi-Periodic Solution with Three-Phase Synchronized Envelopes in a Ring of Three-Coupled, Bistable Oscillator

In this study, we investigate the bifurcation of the quasi-periodic solution in a ring of three-coupled, bistable oscillators. The quasi-periodic solution under study is a propagating wave solution with three-phase synchronized envelope, and we name it as "$ICC3\phi$" which means invariant closed curve for which time waveforms have three-phase synchronized envelope. We obtain the two-parameter bifurcation diagram of $ICC3\phi$ with respect to the coupling factor α versus the nonlinear strength ϵ. Consequently, we detect several Arnold tongues showing various periodic solutions of $ICC3\phi$. By investigating bifurcation on the boundary of these Arnlod tongues, we clarify the transition from periodic to quasi-periodic solution of $ICC3\phi$ or the inverse. Specifically, the transition of the period-4, period-5, and period-7 solutions to $ICC3\phi$ is due to a saddle-node bifurcation, which has no hysteresis. In contrast, the transition from the period-3 solution to $ICC3\phi$ is a combination of subcritical pitchfork and heteroclinic bifurcations; hence, it has hysteresis. We draw diagrams showing the connection of unstable manifolds of heteroclinic bifurcation.

5.1 Introduction

Research on the wave-propagation phenomena observed in active transmission lines such as Soliton is important from theoretical and practical perspectives because of its nondecaying property, which can benefit information-transmission applications [3], [2]. Recently, [8] reported that by using computer simulations, a coupled-oscillator system with soft nonlinearity, which is a type of active transmission line, transmits a pulse wave under certain conditions. This result triggered our investigations of wave-propagation phenomena in a ring of coupled oscillators with hard nonlinearity [1] by using bifurcation analysis. First, we performed computer simulations of wave propagations in the P-coupled system for a large P[5], and then bifurcation analysis from a periodic (a standing wave) to a quasi-periodic solution (a propagating wave) or the inverse in the six-coupled system[6]. Our results showed that this transition

[1] In this study, we refer to a ring of P-coupled oscillators with hard nonlinearity as a P-coupled system.

was due to the combination of subcritical pitchfork (PF) and heteroclinic (HC) bifurcations [6],[20].

In this study, we investigate the bifurcation from a periodic to a quasi-periodic solution or its inverse in the three-coupled system. This quasi-periodic solution, whose time waveforms have three-phase synchronized envelopes, is a propagating wave found by[21] by using computer simulations. For simplicity, we refer to it as "$ICC3\phi$" in this study which means invariant closed curve for which time waveforms have three-phase synchronized envelope. We investigated the transition from the periodic to quasi-periodic solution of $ICC3\phi$ by drawing a two-parameter bifurcation diagram. Therefore, we verified that the transition was due to the following factors: 1) the saddle-node (SN) bifurcation and 2) the combination of subcritical PF and HC bifurcations. Thus, there are clear differences with the two-coupled system[21],[22]], in which only the former one could be detected.

5.2 Circuit and Differential Equation

Fig. 5.1 shows the circuit of a ring of the three-coupled system. Fig. 5.2 shows the circuit of a single bistable oscillator in which inductance (L), capacitance (C), and nonlinear conductance (NC) are connected in parallel. The voltage-current characteristics of NC can be written by using the following 5th power polynomial:

$$i_{NC} = g_1 v - g_3 v^3 + g_5 v^5, \quad g_1, g_3, g_5 > 0.$$

This is called hard nonlinearity. The oscillator with hard nonlinearity is bistable because both

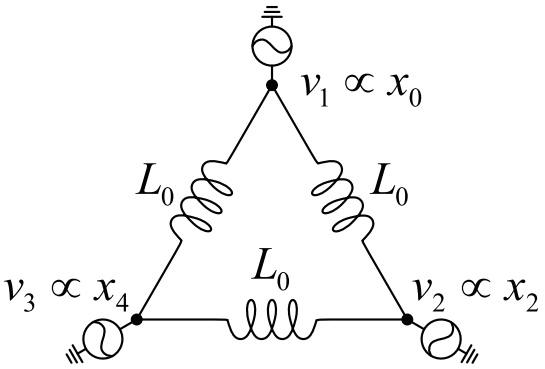

Figure 5.1: Ring of three-coupled, bistable oscillators.

the oscillation and no-oscillation states are possible.

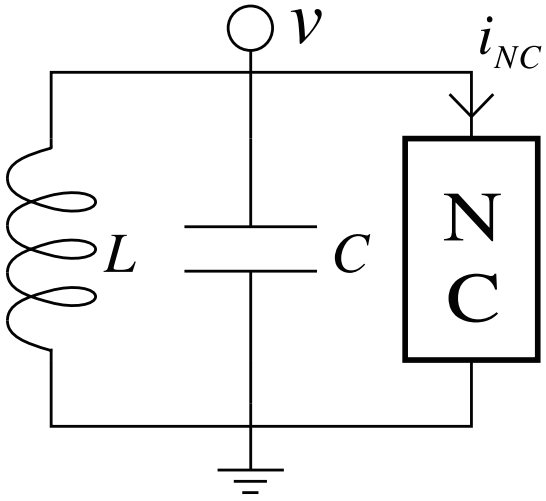

Figure 5.2: Bistable oscillator.

From Fig. 5.1 we can derive the normalized circuit equation as follows:

$$\begin{aligned}
\dot{x}_0 &= x_1 \\
\dot{x}_1 &= -\epsilon(1-\beta x_0^2+x_0^4)x_1 \\
&\quad -(1-\alpha)x_0+\alpha(x_4-2x_0+x_2) \\
\dot{x}_2 &= x_3 \\
\dot{x}_3 &= -\epsilon(1-\beta x_2^2+x_2^4)x_3 \\
&\quad -(1-\alpha)x_2+\alpha(x_0-2x_2+x_4) \\
\dot{x}_4 &= x_5 \\
\dot{x}_5 &= -\epsilon(1-\beta x_4^2+x_4^4)x_5 \\
&\quad -(1-\alpha)x_4+\alpha(x_2-2x_4+x_0)
\end{aligned} \tag{5.1}$$

where x_0, x_2 and x_4 are proportional to each oscillator's output voltage v_1, v_2 and v_3, respectively, and x_1, x_3, and x_5 are proportional to their time derivatives $\dot{v}_1, \dot{v}_2$, and $\dot{v}_3$, respectively. The parameter $\alpha(0 < \alpha < 1)$ is a coupling factor, the parameter $\beta(> 2\sqrt{2})$ controls the amplitude of oscillation, and the parameter ϵ represents the strength of the nonlinearity. Throughout this paper, ϵ and β are fixed to $\epsilon = 0.5$ and $\beta = 3.20$, respectively, except in Figs. 5.4 and 5.18.

All solutions (except for time waveforms) are shown in the local cross section:

$$\Sigma : \{(x_0, x_1, \cdots, x_5) \in R^6 | x_1 = 0, \dot{x}_1 < 0\}.$$

We consider a Poincare map $\mathrm{T} : \Sigma \to \Sigma : y_1 \mapsto y_2$ where $y_1 (\in R^5)$ is a point in Σ and $y_2 (\in R^5)$ is the next point in Σ in which the flow starting from y_1 again reaches Σ.

5.3 Two-parameter-bifurcation diagram of the quasi-periodic solution $ICC3\phi$

The propagating wave rotating clockwise and counter-clockwise along the three oscillators is generally a quasi-periodic solution. Given a comparatively large α and a proper initial condition, we can realize $ICC3\phi$ as shown in Fig. 5.3. The quasi-periodic solution $ICC3\phi$

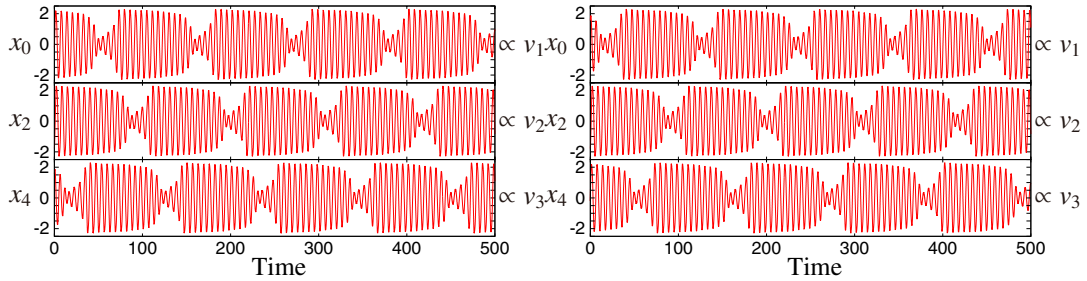

Figure 5.3: $ICC3\phi$ propagating (a) clockwise and (b) counter clockwise for $\alpha = 0.08$. The initial condition is given by $x_0(0) = 0.0, x_1(0) = -0.5, x_2(0) = -2.0, x_3(0) = 0.5, x_4(0) = -2.0$, and $x_5(0) = 0.0$ for (a), and $x_0(0) = -2.0, x_1(0) = 0.0, x_2(0) = -2.0, x_3(0) = 0.5, x_4(0) = 0.0$, and $x_5(0) = -0.5$ for (b).

presents frequency locking with various periodic solutions depending on the values of α and ϵ. To investigate the bifurcation of $ICC3\phi$ with respect to ϵ and α, we perform computer simulations by using the following procedure.

Step 1: Select $\epsilon = 0.01$ and $\alpha = 0.1$ to realize $ICC3\phi$.
Step 2: Setting ϵ as a constant, we vary α to be $0.01 \leq \alpha \leq 1.00$ with a step size of 0.001 by using the continuation method[23] to trace $ICC3\phi$ in the direction of α. We memorize the initial conditions of $ICC3\phi$ for all values of (ϵ, α).
Step 3: Starting from the memorized initial conditions, we vary ϵ to be $0.01 \leq \epsilon \leq 1.00$ with a step size of 0.001 by using the continuation method to trace $ICC3\phi$ in the direction of ϵ.
Step 4: We differentiate between the periodic and quasi-periodic solutions as follows: Take the initial point on an attractor, repeat the mapping N times, and measure the distance between the initial and N-mapped points. If the distance is adequately small after mapping for N-times, we consider this solution as N-periodic. If N is greater than 30, we stop mapping and consider the solution as quasi-periodic.

In this way, we check all solutions in the form of $ICC3\phi$ in the designated (ϵ, α) region. The result is given in Fig. 5.4. When α is varied, we note that many Arnold tongues representing the periodic solutions such as the period-3, period-4, period-5, and period-7 (abbreviated as P3, P4, P5 and P7, respectively) appear. These periodic solutions emerge when the frequency components of the quasi-periodic solution $ICC3\phi$ are entrained. In subsequent sections, we show that the bifurcation at the boundary of the periodic solutions P4, P5, and P7 and the

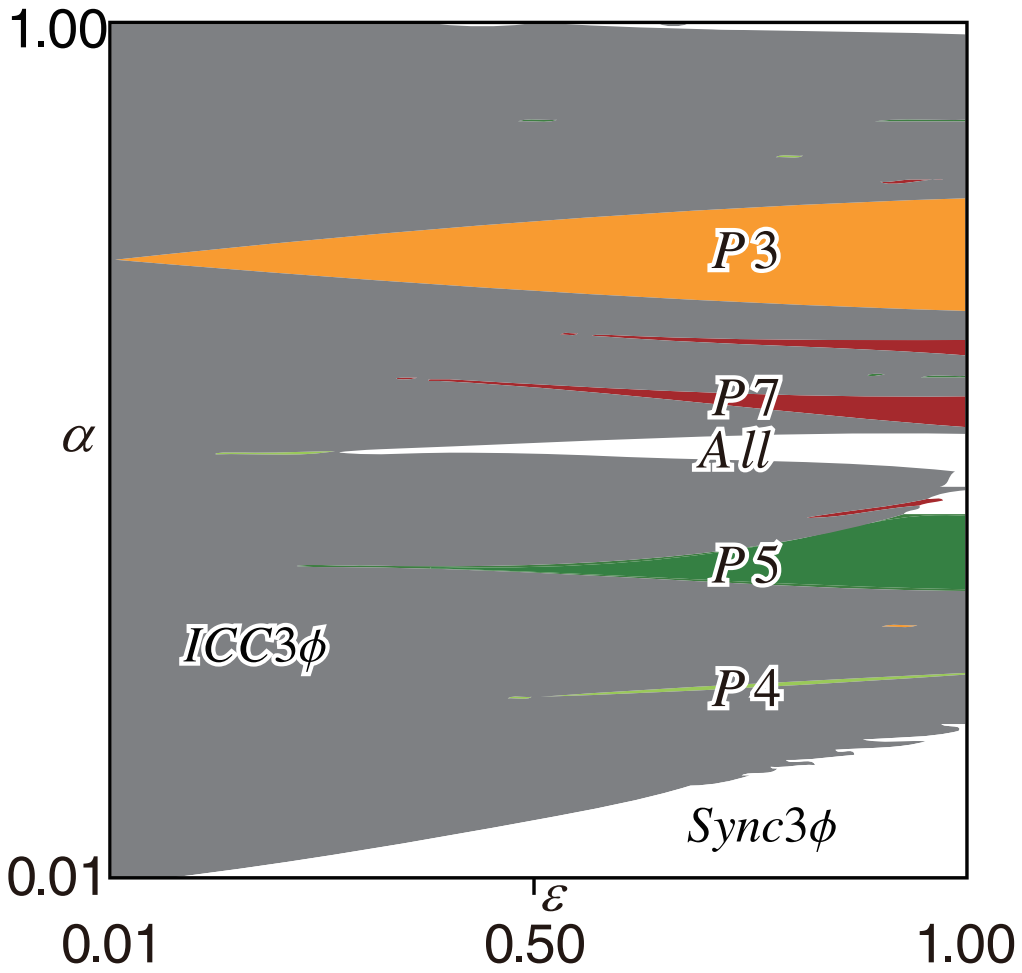

Figure 5.4: Two-parameter (ϵ,α) bifurcation diagram of the quasi-periodic solution $ICC3\phi$ and the k-periodic solution P_k for $\beta = 3.2$.

quasi-periodic solution $ICC3\phi$ is entirely SN bifurcation; therefore, there is no hysteresis. On the contrary, the bifurcation at the boundary of P3 (both the upper and lower ones), is the subcritical PF bifurcation and exhibits hysteresis. In Sections 5.4 and 5.5, we investigate this in detail. In addition, the $Sync3\phi$, which is the three-phase synchronized periodic solution, and the All, which is the same-phase synchronized periodic solution, are not the periodic solutions resulting from the frequency locking of $ICC3\phi$. Specifically, $ICC3\phi$ is eliminated at that boundary and jumps to $Sync3\phi$ and the All. Therefore, they are irreversible.

5.4 Transition from P5 to $ICC3\phi$ (SN bifurcation)

We investigate the transition from P5 to $ICC3\phi$ or its inverse as an example[24]. The same type of bifurcation can be obtained for P4 and P7. Fig. 5.5 shows a one-parameter-bifurcation diagram of P5 and $ICC3\phi$, in which P5 emerges exactly after $ICC3\phi$ disappears. In this

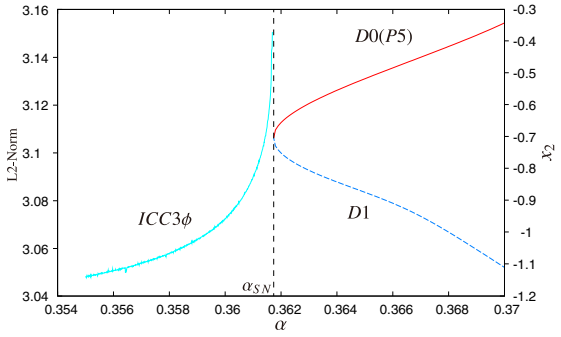

Figure 5.5: One-parameter-bifurcation diagram of the periodic solution period-5 (P5) and the quasi-periodic solution $ICC3\phi$ in terms of α. The $D0(P5)$ denotes the stable P5 solution, and $D1$ denotes the index 1 saddle. $ICC3\phi$ is expressed as a maximum of the L2-norm. All solutions are obtained by using the five-times iterated Poincare map T^5.

bifurcation diagram $ICC3\phi$ is represented by the maximum value of the L2-norm [2]. The transition from $D0(P5)$ [3] to $ICC3\phi$ or its inverse has no gap and no overlap, and hence, this transition is reversible without hysteresis. Fig. 5.6 shows the time waveforms of the periodic solution P5 with $2\pi/3$ rotational symmetry. In Fig. 5.7, the ◯ points represent the periodic

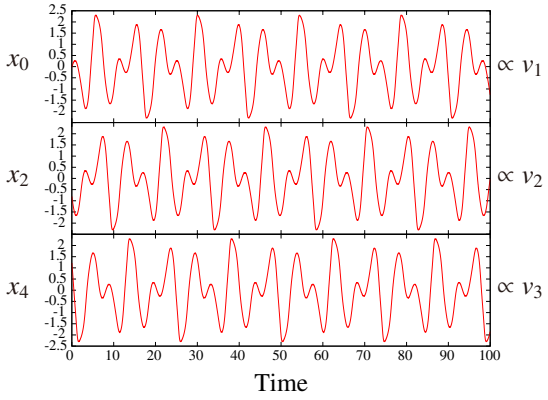

Figure 5.6: Time waveforms of the periodic solution P5 with $2\pi/3$ rotational symmetry for $\alpha = 0.69$.

solution P5 exactly before SN bifurcation, and the closed curve represents the quasi-periodic solution $ICC3\phi$ exactly after SN bifurcation. In Fig. 5.7, the ◯ points are distributed on the closed curve, which is an additional evidence that the transition between the periodic and the quasi-periodic solutions is reversible. Fig. 5.8 shows an expression of the Discrete

[2] The L2-norm of the quasi-periodic solution is represented by the following equation: L2-norm = $(x_0^2 + x_2^2 + x_3^2 + x_4^2 + x_5^2)^{0.5}$ where $x_k, k = 0, 2, 3, 4, 5$ is the state variable on the local cross section Σ.

[3] Throughout this paper, D_k denotes that the index (unstable dimension) is k-dimensional. Therefore, D_0 is a stable node.

Fourier Transform (DFT) co-ordinate system (Appendix 5.A). We observe that the solution has rotational symmetry, and hence, there is no co-existing solution [4]. This bifurcation is of the same type as that reported in [21], and [22] for the two-coupled system, and henceforth, we call this bifurcation as the "birth and death of the quasi-periodic solution via the SN cycle."

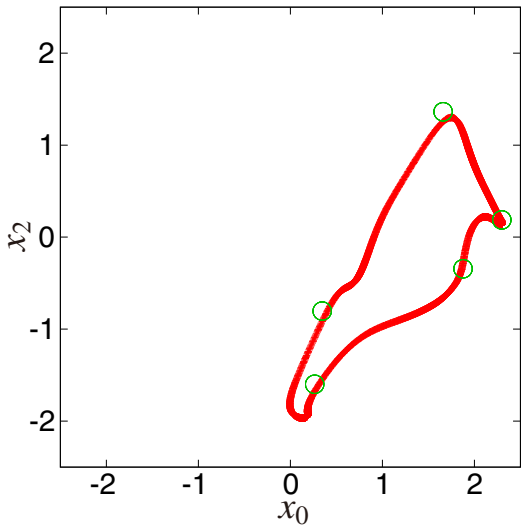

Figure 5.7: Overlapped presentation of the periodic solution P5 exactly before saddle-node (SN) bifurcation (◯ mark; $\alpha = 0.37$) and the quasi-periodic solution $ICC3\phi$ exactly after SN bifurcation (closed curve; $\alpha = 0.36$) represented on the local cross section Σ around the boundary of the P5 Arnold tongue. P5 and $ICC3\phi$ are projected onto the (x_0, x_2) plane.

[4] $ICC3\phi$ and P5 are both clockwise and counter clockwise. Here we treat only the clockwise ones. Therefore, if we consider both directions, the other solution co-exists.

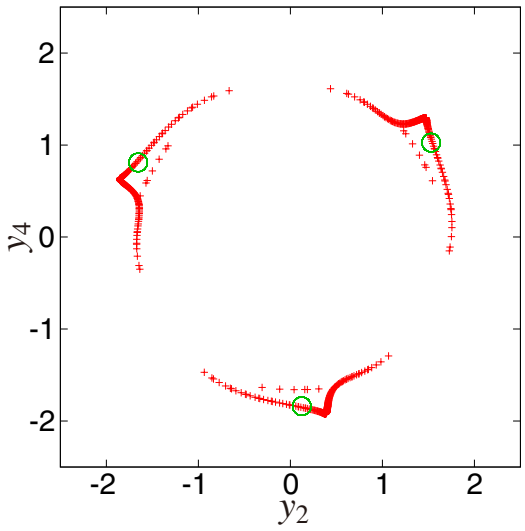

Figure 5.8: Discrete Fourier Transform (DFT) representation of the attractors of Fig. 5.7 projected onto the (y_2, y_4) plane. The ◯ marks and closed curve have the same parameter values as those in Fig. 5.7.

5.5 Transition from P3 to $ICC3\phi$ (PF and HC bifurcations)

Next, we investigate the bifurcation from the periodic solution P3 to the quasi-periodic solution $ICC3\phi$[24]. This type of bifurcation is different from the SN cycle stated in the previous section.

5.5.1 Attractors on the Poincare map

Fig. 5.9 shows the one-parameter-bifurcation diagram in terms of α representing $ICC3\phi$ and the P3. There is an overlapping region between them ($\alpha_{PF} < \alpha < \alpha_c$), and hence, a hysteresis

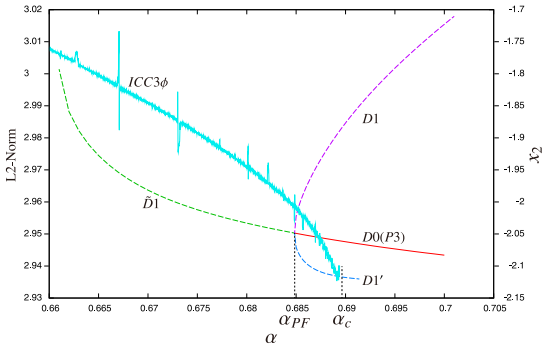

Figure 5.9: One-parameter-bifurcation diagram of the periodic solution P3 and the quasi-periodic solution $ICC3\phi$ in terms of α. The $D0(P3)$ denotes the stable period-3 (P3) solution. $ICC3\phi$ is expressed by the maximum value of the L2-norm. All solutions are obtained from the three-times iterated Poincare map T^3.

exists in the transition between the quasi-periodic solution $ICC3\phi$ and the periodic solution P3. Specifically, when α is decreased, a stable P3 becomes unstable via the subcritical PF bifurcation at α_{PF}, and it jumps to the stable $ICC3\phi$. Next, when α is increased, the stable $ICC3\phi$ disappears via the HC bifurcation at α_c, and it jumps back to the stable periodic solution P3. $D1$ and $D1'$ denote the two unstable branches of the subcritical PF bifurcation. Fig. 5.10 shows the time waveforms of the periodic solution P3, where x_4 is different from x_0 and x_2. Fig. 5.11 shows the periodic solution P3 (◯ points) exactly before the subcritical PF bifurcation and $ICC3\phi$ (closed curve) exactly after the subcritical PF bifurcation. Fig. 5.12 shows the same ones in DFT representation. The ◯ points are not on the closed curve in Fig. 5.11, which confirms that the transitions of these two solutions are irreversible. Further, as opposed to what was observed in Fig. 5.8, the periodic solution P3 in DFT representation of Fig. 5.12 is only one point. This means that the time waveform of the periodic solution P3 in Fig. 5.10 does not have the rotational symmetry. Therefore, the three solutions coexist for P3.

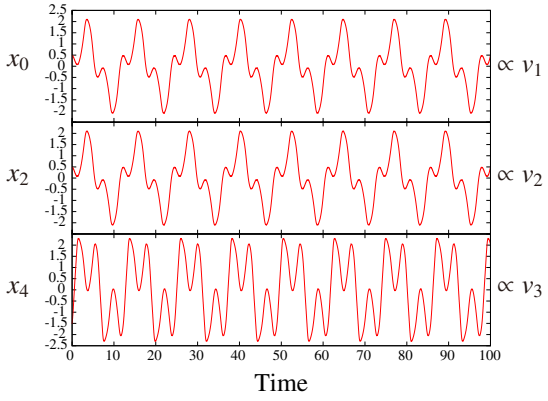

Figure 5.10: Time waveforms inside the P3 Arnold tongue for $\alpha = 0.69$.

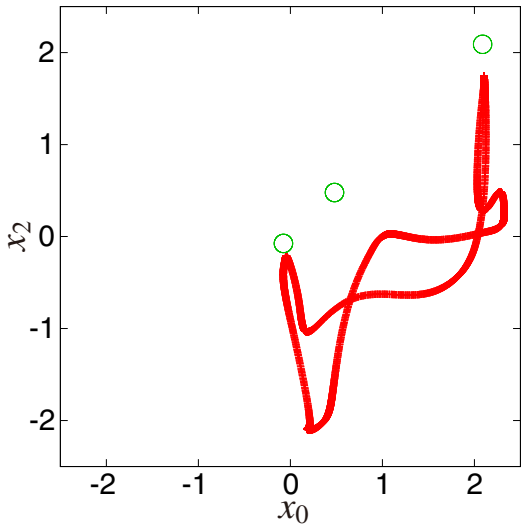

Figure 5.11: Overlapped presentation of the periodic solution P3 exactly before the subcritical PF bifurcation (◯ mark; $\alpha = 0.69$) and the quasi-periodic solution $ICC3\phi$ exactly after the subcritical PF bifurcation (closed curve; $\alpha = 0.68$) represented on the local cross section Σ near the boundary of the P3 Arnold tongue. P3 and $ICC3\phi$ are projected onto the (x_0, x_2) plane.

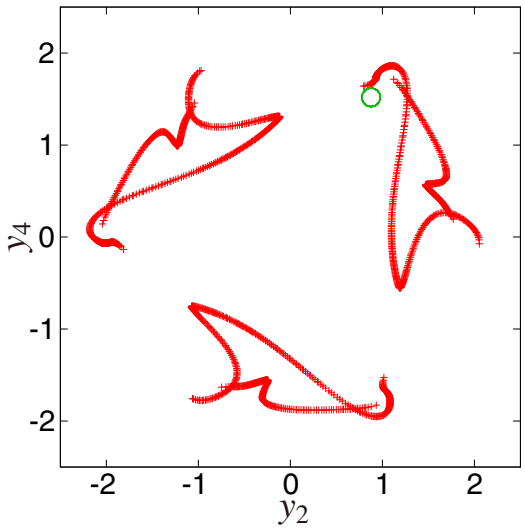

Figure 5.12: DFT representation of the attractors of Fig. 5.11 projected onto the (y_2, y_4) plane. The ◯ mark and closed curve have the same parameter values as those in Fig. 5.11.

Next, we will investigate the small parameter region including α_c. From microscopic observations, α_c, which is both the death- and birth-parameter value of $ICC3\phi$, consists of two points α_{c1} and α_{c2}, at which the HC tangency (Appendix 5.C) occurs on the local cross section Σ. Therefore, for $\alpha_{c1} < \alpha < \alpha_{c2}$, there is an HC tangle, which induces complicated dynamics [11]. In the next subsection, we will investigate the behavior of the unstable manifolds (UM) of the saddle fixed points $D1$ and $D1'$ in Fig. 5.9 near α_{c1} and α_{c2}.

5.5.2 Connection of UMs in relation to α

Because $D0(P3)$ in Fig. 5.10 is a P3 node with three co-existing solutions, we use the following notation; ${}^{j}N_i^3$ where the upper-right superscript "3" denotes the P3 solution, the subscript $i(=1,2,3)$ denotes the order of movement in the P3 solution, and the upper-left superscript $j(=1,2,3)$ denotes the number assigned to the three coexisting periodic solutions. Similarly, $D1$ and $D1'$ are expressed as ${}^{j}_{k}D_i^3$ where the lower-left subscript $k = 1$ denotes $D1$, and $k = 2$ denotes $D1'$.

Fig. 5.13 shows the schematic of UMs connecting all the nodes and saddles for $\alpha > \alpha_{c2}$. For example, one of the UMs of ${}^{1}_{1}D_1^3,{}^{1}_{2}D_1^3,{}^{3}_{2}D_1^3$, and ${}^{2}_{1}D_1^3$ converges to ${}^{1}N_1^3$, and one of the UMs

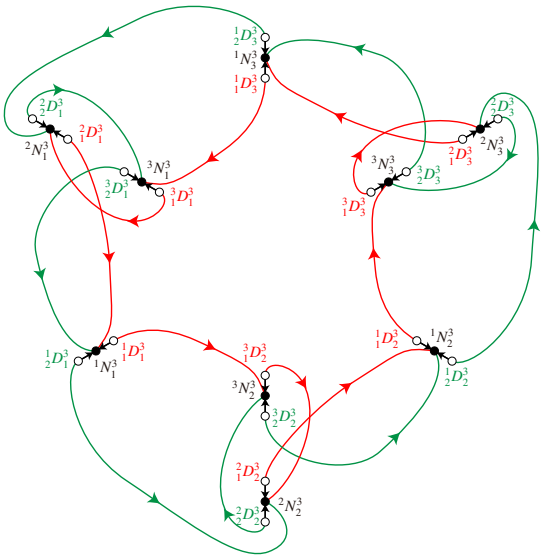

Figure 5.13: Schematic showing the connection of UMs with saddles and nodes for $\alpha > \alpha_{c2}$. The arrows indicate the direction of UMs.

of ${}^{2}_{2}D_1^3,{}^{2}_{1}D_1^3,{}^{1}_{2}D_3^3$, and ${}^{3}_{1}D_1^3$ converges to ${}^{2}N_1^3$, and one of the UMs of ${}^{3}_{1}D_1^3,{}^{3}_{2}D_1^3,{}^{2}_{2}D_1^3$, and ${}^{1}_{1}D_3^3$ converges to ${}^{3}N_1^3$. In general, two UMs from a pair of saddles ${}^{j}_{1}D_i^3$ and ${}^{j}_{2}D_i^3$ converge to ${}^{j}N_i^3$ (the PF pair node), and other two UMs results from other saddles for $i, j = 1,2,3$. The node ${}^{j}N_i^3$ for $i = 1,2,3$ corresponds to (one of three) $D0(P3)$, and the saddles ${}^{j}_{1}D_i^3$ and ${}^{j}_{2}D_i^3$ for $i = 1,2,3$ correspond to (one of three) $D1$ and $D1'$, repectively, in Fig. 5.9. In this case, the mapped points converge to one of three sets of the P3 nodes: $({}^{1}N_1^3, {}^{1}N_2^3, {}^{1}N_3^3)$, $({}^{2}N_1^3, {}^{2}N_2^3, {}^{2}N_3^3)$, $({}^{3}N_1^3, {}^{3}N_2^3, {}^{3}N_3^3)$.

Fig. 5.14 shows the schematic of UMs connecting all the nodes and saddles for $\alpha < \alpha_{c1}$. In

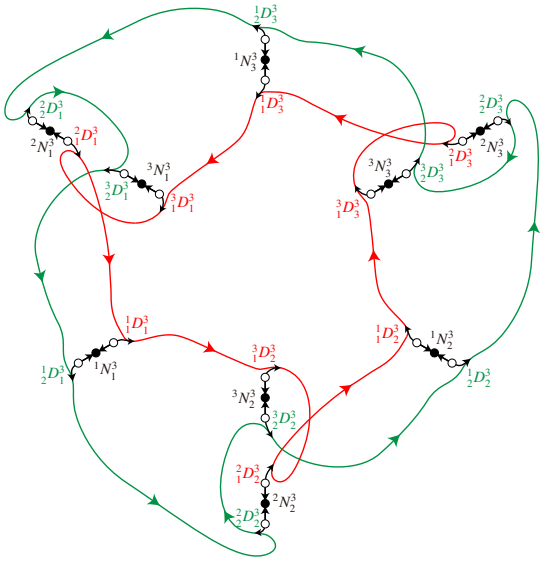

Figure 5.14: Schematic showing the connection of UMs with saddles and nodes for $\alpha < \alpha_{c1}$. The green curve represents $ICC3\phi CL$, and the red curve represents the $ICC3\phi CCL$. The arrows indicate the direction of UMs.

this case, one of the two UMs of each saddle approaches toward the PF pair node, and the other UM converges with one of the two $ICC3\phi$. There coexist two $ICC3\phi$'s, one of which rotates clockwise, and the other counter clockwise. Hereafter, we call the former one as $ICC3\phi CL$ and the latter one as $ICC3\phi CCL$. $ICC3\phi$ represented by the green curve passes through the neighborhood of saddles in the following order:

$$\rightarrow {}^{2}_{2}D^{3}_{1} \rightarrow {}^{3}_{2}D^{3}_{1} \rightarrow {}^{1}_{2}D^{3}_{1}| \rightarrow {}^{2}_{2}D^{3}_{2} \rightarrow {}^{3}_{2}D^{3}_{2} \rightarrow {}^{1}_{2}D^{3}_{2}| \rightarrow {}^{2}_{2}D^{3}_{3} \rightarrow {}^{3}_{2}D^{3}_{3} \rightarrow {}^{1}_{2}D^{3}_{3}| \rightarrow$$

This corresponds to$ICC3\phi CL$ whose time waveforms v_1, v_2, and v_3 rotate clockwise, as shown in Fig. 5.3a. Similarly, $ICC3\phi$ represented by the red curve passes through the neighborhood of the saddles in the following order:

$$\rightarrow {}^{3}_{1}D^{3}_{1} \rightarrow {}^{2}_{1}D^{3}_{1} \rightarrow {}^{1}_{1}D^{3}_{1}| \rightarrow {}^{3}_{1}D^{3}_{2} \rightarrow {}^{2}_{1}D^{3}_{2} \rightarrow {}^{1}_{1}D^{3}_{2}| \rightarrow {}^{3}_{1}D^{3}_{3} \rightarrow {}^{2}_{1}D^{3}_{3} \rightarrow {}^{1}_{1}D^{3}_{3}| \rightarrow$$

This is related to $ICC3\phi CCL$ whose time waveforms v_1, v_2, and v_3 rotate counter clockwise, as observed in Fig. 5.3b. Thus, the mapped points converge with either of the two $ICC3\phi$'s or one of the three sets of nodes mentioned above for $\alpha < \alpha_{c1}$.

Fig. 5.15 illustrates a schematic of UMs for $\alpha_{c1} < \alpha < \alpha_{c2}$; namely, one of the UMs of a saddle approaches toward the PF pair node directly, and the other UM fluctuates significantly as it approaches the next saddle. The UM of the previous saddle forms an HC tangle with the stable manifold (SM) of the subsequent saddle (Appendix 5.C). In this case, the mapped points indicate the sensitive dependence on the initial condition/parameter variation before converging with one of three sets of the above mentioned P3 nodes.

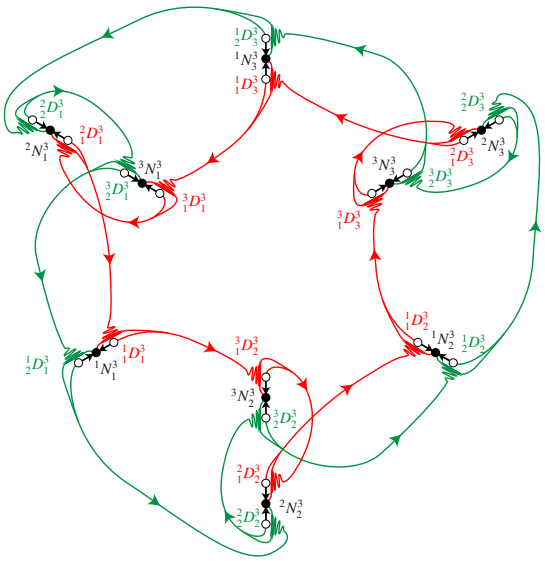

Figure 5.15: Schematic showing the connection of UMs with saddles and nodes for $\alpha_{c1} < \alpha < \alpha_{c2}$. The heteroclinic (HC) tangle appears near the saddles. The arrows indicate the direction of UMs starting from a saddle. In this case, the tip of UM fluctuates forward and backward while being compressed via the HC tangle. Therefore, the direction of UM will change during process.

Fig. 5.16 shows the numerical-calculation result of actual UMs ($\in R^5$) projected onto the (x_2, x_4) plane for $\alpha = 0.68520 (< \alpha_{c1})$. The green curve corresponds to $ICC3\phi CL$, and the red curve corresponds to $ICC3\phi CCL$. The positions of the nodes and saddles, and the shape of $ICC3\phi$ significantly differ from those in the schematic in Fig. 5.14. However, the connection of nodes and saddles are the same in the two figures.

Fig. 5.17 shows the numerical-calculation results of UMs from ${}^{2}_{1}D^{3}_{1}$ for three values of α, namely; 0.68964 (red) $< \alpha_{c1} <$ 0.68967 (blue) $< \alpha_{c2} <$ 0.68971 (green). This is a magnified diagram of the square region in Fig. 5.16. It is evident that UM for $\alpha < \alpha_{c1}$ (red curve) fluctuates near the saddle ${}^{1}_{1}D^{3}_{1}$ and approaches toward $ICC3\phi CCL$. UM for $\alpha > \alpha_{c2}$ (green curve) fluctuates near the same saddle and approaches toward ${}^{1}N^{3}_{1}$. UM for $\alpha_{c1} < \alpha < \alpha_{c2}$ fluctuates near ${}^{1}_{1}D^{3}_{1}$, and it is stretched in the two directions of UM of ${}^{1}_{1}D^{3}_{1}$. In this case, HC tangle occurs[5]. This is the mechanism behind the appearance and disappearance of $ICC3\phi$, which is the propagating-wave solution. We call this bifurcation as the "birth and death of the quasi-periodic solution via the HC cycle."

[5] Unfortunately, we are unable to show SM because it is four dimensional. However, the transversal intersection of SM and UM is evident because UM is stretched in "two" directions.

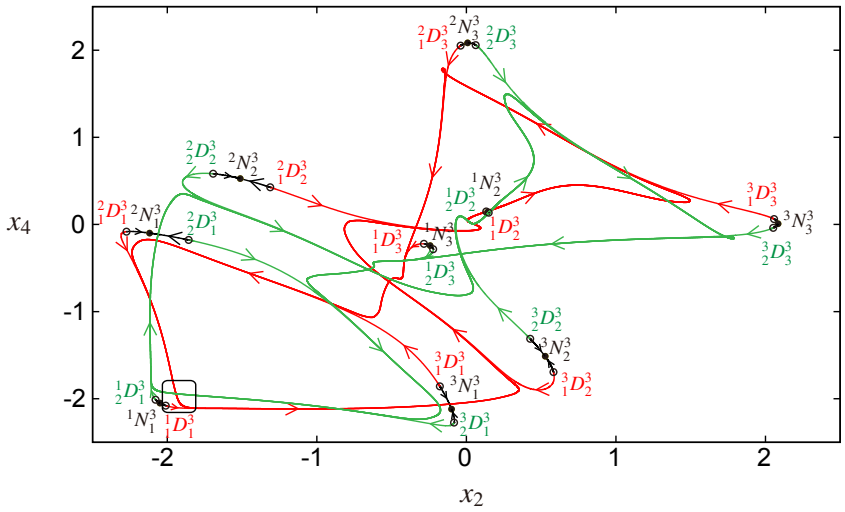

Figure 5.16: Numerically calculated actual UMs ($\in R^5$) projected onto the (x_2, x_4) plane by using the T^3 map for $\alpha = 0.68520 < \alpha_{c1}$. The green curve corresponds to the $ICC3\phi CL$, and the red curve corresponds to the $ICC3\phi CCL$.

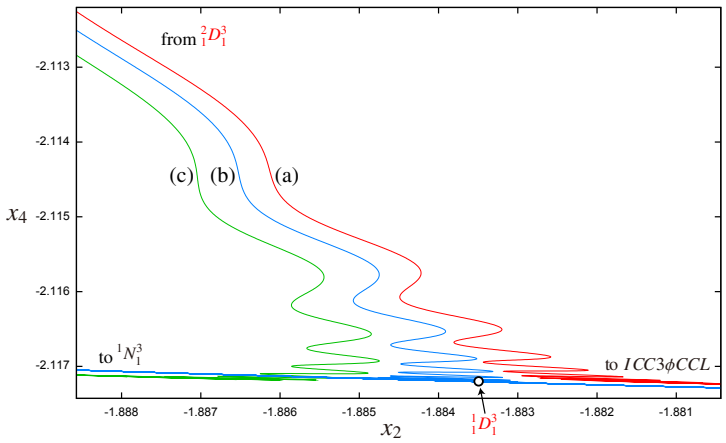

Figure 5.17: Magnified diagram in the square region of Fig. 5.16 for three different values of α : (a) 0.68964 (red curve) $< \alpha_{c1} <$ (b) 0.68967 (blue curve) $< \alpha_{c2} <$ (c) 0.68971 (green curve).

5.6 Conclusions

We investigated two bifurcation scenarios for the birth and death of the quasi-periodic solution $ICC3\phi$, whose envelopes are synchronized with three phases in the three-coupled system. Our results confirm that the bifurcation of $ICC3\phi$ is not always from SN cycle, but it is also from HC cycle. The new results found in this study can be summarized as follows:
1. The quasi-periodic solution $ICC3\phi$, which is the propagating wave's solution, cannot occur from the P1 solution in the form of a standing wave, in which one or two oscillators oscillate while others do not (Appendix 5.B). This is different from the cases of two-coupled and six-coupled systems shown in [21],[22],[6], and [20], in which the quasi-periodic solution in the form of the propagating wave occurs via SN or PF bifurcations from the above P1 solution.
2. The transition between $ICC3\phi$ and the P4, P5 and P7 solutions is due to SN bifurcation, and hence, it has no hysteresis. In contrast, the transition between $ICC3\phi$ and the P3 solution is due to the combination of the subcritical PF and HC bifurcations, and hence, it has hysteresis. The latter bifurcation scenario was not observed in the two-coupled system, and it was first detected in the three-coupled system as the number of oscillators was increased from two.
3. The transition between $ICC3\phi$ and three-phase synchronized periodic solution ("$Sync3\phi$" in Fig. 5.4) and that between $ICC3\phi$ and the same-phase periodic solution ("All" in Fig. 5.4) occurs because of the extinction of $ICC3\phi$. This is a jump phenomenon to other attractors, and hence, it is irreversible.
4. The HC cycle in the three-coupled system appears in both the upper and lower boundaries of the P3 region. In contrast, the HC cycle in the six-coupled system [6], [20] appears only in the upper boundary (no lower boundary).
5. The behavior of UM near the HC tangle can be verified by using schematics and actual numerical calculations.

In [21], the authors insisted that there existed a quasi-periodic solution in the two-, three-, and four-coupled systems. Moreover, they insisted that the bifurcation mechanism of the two-coupled system was equivalent to the SN cycle of the P1 solution, in which one oscillator oscillated, and the other oscillator did not oscillate. However, they did not clarify the mechanism behind the occurrence of the quasi-periodic solution $ICC3\phi$ in the three-coupled system (they only showed computer-simulation results). In [22], same as that in [21], only the occurrence of the quasi-periodic solution via the SN cycle for the two-coupled system was investigated. In [6] and [20], the authors investigated the onset mechanism of the quasi-periodic solution (the propagating wave) via the HC cycle in the six-coupled system. In the six-coupled system, HC bifurcation was observed when the coupling factor α was increased from zero, However, in this three-coupled system, HC bifurcation was observed when α is increased or decreased around a relatively large value of $\alpha = 0.72$, as noted above. From a physical perspective, $ICC3\phi$ in the three-coupled system appeared via the frequency unlocking of periodic solutions; therefore, it occurred when α is both increased and decreased. In contrast, the periodic solutions observed in the two-coupled and six-coupled systems were the "standing waves," which existed only for small α and did not originate from the frequency locking of the quasi-periodic solution. Therefore, the transition to the propagating wave solution occurred only when α was increased from zero. In future, we will investigate the extinction mechanism of the quasi-periodic solution of $ICC3\phi$ by capturing the unstable quasi-periodic solutions.

Appendix 5.A Representation in the Discrete Fourier Transform (DFT) coordinate system

The DFT coordinate system is frequently used to observe the position of flows in the system with rotational symmetry such as (1). The transformation can be represented by the following equations for the three-coupled system. Note that the attractors exhibit the $2\pi/3$ rotational symmetry. In this study, the local cross section is a hyper plane of $y_1 = 0$ with $\dot{y}_1 < 0$.

$$\begin{aligned}
y_0 &= x_0 + x_2 + x_4 \\
y_1 &= x_1 + x_3 + x_5 \\
y_2 &= x_0 \cos(2\pi \times 1 \times 0/3) \\
&\quad + x_2 \cos(2\pi \times 1 \times 1/3) \\
&\quad + x_4 \cos(2\pi \times 1 \times 2/3) \\
y_3 &= x_1 \cos(2\pi \times 1 \times 0/3) \\
&\quad + x_3 \cos(2\pi \times 1 \times 1/3) \\
&\quad + x_5 \cos(2\pi \times 1 \times 2/3) \\
y_4 &= x_0 \sin(2\pi \times 1 \times 0/3) \\
&\quad + x_2 \sin(2\pi \times 1 \times 1/3) \\
&\quad + x_3 \sin(2\pi \times 1 \times 2/3) \\
y_5 &= x_1 \sin(2\pi \times 1 \times 0/3) \\
&\quad + x_3 \sin(2\pi \times 1 \times 1/3) \\
&\quad + x_5 \sin(2\pi \times 1 \times 2/3)
\end{aligned} \tag{5.2}$$

Appendix 5.B The bifurcation of the P1 solution

In the six-coupled system, after the P1 solution [6] (in P1 solution, one oscillator oscillates and others do not) loses its stability via the PF bifurcation as the coupling factor is increased, it jumps to the coexisting quasi-periodic solution (propagating wave)[6]. We expected the same type of bifurcation to occur in the three-coupled system, but we actually observed a different type of bifurcation. Specifically, the P1 solution loses its stability via the subcritical PF bifurcation, and then, it jumps to a periodic solution in which two oscillators oscillate and one does not as the coupling factor is increased [7]. This is different from the case involving the six-coupled system. The actual bifurcation scenario is shown in Fig. 5.18. The P1 solution loses its stability via the subcritical PF bifurcation at $\alpha_{PF} = 0.091$ ($D1$ and $D1'$ indicate the unstable branch attached to $D0$.), and then, it subsequently becomes $\tilde{D}1$, $D3$, and $\hat{D}1$ after two iterations of Neimark-Sacker bifurcations on the basis of the increase in the coupling factor.

[6] We called the P1 solution as the Type 1 solution in [6].
[7] We called the P1 solution as the Type 2 solution in [20].

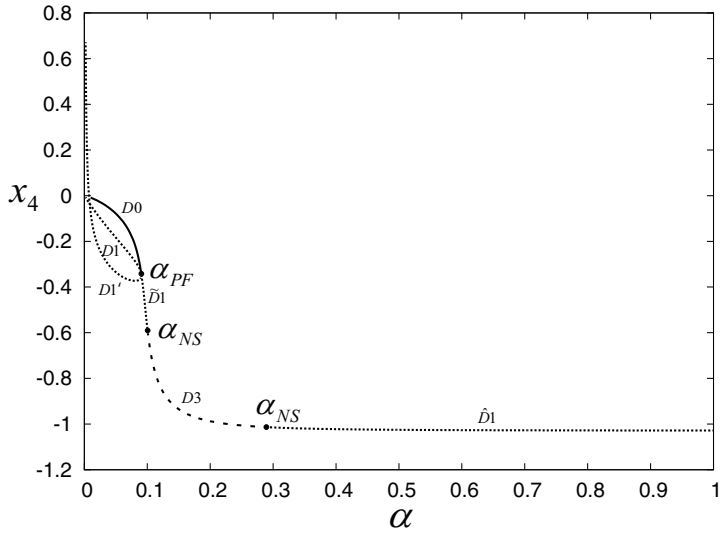

Figure 5.18: One-parameter-bifurcation diagram of the the P1 solution $D0$ for $\epsilon = 0.36$ and $\beta = 3.20$.

Appendix 5.C The heteroclinic (HC) tangle

Consider two saddle points "a" and "b" on the local cross section Σ. When UM of "a" intersects SM of "b," the cross points are called as HC points, and they are countably infinite. We call the intersection as the HC tangle. Because UM with the HC tangle is compressed and stretched in two directions, the mapped points on UM tend to be in different directions upon small changes in the initial condition and/or parameter values. This leads to a sensitive dependence of the flow on the initial condition. There are two boundary parameters of the HC tangle at which UM and SM exhibit HC tangency, as shown in Figs. 5.19(a) and (c). They are called as the critical parameter values of HC bifurcation. In our case, because UM is one-dimensional and SM is four-dimensional, the schematics of HC tangle are shown in Fig. 5.19(b) and those of HC tangency are shown in Figs. 5.19(a) and (c). We note that UM in Figs. 5.17(a) and (c) is eventually directed in one direction, but the one in Fig. 5.17(b) is compressed and stretched in two directions. This is an evidence that the HC tangle exists.

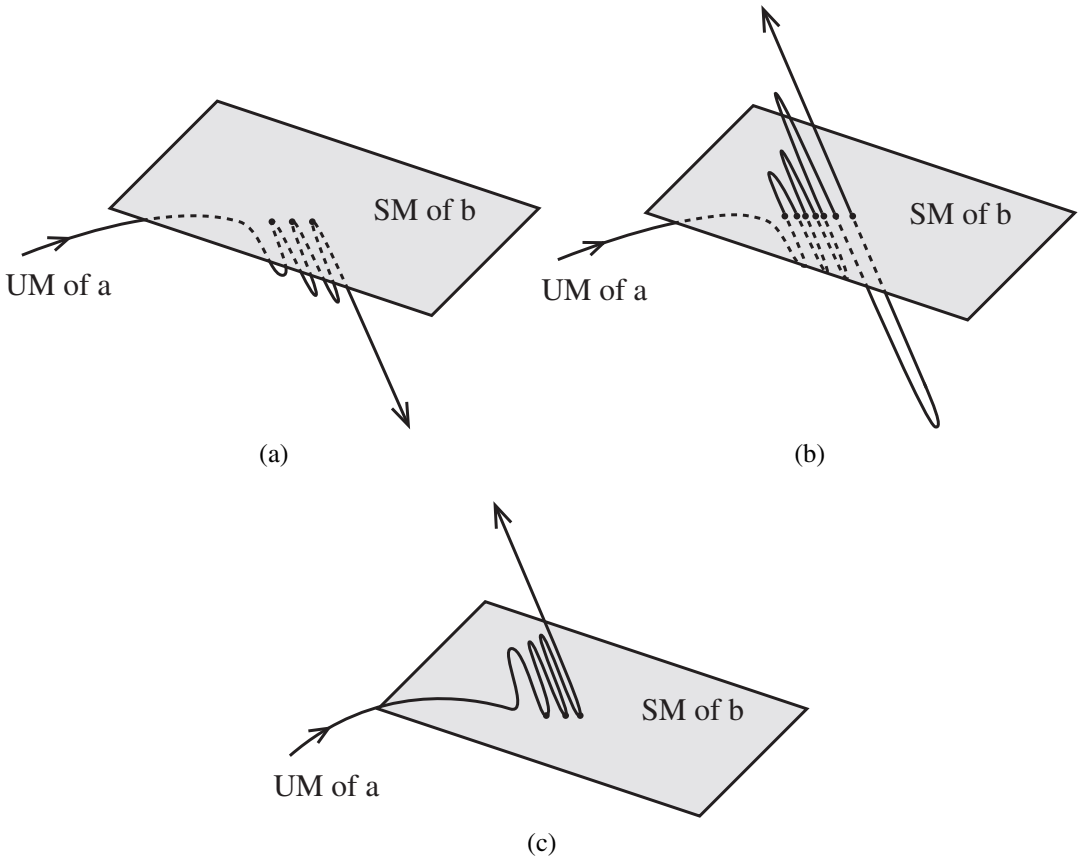

Figure 5.19: Phase space diagrams of UM and SM around the HC tangle. (a) The diagram at the bifurcation point of $\alpha = \alpha_{c1}$ showing the HC tangency. (b) The diagram for $\alpha_{c1} < \alpha < \alpha_{c2}$ showing the HC tangle. (c) The diagram at the bifurcation point of $\alpha = \alpha_{c2}$ showing the HC tangency.

6 Algorithm for Obtaining a Saddle Torus Between Two Attractors

We develop two algorithms for obtaining an index 1 saddle torus between two attractors of which basin boundary is smooth by using bisection method. In the first algorithm, which we name "overall template method," we make a template approximating a whole attractor and use it for pattern matching. The attractor can be a periodic orbit, a torus and even a chaos. In the second algorithm, which we name "partial template method," we make a template approximating only a part of an attractor. In this algorithm, the attractor is restricted to a periodic orbit and a two-torus, but calculation time is much smaller than that of the overall template method. We demonstrate these two algorithms for two solutions, observed in a ring of the six coupled bistable oscillators. One is a saddle torus in the basin boundary of the two switching solution, and the other is of the two quasi-periodic propagating wave solutions. We calculate the Lyapunov spectrum of the obtained saddle torus, and confirm one positive Lyapunov exponent.

6.1 Introduction

The numerical algorithm for obtaining a saddle fixed point on a Poincaré section using Newton's method has been well known for a long time. It has been used for calculating bifurcation sets of fixed points [1]. However, to the best of our knowledge, there is no algorithm for obtaining a saddle torus [1]. It is important to obtain a saddle torus when we calculate the bifurcation of a quasi-periodic solution because obtaining a saddle torus is indispensable in proving various torus bifurcations such as saddle-node and pitchfork [25]. For example, in saddle-node bifurcation, a stable torus (node) merges with an unstable torus (saddle) and both disappear. In a supercritical pitchfork bifurcation, a stable torus (node) becomes an unstable torus (saddle) surrounded by two stable tori (nodes).

We recently developed an algorithm for obtaining a saddle torus in the basin boundary of two attractors by using the bisection method. In general, there is a saddle periodic orbit or a saddle torus (or even a saddle chaos) in the basin boundary of two attractors. Therefore, to obtain a saddle torus, we first calculate the basin boundary. To do this, we must know which of the two attractors a given initial condition leads. Assuming that an initial point "a" leads to attractor A and an initial point "b" leads to attractor B, the basin boundary is on the line connecting points "a" and "b." Therefore, by using the bisection algorithm, the distance between "a" and "b" can be reduced to obtain the basin boundary of any desired

[1] The torus means N-torus as a flow for $N \geq 2$. When $N = 2$, it is called an invariant closed curve (ICC) on Poincaré section.

accuracy. We assume that the saddle torus is stable in the basin boundary. Therefore, if we can restrict the dynamics in the basin boundary, the trajectory converges to the saddle torus automatically. This gives an outline of our method. The limitation of this algorithm is that the unstable dimensionality of the saddle torus must be one (the unstable direction is to be included in the complementary subspace of the basin boundary). In Section 3, we describe a general template method applicable to all types of attractors. In Section 4, we describe a partial template method applicable to attractors in the form of a fixed point and an invariant closed curve (ICC) in a Poincaré section. Although the partial template method has some restrictions, it is much faster than the overall template method. We demonstrate these two algorithms for two cases: a saddle ICC in the basin boundary of two stable branches of the switching solution and a saddle ICC in the basin boundary of two quasi-periodic propagating wave solutions, both observed in a six-coupled bistable oscillator system [20]. We calculate the Lyapunov spectrum of the obtained saddle torus and confirm whether there is more than one positive Lyapunov exponent.

6.2 Bisection Algorithm for deriving a Saddle Torus

In general, there exists a basin boundary between the basins of two attractors A and B. Here each attractor can be a periodic orbit, a torus, or a chaos, in which case, there exists a saddle torus (or a saddle periodic orbit) in the basin boundary. We will obtain this saddle torus by using the bisection algorithm. Fig. 6.1 shows a conceptual diagram for tracing a saddle torus that exists in a basin boundary of two attractors. Take arbitrary points a_0 and b_0 in the basins of attractors A and B, respectively. Calculate a'_0 and b'_0 close to each other by using the bisection algorithm. Here a'_0 and b'_0 should belong to the basins of attractors A and B, respectively. Then

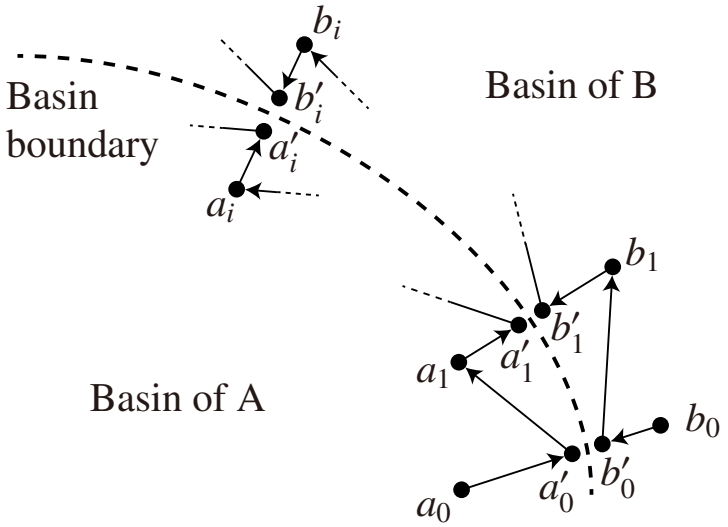

Figure 6.1: Conceptual diagram showing algorithm for tracing a saddle torus.

apply the mapping for a'_0 and b'_0 to obtain a_1 and b_1, respectively, and repeat this process. We

assume the following in our dynamical system. 1) The unstable dimensionality of the basin boundary between A and B must be one. 2) Two attractors should be asymptotically stable ordinary attractors[2]. 3) The basin boundary between two attractors is smooth[3]. 4) A part of attractors A and B must be adjacent. 5) There is no basin of other attractor besides A and B on the line connecting two initial points a_0 and b_0.

Fig. 6.2 presents a flowchart of the bisection algorithm. Take a_i and b_i, which belong to the

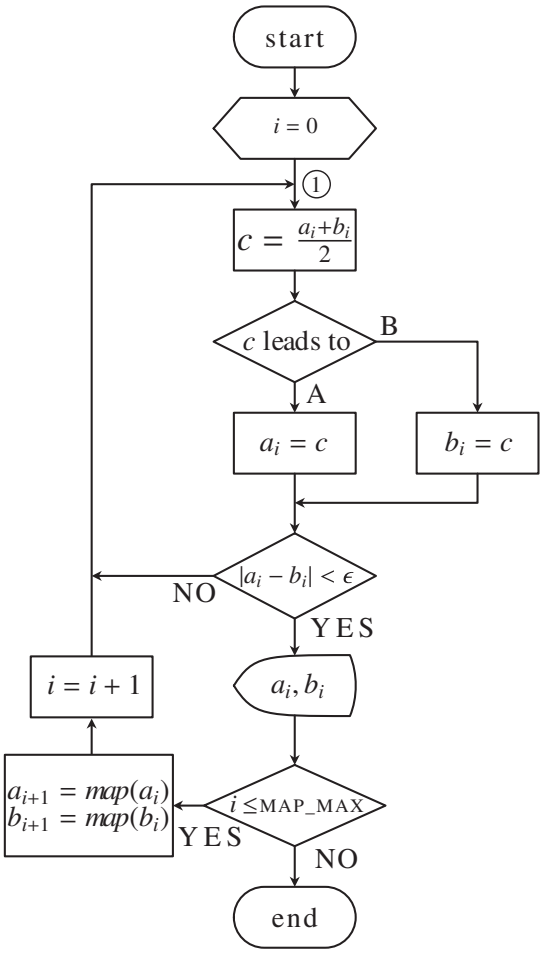

Figure 6.2: Flowchart for tracing a saddle torus via the bisection algorithm.

basins of A and B, respectively. Then, take the mid-point c of a_i and b_i. If the initial point c leads to attractor A, a_i is replaced by c, and if c leads to attractor B, b_i is replaced by c. Then, measure the distance between a_i and b_i. If the distance is greater than or equal to some small value ϵ, we go back to ①. If it is less than ϵ we accept and output a_i and b_i. Next, if i is smaller than or equal to a certain fixed value MAP_MAX, then map them to obtain a_{i+1} and b_{i+1}, respectively and increase i by one before going back to ①. If i becomes greater than

[2] So far, the so called "hidden attractors" [26] are excluded.

[3] There may be some cases in which the basin boundary is non-smooth such as fractal. Our algorithm cannot apply for such a case so far.

MAP_MAX, we stop this algorithm. The most important part of this flowchart is to judge to which attractor, A or B, an initial point c leads. If the attractor is a periodic solution, it becomes a periodic orbit on the Poincaré section. Therefore, an initial point converges to one point (or a set of points) essentially. Therefore, it is not difficult to recognize which periodic orbit the initial condition leads to. Namely, we can easily judge the point attractor by simply measuring the distance between an adequately mapped point and the periodic orbit. However, if the attractor is quasi-periodic or chaotic, it becomes a complex object on the Poincaré section, and therefore its detection becomes more difficult. This algorithm can be applied for obtaining a saddle periodic orbit, a saddle torus, or a saddle chaos as long as its index (hence its unstable dimensionality) is one.

6.3 Overall Template Method

We overcome the difficulty stated in the previous section as follows:
1. We take P points after transient is decayed that cover all parts of the attractor in the N-dimensional space and project them in the M-(≤ N)dimensional space for reducing calculation time. We must define the dimension M and its projection direction depending on cases. In general, we must choose the dimension and its projection in order not to crush or overlap attractors A and B [4].
2. We divide the region covering the attractor into many M-dimensional cubes by discretization as shown in Fig. 6.3. We mark all the cubes in which there is more than one point. In

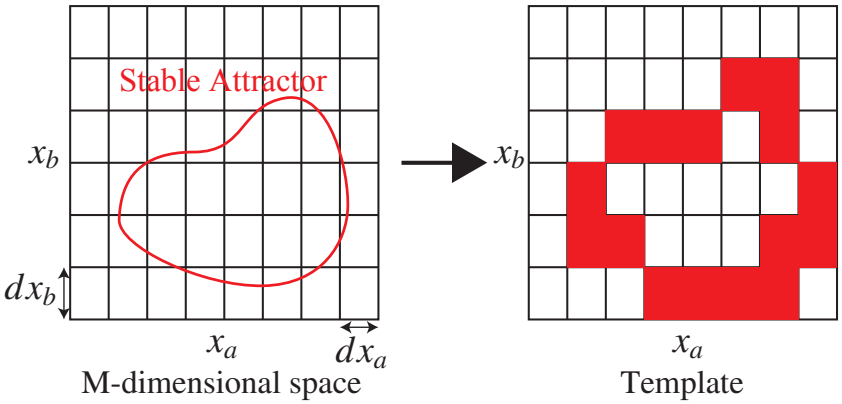

Figure 6.3: Schematic of the attractor discretization algorithm.

this way, we can make a template consisting of many cubes inherent to the attractor. Most of cubes must be taken in the basin of the attractor [5].
3. We make another template corresponding to the other attractor in the same manner.

[4] In the example of a ring of six coupled oscillators stated in Section 5, we choose P= 5000, M= 3 and use the projection onto the (x_0, x_2, x_4)-subspace.
[5] In fact, some amount of cubes can belong to both attractors. As the number of overlapped cubes and the decision percentage are closely related, we must carefully determine the decision percentage.

4. If the template corresponding to a certain initial point agrees with the template of the attractors A or B by more than certain percentage [6] (we call this the decision percentage), we recognize that the initial point leads to the attractor.
In principle, this algorithm can be applied for all types of attractors on Poincaré section, a periodic orbit, a torus, and a chaos.

6.4 Partial Template Method

This is a faster algorithm for obtaining a saddle torus between two stable "two"-tori. A drawback of the overall template method for obtaining a saddle torus described in Section 3 is that the algorithm takes a long time to discriminate to which of the two attractors, A or B, an initial condition leads. The primary reason is that a long transient time is spent in making a template (set of cubes) of an attractor. In the following section, we consider the case where the attractors A and B are two-tori. They then become ICCs on the Poincaré section. Fig. 6.4 represents a schematic of the mapped points of a stable two-torus. We take two successive points "p"

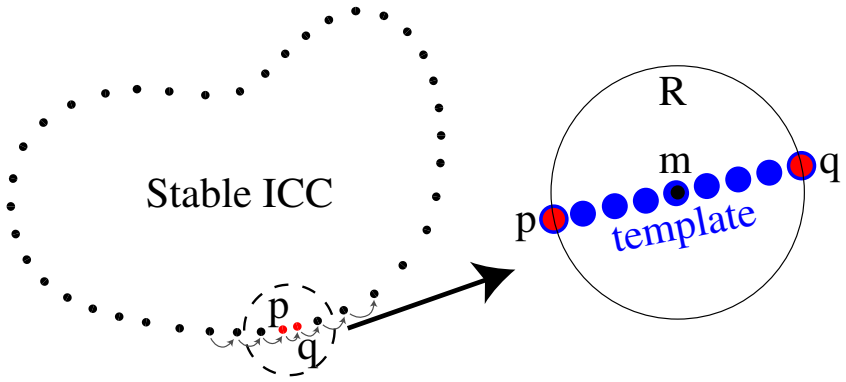

Figure 6.4: Schematic of faster stable ICC templatizing algorithm.

and "q" (q is a mapped point of p). Since the mapped points fall in the interval between "p" and "q" many times while repeating the Poincaré map, we regard a set of sufficient number of points between "p" and "q" (including end points "p" and "q") as a template of the associated ICC as shown in Fig. 6.4. The algorithm for making a set of mapped points into a template is as follows:
1. Take two successive points "p" and "q" in a stable ICC. The distance between these two points should be as small as possible.
2. Calculate a middle point $m = (p + q)/2$ and make a hyper-circle R centered at m, whose radius is $r = |p - q|/2$.
3. Store sufficient points in R while repeating the Poincaré map, and consider the end points "p" and "q" and the stored points in R as the associated template. To include "p" and "q" is

[6] In the example of a ring of six coupled oscillators stated in Section 5, if a template from a certain initial point agrees with that of A (or B) by more than 80% (the decision percentage), we recognize the initial condition leads to A (or B). So far, we determine the decision percentage by try-and-error method.

crucial when phase locking of ICC A or ICC B has occurred [7].
In this manner, we can make templates for ICC A and ICC B. We can recognize easily which attractor, ICC A or ICC B, an initial point leads to, by calculating the distance between the mapped point (in the interval of "p" and "q") and each point in the templates for A and B. With this algorithm, we can judge the convergence to an ICC as soon as one mapped point falls in one of the templates. Compared to the overall template method, this method saves a lot of time in calculating the long transient, which is unnecessary for most initial points [8]. This algorithm can be applied for obtaining a saddle torus when sandwiched between the two attractors A and B, where A and B can be a periodic orbit or a two-torus.

6.5 Examples of Our Algorithms

We give some examples in which we succeed in obtaining a saddle torus. These examples can be observed in a ring of six coupled oscillators described in the following equation: [20]

$$\begin{cases} \dot{x}_{i\times 2} &= x_{i\times 2+1}, \\ \dot{x}_{i\times 2+1} &= -\epsilon(1-\beta x_{i\times 2}^2 + x_{i\times 2}^4)x_{i\times 2+1} - (1-\alpha)x_{i\times 2} \\ & \quad + \alpha(x_{i\times 2-2} - 2x_{i\times 2} + x_{i\times 2+2}), \\ & \quad x_{-2} = x_{10}, x_{12} = x_0, \end{cases} \tag{6.1}$$
$$i = 0, 1, 2, 3, 4, 5.$$

Parameters α, β, and ϵ indicate coupling factor, amplitude control parameter, and degree of nonlinearity, respectively. A cross section of the Poincaré map is defined as $\Sigma : \{(x_0, x_1, \cdots, x_{11}) \in R^{11} | x_1 = 0, \dot{x}_1 < 0\}$. In this chapter, β is fixed as 3.20 and ϵ is fixed as 0.36 for Figs. 5–8, and 0.32 for Figs. 9–11.

In Fig. 6.5, we first demonstrate the switching solution for $\alpha = 0.11$ with initial conditions $x_0 = 2.0, x_1 = -2.0$, and all other variables are zero. In the switching solution, a pair of (x_0, x_2) and (x_6, x_8), which are synchronized with the reverse phase, alternate between oscillation (alive) and no oscillation (dead). The switching solution is a two-torus quasi-periodic solution. Fig. 6.6 presents a bifurcation diagram of the switching solution in terms of α [27]. In this diagram, a stable two-torus showing the stable switching solution (SSW) exists for $\alpha > \alpha_{crt} \simeq 0.1082$. When α decreases across α_{crt}, a supercritical pitchfork bifurcation occurs and the stable two-torus (SSW) becomes an unstable two-torus (USW), and a pair of stable two-tori (SSW1 and SSW2) emerge around the USW. The distance D is an averaged distance of SSW1 and SSW2 from the hyperplane H to which the USW is restricted. This is clearly supercritical pitchfork bifurcation. In this example, the USW can be easily calculated using the restricted dynamics of Eq. (6.1) to H [9]. In this chapter, we calculate the USW in the basin boundary of two stable tori, SSW1 and SSW2, directly from Eq. (6.1). We use the USW obtained from a restricted system as a standard, because it can be calculated as an "attractor"

[7] When phase locking occurs, only "p" and "q" may appear in the interval.

[8] In general, the time for convergence to attractor A or B depends on a given initial point. In the overall template method, however, the calculation time for all initial points must be equal. It must be set to meet the slowest convergent initial point. This causes a lot of unnecessary calculation time.

[9] In other words, the unstable dimension of the USW is included in the complementary subspace $H^{\perp}$. The details of this analysis can be referred to [28].

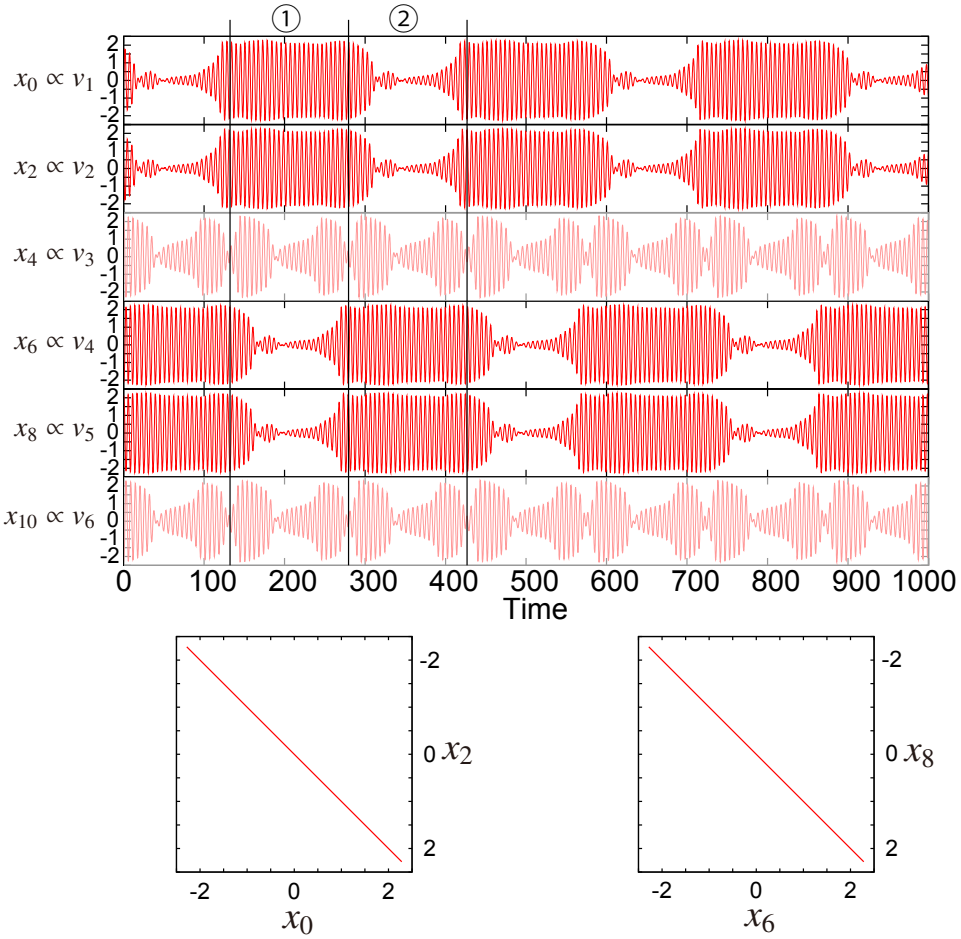

Figure 6.5: Time waveforms of the switching solution for $\alpha = 0.11, \beta = 3.20$ and $\epsilon = 0.36$, with initial conditions $x_0 = 2, x_2 = -2$, and others are all zero. Interval ①: (x_0, x_2) is alive and (x_6, x_8) is dead. Interval ②: The inverse of interval ①. Reproduced from Fig. 16 of [20].

in the restricted subspace, and therefore more reliable compared to the other two methods proposed here.

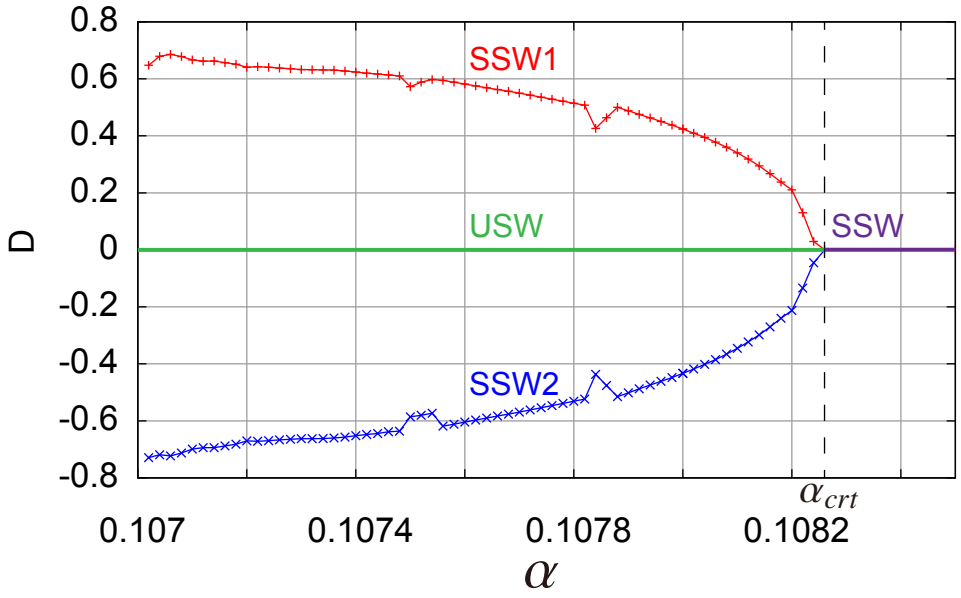

Figure 6.6: Bifurcation diagram of the switching quasi-periodic solution in terms of α for $\beta = 3.20$ and $\epsilon = 0.36$ [27]. This shows supercritical pitchfork bifurcation: $\alpha_{crt} = 0.10826$. D is the distance between SSW1 (SSW2) and the hyperplane. Reproduced from Fig. 4 of [27].

Fig. 6.7 presents the USW for $\alpha = 0.108$. In Fig. 6.7, we calculate a saddle ICC by three

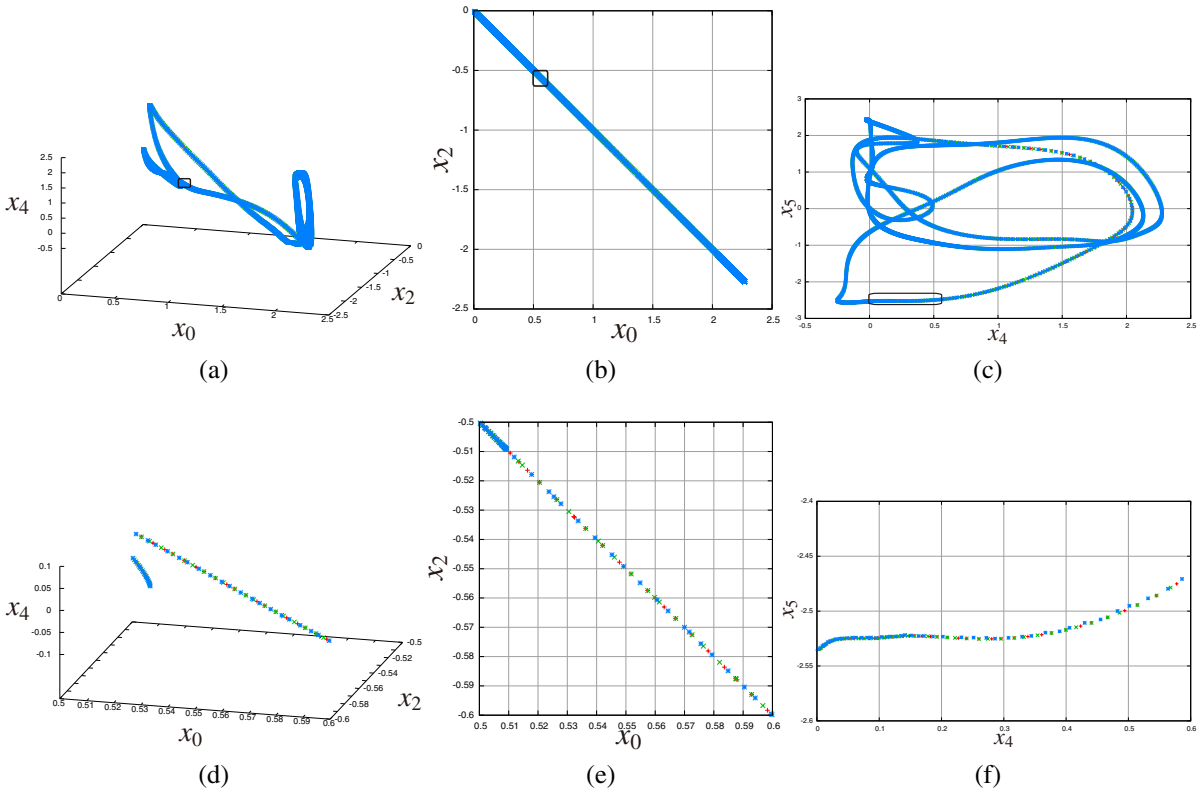

Figure 6.7: Unstable ICC (USW) for $\alpha = 0.108, \beta = 3.20$ and $\epsilon = 0.36$ in the Poincaré section Σ. The USW calculated from the restricted system is presented by red points, that from the overall template method by green points, and that from the partial template method by blue points, which agree very well. The data points obtained by three methods agree so well and overlap that only latest plots (blue) appear in (a), (b), and (c). (a) Projection onto the (x_0, x_2, x_4)-space. (b) Projection onto the (x_0, x_2)-space. (c) Projection onto the (x_4, x_5)-space. (d) Enlarged diagram surrounded by the square in (a). (e) Enlarged diagram surrounded by the square in (b). (f) Enlarged diagram surrounded by the square in (c).

methods: the first using the restricted system (red points), the second using the algorithm in Section 3 (green points), and the third using the algorithm in Section 4 (blue points), all of which are in good agreement [10].

We compare the calculation time using the method in Sections 3 and 4 by using the example given in Fig. 6.7. In this example, the time for obtaining 1000 points unstable ICC

[10] We evaluate the difference of these three methods by using the average of absolute errors of 500 mapped points. The error between the restricted method result and the overall template method result is 2.7656×10^{-5}, and the error between the restricted method result and the partial template method result is 9.5273×10^{-5}. The precision accuracy of the bisection algorithm of this part is taken as 1.0×10^{-10} as a special case, and absolute tolerance of the 5th-order Runge-Kutta method used here is 1.0×10^{-8}.

(USW) is 1071.710 s for the overall template method in Section 3 and 21.084 s for the partial template method in Section 4 [11]. The enormous time difference mainly occurs because, in the former method, we calculated the unnecessary long transient even for the case of short transient time (because we could not confirm the convergence to the stable ICC), whereas in the latter method, we can confirm the convergence in the process of calculation, and therefore choose the appropriate transient time. Lyapunov exponents for the USW for $\alpha = 0.108$ are as follows: $LE1 = 8.14 \times 10^{-04} > 0, LE2 = -4.36 \times 10^{-05} \simeq 0, LE3 = -1.57 \times 10^{-05} \simeq 0, LE4 = -2.03 \times 10^{-02} < 0, LE5, \cdots, LE12 < 0$. This verifies that the USW is index 1 ICC. Furthermore, Lyapunov exponents for the USW for $\alpha = 0.1073$ are as follows: $LE1 = 2.94 \times 10^{-03} > 0, LE2 = -8.98 \times 10^{-05} \simeq 0, LE3 = -2.27 \times 10^{-05} \simeq 0, LE4 = -2.20 \times 10^{-02} < 0, LE5, \cdots, LE12 < 0$. One may misunderstand that this is a chaotic attractor because of one positive Lyapunov exponent. However, one positive Lyapunov exponent here comes from one-dimensional "instability" of ICC. As far as we know, there are few examples of Lyapunov exponents' calculation for unstable solution due to difficulty of tracing the unstable core orbit. In fact, we must modify the core orbit of the variational equation, obtained by the partial template method, for every small time interval $T(= 0.1$ sec in this case) via the bisection method for calculating Lyapunov exponents [12].

Fig. 6.8 presents SSW1, SSW2, and the USW for $\alpha = 0.1068$, where SSW1 and SSW2 are chaotic attractors [13] and the USW is a saddle two-torus (see Fig. 5 of [27]). Our algorithm in

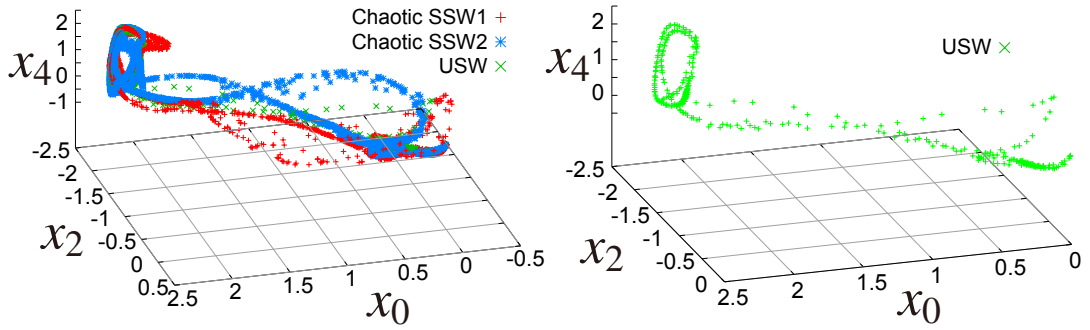

(a) (b)

Figure 6.8: Saddle ICC between two chaotic attractors. (a) SSW1 (red) and SSW2 (blue) are chaotic attractors and the USW (green) is a saddle ICC. (b) The extracted USW (saddle ICC). Parameters are $\alpha = 0.1068, \beta = 3.20$, and $\epsilon = 0.36$.

Section 3 works for a saddle torus sandwiched by two chaotic attractors! Correctness of the obtained saddle ICC is confirmed by calculating the saddle ICC via the restricted system [27],

[11] The computational environment is as follows: CPU: Intel Core i7-2600K, 3.8 GHz; Compiler: Visual Studio 2012 (cl /O2 /EHsc); Computational method and its accuracy: 5th-order Runge-Kutta method with absolute tolerance= 1.0×10^{-8}; Accuracy of bisection algorithm (excluding the data in Fig. 6.7) = 1.0×10^{-5}.

[12] As to interpretation of Lyapunov exponents, we obey the following reference [29], although there exist more in-depth understandings [30].

[13] Lyapunov exponents for SSW1 (SSW2) are $LE1 = 3.18 \times 10^{-3} > 0, LE2 = -4.69 \times 10^{-5} \simeq 0, LE3 = -8.32 \times 10^{-4} < 0, LE4, \cdots, LE12 < 0$.

confirming that the same saddle ICC can be obtained from a restricted system. Lyapunov exponents for the USW for $\alpha = 0.1068$ are as follows: $LE1 = 4.29 \times 10^{-03} > 0, LE2 = -1.76 \times 10^{-05} \simeq 0, LE3 = -2.64 \times 10^{-05} \simeq 0, LE4 = -2.31 \times 10^{-02}, LE5, \cdots, LE12 < 0$. This verifies that the USW is index 1 ICC. From the results for $\alpha = 0.1080, 0.1073$, and 0.1068, we notice that the positive Lyapunov exponent $LE1$ of the USW increases as α moves from the bifurcation point $\alpha_{crt} = 0.10826$.

Next, we will demonstrate another example from PW1L (R) and PW2L (R)[14]. Fig. 6.9 demonstrates a saddle ICC between two propagating wave solutions PW1L (R) and PW2L (R) from a ring of six coupled bistable oscillator system by using the faster algorithm in Section 4. In this example, we cannot create a restricted system. Fig. 6.9(a) indicates a saddle ICC (green) between the propagating wave solutions PW1L (blue) and PW2L (red) rotating counterclockwise for $\alpha = 0.1930$, both stable ICCs. Similarly, in Fig. 6.9(b) we obtain a

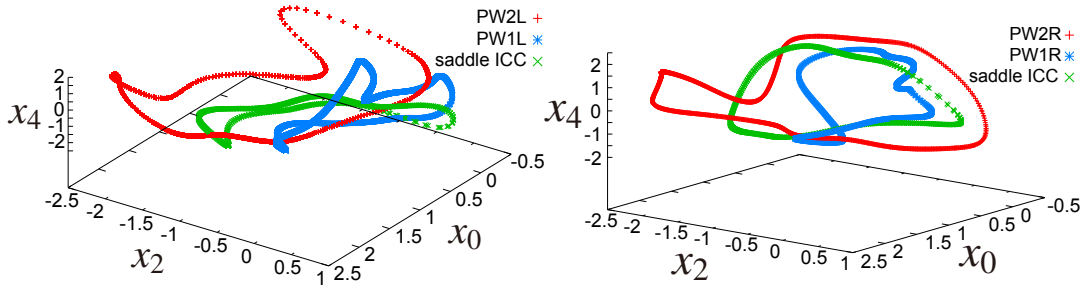

(a) (b)

Figure 6.9: Saddle ICC in the basin boundary of PW1 and PW2. (a) Counterclockwise rotation (PW1L and PW2L). (b) Clockwise rotation (PW1R and PW2R). Parameters are $\alpha = 0.1930, \beta = 3.20$ and $\epsilon = 0.32$.

saddle ICC (green) betweenPW1R (blue) and PW2R (red) rotating clockwise for the same parameters.

Fig. 6.10 presents saddle ICCs for three values of $\alpha = 0.1930, 0.1941$, and 0.1942 rotating counterclockwise. For $\alpha = 0.1930$ and 0.1941, saddle ICCs (green and blue closed curve, respectively) can be obtained with this algorithm; however, for $\alpha = 0.1942$, we cannot obtain a saddle ICC. This means that saddle ICCs for $\alpha = 0.1930$ and 0.1941 are index 1, while that for $\alpha = 0.1942$ is greater than index 2. In Fig. 6.11, we calculate Lyapunov exponents of the saddle ICCs in terms of $\alpha = 0.1930, \cdots, 0.1950$. This verifies that there exists an index 1 saddle torus for $\alpha = 0.1930, \cdots, 0.1941$ because only $LE1$ is positive, and for $\alpha > 0.1941$, there is no index 1 saddle torus for most of α because $LE1$ and $LE2$ are positive, in which case our algorithm does not work. However, because of phase locking, many small index 1 saddle torus (only $LE1$ is positive) regions appear. From this result, we suppose that some kind of bifurcation of the index 1 saddle ICC occurs around $\alpha = 0.1941$.

[14] PW1L(R) is an abbreviation of Propagating wave solution of Type 1 propagating counterclockwise (clockwise) [6]. PW2L(R) is abbreviation of Propagating wave solution of Type 2 propagating counterclockwise (clockwise) [20]. They are asymptotically stable in a ring of six-coupled oscillators.

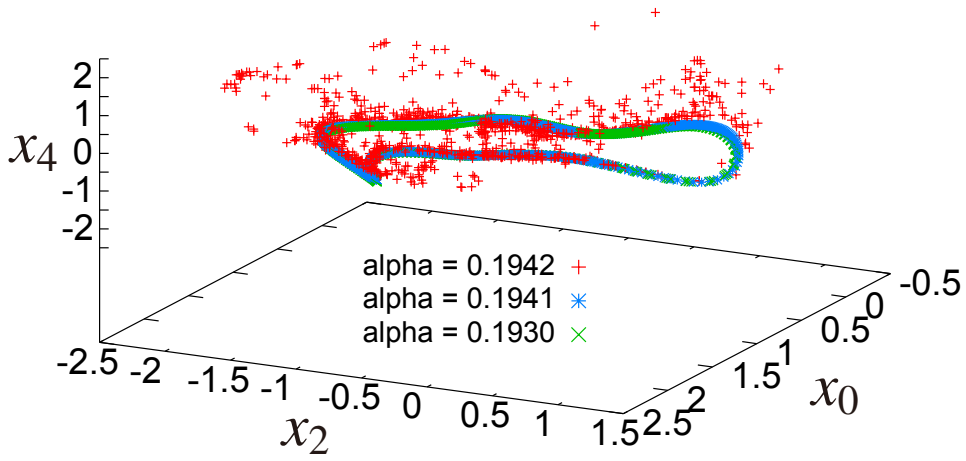

Figure 6.10: Converged saddle ICC for $\alpha = 0.1930$ (green) and 0.1941 (blue), and unconverged case for 0.1942 (red). Parameters are $\beta = 3.20$ and $\epsilon = 0.32$.

6.6 Conclusions

We propose two algorithms for judging the convergence of two attractors, and succeed in obtaining an index 1 saddle torus in the basin boundary of two attractors via the bisection algorithm. In the first algorithm which we named the "overall template method," all parts of the attractor are divided into many cubes and a set of these cubes constitutes the associated template. Since this method uses all parts of the attractor as a template, it takes a long time to derive a saddle torus. However, this method applies to all kinds of attractors, a periodic orbit, a torus, and a chaos. In the second algorithm, which we named the "partial template method," only a part of the attractor is used as a template, and therefore, the derivation of the saddle torus is much faster than that with the first algorithm. However, in the partial template method, the attractor is restricted to a two-torus (including a periodic orbit), namely, ICC on a Poincaré section. We demonstrate two examples; one is the saddle torus obtained from supercritical pitchfork bifurcation of the switching solution; the other is the saddle torus between two kinds of propagating wave solutions. They are both observed from a ring of six-coupled oscillators. We calculate Lyapunov exponents for the obtained saddle ICCs, which verify our algorithm. Calculating Lyapunov exponents of a saddle ICC using correction of core orbit via the bisection method seems novel. After all, we have developed two algorithms for obtaining an index 1 saddle torus; namely, the overall template method and the partial template method. Our future research objective is to extend our algorithm to the cases where there is an index 2 saddle torus, a non-smooth basin boundary, and a hidden attractor. From engineering point of view, the propagating waves shown in Fig. 9 have a potential application as an active transmission line. They propagate with no decay, therefore, if one makes a large array of coupled bistable oscillators, it may be used as a transmission line in neuro-dynamics and communication systems, etc.. Therefore, to investigate bifurcations of these solutions using unstable ICC become important subject of research.

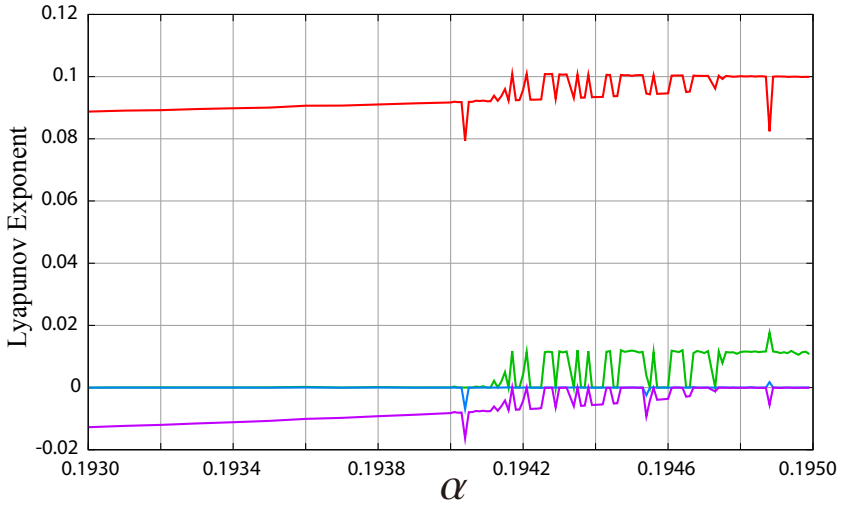

Figure 6.11: Four major Lyapunov exponents $LE1$ (red), $LE2$ (green), $LE3 \simeq 0$ (blue), and $LE4$ (purple) of the saddle ICC in the basin boundary of PW1L and PW2L in terms of α. Step size of α is chosen as 0.0001 from 0.1930 to 0.1940, and 0.00001 from 0.1940 to 0.1950. Fixed parameters are $\beta = 3.20$ and $\epsilon = 0.32$.

7 General Conclusion

In this paper, we have analyzed the bifurcation of quasi-periodic solutions observed in several-types of coupled bistable oscillator systems. In Chapter 2, we have focused on the propagating wave characteristics of the quasi-periodic solutions which exist in these systems. Namely, we have investigated the propagating velocity and statistical characteristic of them. In Chapter 3, we have clarified the bifurcation mechanisms of two quasi-periodic solutions, the propagating wave and the switching solutions. As a result, we have elucidated that the bifurcation mechanisms of the quasi-periodic solutions, related to appearance and disappearance of the propagating wave solution, are due to heteroclinic bifurcation. In Chapter 4, we have developed the algorithm for obtainig saddle quasi-periodic solutions. We have elucidated the existence of saddle quasi-periodic solutions of quasi-periodic saddle-node and pitchfork bifurcations by using this algorithm. In Chpter 5, we have clarified that appearance and disappearance of the quasi-periodic solution with three-phase synchronized envelopes (ICC3ϕ) are not due to phase-locking phenomena of Arnold tangues. Namely, it is due to heteroclinic bifurcations of three coexisting three-periodic solutions. In Chapter 6, we have improved the algorithm for obtaining saddle quasi-periodic solution explained in Ch. 4. We expand the scope of this algorithm, namely the kind of attractors to which this algorithm can be applied. This algorithm can be applied not only to a saddle quasi-periodic solution in the basin boundary between a periodic solution and a quasi-periodic or chaotic attractors, but to one in the basin boundary between any attractors. Moreover, we have developed high speed version of this algorithm which can be applied to a saddle quasi-periodic solution sandwiched with periodic or 2-torus attractors. Thus, we have made the foothold of bifurcation analysis of quasi-periodic solutions not analyzable before. In future works, more detailed elucidation of both local and global bifurcations of a quasi-periodic solution is desired.

Acknowledgements

The author would like to thank Professor Tetsuro Endo of Meiji University for providing me this precious study opportunity in his laboratory, helpful support, and considerable encouragement. The author is very grateful to Professor Motomasa Komuro of Teikyo University of Science for his valuable discussion and his elaborated advice from the mathematical point of view. The author appreciate Professor Hiroyuki Kamata of Meiji University and the members of his laboratory from their support and comfortable space for study. The author would like to thank Professor Naoki Matsumoto for his invaluable proof reading and helpful suggestions of this manuscript. Finally the author would like to extend my indebtedness to my parents, Atsumi and Jun, and my cat, Sasuke, for their endless love, support, and sacrifice throughout my study.

December 16, 2013 Kyohei Kamiyama

Bibliography

[1] H. Kawakami, "Bifurcation of periodic responses in forced dynamic nonlinear circuits: Computation of bifurcation values of the system parameters," IEEE Trans. Circuit Syst., vol.CAS-31, no.3, pp.248–260, March 1984.

[2] J.P. Keener, "Propagation and its failure in coupled systems of discrete excitable cells," SIAM Journal on Applied Mathematics, vol.47, no.3, pp.556–572, June 1987.

[3] Y. Nishiura, D. Ueyama, and T. Yanagita, "Chaotic pulses for discrete reaction diffusion systems," SIAM Journal on Applied Dynamical Systems, vol.4, no.3, pp.733–754, Aug. 2006.

[4] Y. Masayuki, W. Masahiro, N. Yoshifumi, and U. Akio, "Wave propagation phenomena of phase states in oscillators coupled by inductors as a ladder," IEICE Trans. Fundamentals, vol.E82-A, no.11, pp.2592–2598, Nov. 1999.

[5] K. Shimizu, T. Endo, and D. Ueyama, "Pulse wave propagation in a large number of coupled bistable oscillators," IEICE Trans. Fundamentals, vol.E91-A, no.9, pp.2540–2545, Sept. 2008.

[6] K. Shimizu, M. Komuro, and T. Endo, "Onset of the propagating pulse wave in a ring of coupled bistable oscillators," NOLTA, IEICE, vol.2, no.1, pp.139–151, Jan. 2011.

[7] K. Kamiyama, M. Komuro, and T. Endo, "Bifurcation analysis of the propagating wave and the switching solutions in a ring of six-coupled bistable oscillators –bifurcation starting from type 2 standing wave solution–," Int. J. Bifurcation and Chaos, vol.22, no.05, p.1250123 (13 pages), May 2012.

[8] M. Yamauchi, Y. Nishino, A. Ushida, and M. Tanaka, "Phase-inversion waves in oscillators coupled by two kinds of inductors as a ladder," IEICE Trans. Fundamentals, vol.E87-A, no.9, pp.2233–2240, Sept. 2004.

[9] O. Papy and H. Kawakami, "Bifurcations of the quasi-periodic solutions of a coupled forced van der pol oscillator," IEICE Trans. Fundamentals, vol.E77-A, no.11, pp.1788–1793, Nov. 1994.

[10] T.S. Parker and L.O. Chua, Practical Numerical Algorithms for Chaotic Systems, 3rd edition, Springer-Verlag, Jan. 1992.

[11] J. Guckenheimer and P. Holmes, Nonlinear Oscillations, Dynamical Systems, and Bifurcations of Vector Fields (Applied Mathematical Sciences Vol. 42), F. John, J.E. Marsden, and L. Sirovich, eds., second, rev, corr edition, Springer-Verlag, Aug. 1983.

[12] T. Endo and S. Mori, "Mode analysis of a multimode ladder oscillator," IEEE Trans. Circuit Syst., vol.23, no.2, pp.100–113, 1976.

[13] T. Endo and S. Mori, "Mode analysis of a ring of a large number of mutually coupled van der pol oscillators," IEEE Trans. Circuit Syst., vol.25, no.1, pp.7–18, Jan. 1978.

[14] J. Schaffner, "Simultaneous oscillations in oscillators," IRE Trans., vol.1, no.2, pp.2–8, June 1954.

[15] S.P. Datardina and D.A. Linkens, "Multimode oscillations in mutually coupled var der pol type oscillators with fifth-power nonlinear characteristics," IEEE Trans. Circuit Syst., vol.CAS-25, no.5, pp.308–315, May 1978.

[16] T. Endo and T. Ohta, "Multimode oscillations in a coupled oscillator system with fifth-power nonlinear characteristics," IEEE Trans. Circuit Syst., vol.27, no.4, pp.277–283, April 1980.

[17] C. Robinson, "Second-order averaging of forced and coupled nonlinear oscillators," IEEE Trans. Circuit Syst., vol.30, no.8, pp.591–598, Aug. 1983.

[18] K. Kamiyama, M. Komuro, and T. Endo, "Bifurcation of quasi-periodic oscillations in mutually-coupled hard type oscillators —demonstration of unstable quasi-periodic orbits—," Proceedings of the 2011 IEEE Workshop on Nonlinear Circuit Networks (NCN2011), pp.71–74, Dec. 2011.

[19] H.E. Nusse and J.A. Yorke, "A procedure for finding numerical trajectories on chaotic saddles," Physica D: Nonlinear Phenomena, vol.36, no.1-2, pp.137–156, June 1989.

[20] K. Kamiyama, M. Komuro, and T. Endo, "Bifurcation analysis of the propagating wave and the switching solutions in a ring of six-coupled bistable oscillators -bifurcation starting from type 2 standing wave solution-," Int. J. Bifurcation and Chaos, vol.22, no.5, p.1250123 (13 pages), May 2012.

[21] T. Yoshinaga and H. Kawakami, "Synchronized quasi-periodic oscillations in a ring of coupled oscillators with hard characteristics," IEICE Trans. A, vol.J75-A, no.12, pp.1811–1818, Dec. 1992.

[22] Y. Aruga and T. Endo, "Transitional dynamics and chaos in coupled oscillator systems," IEICE Trans. A, vol.86, no.5, pp.559–568, May 2003.

[23] E. Allgower and K. Georg, "Simplicial and continuation methods for approximating fixed points and solutions to systems of equations," SIAM Review, vol.22, no.1, pp.28–85, 1980.

[24] K. Kamiyama, M. Komuro, and T. Endo, "Origin of the quasi-periodic solutions with three-phase synchronized envelope in a ring of three-coupled bistable oscillators," IEICE, Proceedings of NOLTA 2011, pp.411–414, Sept. 2011.

[25] K. Kamiyama, M. Komuro, and T. Endo, "Bifurcation of quasi-periodic oscillations in mutually coupled hard-type oscillators —demonstration of unstable quasi-periodic orbits—," Int. J. Bifurcation and Chaos, vol.22, no.06, p.1230022 (13 pages), June 2012.

[26] G.A. Leonov and N.V. Kuznetsov, "Hidden attractors in dynamical systems. from hidden oscillations in hilbert kolmogorov, aizerman, and kalman problems to hidden chaotic attractor in chua circuits," Int. J. Bifurcation and Chaos, vol.23, no.01, p.1330002, 2013.

[27] K. Kamiyama, M. Komuro, and T. Endo, "Supercritical pitchfork bifurcation of the quasi-periodic switching solution in a ring of six-coupled, bistable oscillators," Int. J. Bifurcation and Chaos, vol.22, no.12, p.1250310 (8 pages), Dec. 2012.

[28] K. Kamiyama, M. Komuro, and T. Endo, "Bifurcation analysis of the quasi-periodic solution with three-phase synchronized envelopes in a ring of three-coupled, bistable oscillators," Int. J. Bifurcation and Chaos, vol.22, no.12, p.1250309 (13 pages), Dec. 2012.

[29] I. Shimada and T. Nagashima, "A numerical approach to ergodic problem of dissipative dynamical systems," Progress of theoretical physics, vol.61, no.6, pp.1605–1616, jun 1979.

[30] G.A. Leonov and N.V. Kuznetsov, "Time-varying linearization and the perron effects," Int. J. Bifurcation and Chaos, vol.17, no.4, pp.1079–1107, 2007.